DETERMINATION AND IMPLICATIONS OF ELECTROOSMOTIC TRANSPORT IN THE BRAIN

by

Yifat Guy

BS, University of Pittsburgh, 2004

Submitted to the Graduate Faculty of

Arts and Sciences in partial fulfillment

of the requirements for the degree of

Doctor of Philosophy

University of Pittsburgh

2011

UNIVERSITY OF PITTSBURGH

Graduate Arts and Sciences

This dissertation was presented

by

Yifat Guy

It was defended on

December 15, 2010

and approved by

Dr. Shigeru Amemiya, Professor, Department of Chemistry

Dr. Adrian Michael, Professor, Department of Chemistry

Dr. Mats Sandberg, Professor, Department of Anatomy and Cell Biology, Gothenberg University

Dissertation Advisor: Dr. Stephen G. Weber, Professor, Department of Chemistry

Reproduced with permission from:

Guy Y, Sandberg M, Weber SG. *Biophysical Journal.* 2008;94(11):4561-4569.

Guy Y, Muha RJ, Sandberg M, Weber SG. *Analytical Chemistry.* 2009;81(8):3001-3007.

DETERMINATION AND IMPLICATIONS OF ELECTROOSMOTIC TRANSPORT IN THE BRAIN

Yifat Guy, PhD

University of Pittsburgh, 2011

Electroosmotic flow is a bulk fluid flow that influences solute transport through capillary conduits and porous material under the influence of an electric field. The magnitude of electroosmotic flow is proportional to the ζ-potential of the capillary or porous material. A porous material such as living tissue would need to have an appreciable ζ-potential to create electroosmotic flow in the interstitial space. Transporting solutes in and out of tissue by virtue of electroosmotic flow in principle has advantages such as avoiding pressure effects and sample dilution that accompany micropush-pull and microdialysis approaches. In order to assess the viability of this approach, it is necessary to know the ζ-potential in the tissue of interest. To address this, a method and apparatus was developed to measure the ζ-potential and tortuosity in tissue slices. The method was applied to organotypic hippocampal slice cultures. The apparatus was improved on in order to provide feedback control to maintain a constant electric field through the tissue culture. The ζ-potential of the organotypic tissue culture is -22 ± 0.8 mV and the tortuosity is 2.24 ± 0.10. With a ζ-potential of -22 mV, low electric fields applied to the brain will create electroosmotic flow.

Electroosmotic flow can be directed to transport extracellular fluid from brain tissue into a conduit such as a sampling capillary. Furthermore, electroosmotic flow can be used in the opposite way to eject fluid and solutes from a capillary or pipette into brain tissue. The electroosmotic effect may be important in the widely used solute delivery method of iontophoresis. In iontophoresis, solutes are ejected into tissue via an applied current. Once in the tissue, solute transport is affected by the electroosmotic flow in the tissue and thus depends on the tissue ζ-potential. The dependence of solute transport on ζ-potential is illustrated using a set of poly(acrylamide-*co*-acrylic acid) hydrogels. A method of measuring the thickness of organotypic tissue cultures has also been developed. Characterization of ζ-potential and tortuosity provides the fundamentals for understanding electroosmotic flow through the extracellular space of brain tissue.

TABLE OF CONTENTS

PREFACE XIV

1.0 INTRODUCTION 1

- 1.1 ELECTROKINETIC TRANSPORT 2
- 1.2 PHYSICOCHEMICAL BRAIN PROPERTIES 4
- 1.3 THE MODEL SYSTEM: ORGANOTYPIC HIPPOCAMPAL SLICE CULTURE 5
- 1.4 QUANTITATIVE ANALYSIS OF THE EXTRACELLULAR SPACE 7

2.0 INITIAL MOTIVATION 9

3.0 DETERMINATION OF ZETA POTENTIAL IN RAT ORGANOTYPIC HIPPOCAMPAL CULTURES 15

- 3.1 INTRODUCTION 16
  - 3.1.1 Theory 19
- 3.2 MATERIALS AND METHODS 21
  - 3.2.1 Chemicals and solutions 21
  - 3.2.2 Instrumentation 22
    - 3.2.2.1 Capillary electrophoresis: 22
    - 3.2.2.2 Apparatus for tissue experiments 23
    - 3.2.2.3 Ag/AgCl electrodes 23

3.2.2.4 Injection capillary 24
3.2.2.5 Imaging 24
3.2.3 Procedures 25
3.2.3.1 Hippocampal organotypic slice cultures 25
3.2.3.2 ζ-potential determination 26
3.2.3.3 Two-fluorophore experiments 26
3.3 RESULTS 26
3.4 DISCUSSION 31
3.4.1 Analysis of the method 31
3.4.2 Analysis of the results 33
3.4.3 Potential applications and implications 36
3.5 ACKNOWLEDGMENTS 38
3.6 SUPPORTING MATERIAL 38
3.6.1 Results 38
3.6.2 Discussion 39
3.6.2.1 Analysis of the method 39
3.6.3 Materials and methods 39
3.6.3.1 Chemicals and solutions 39
3.6.3.2 Capillary electrophoresis 39
4.0 DETERMINATION OF ζ-POTENTIAL AND TORTUOSITY IN RAT ORGANOTYPIC HIPPOCAMPAL CULTURES FROM ELECTROOSMOTIC VELOCITY MEASUREMENTS UNDER FEEDBACK CONTROL 41
4.1 INTRODUCTION 42

4.2 THEORY 44

4.3 EXPERIMENTAL SECTION 46

4.3.1 Chemicals and solutions 46

4.3.2 Organotypic hippocampal slice cultures 47

4.3.3 Four-electrode potentiostat 47

4.3.4 Apparatus for tissue experiments 49

4.3.5 Injection capillary 50

4.3.6 Imaging 51

4.3.7 ζ-potential determination 51

4.4 RESULTS 53

4.5 DISCUSSION 57

4.5.1 Comparison of methods 57

4.5.2 Accuracy of the method 60

4.6 SUPPORTING INFORMATION 63

5.0 IONTOPHORESIS INTO A POROUS MEDIUM DEPENDS ON THE ZETA POTENTIAL OF THE MEDIUM 65

5.1 INTRODUCTION 66

5.1.1 Theory 68

5.2 EXPERIMENTAL 71

5.2.1 Chemicals and Solutions 71

5.2.2 Fluorophores 72

5.2.3 Determination of Diffusion Coefficients 72

5.2.4 Electrophoretic Mobility Determination by Capillary Zone Electrophoresis (CZE) 73

5.2.5 Synthesis of Hydrogels 74

5.2.6 ζ-Potential and Tortuosity 75

5.2.7 Porosity of Hydrogels 76

5.2.8 Conductivity of Hydrogels 77

5.2.9 Organotypic Hippocampal Slice Cultures (OHSCs) 77

5.2.10 Electrokinetic Ejections into Hydrogels 78

5.2.11 Electrokinetic Ejections into OHSCs 80

5.2.12 Two-pipette experiments 81

5.3 RESULTS 82

5.3.1 Properties of the fluorophores, hydrogels, and iontophoresis capillaries 82

5.3.2 Two-pipette experiment 84

5.3.3 Time to steady-state 85

5.3.4 Correlation between ζ-potential and solute penetration distance: 86

5.3.5 Effect of current on concentration and Pe 88

5.3.6 Comparison of Pe_E with Pe_T 89

5.3.7 Small, highly charged solute: 90

5.4 DISCUSSION 91

5.4.1 Fluorophore, hydrogel, and pipette parameters 91

5.4.2 Time to steady-state 92

5.4.3 Solute penetration distance 93

5.4.4 Two-pipette experiments 94

5.4.5 Pe$_E$ versus Pe$_T$ 95

5.4.6 Ejections into OHSCs 98

5.4.7 Conclusion 99

5.4.8 Acknowledgement 99

5.5 SUPPORTING INFORMATION 100

5.5.1 Comsol Simulations:[¥] 102

6.0 A SIMPLE METHOD FOR MEASURING ORGANOTYPIC TISSUE SLICE CULTURE THICKNESS 110

6.1 INTRODUCTION 111

6.2 MATERIALS AND METHODS 112

6.2.1 Chemicals and solutions 112

6.2.2 Tissue culturing procedure 113

6.2.3 Tissue thickness measurements 114

6.2.4 Viability measurements 115

6.2.5 Method validation 116

6.3 RESULTS 117

6.3.1 Tissue culture thickness 117

6.3.2 Viabilty 120

6.3.3 Method validation 120

6.4 DISCUSSION 120

REFERENCES 123

LIST OF TABLES

Table 3.1. Values of μ_{ep} in HBSS 22

Table 3.2. A summary of the average observed mobilities in tissue and their SEMs 30

Table 3.3. Dye concentrations 40

Table 3.4. CE parameters.. 40

Table 4.1a. Comparison of observed mobilities 55

Table 4.1b. Comparison of variances 55

Table 4.2a. Comparison of ζ-potential and tortuosity of the two experimental methods............ 56

Table 4.2b. Comparison of variances 56

Table 4.3a. Comparison of ζ-potential and tortuosity of the two analysis methods.................... 57

Table 4.3b. Comparison of variances 57

Table 5.1. Hydrogel compositions... 74

Table 5.2. Fluorophore properties[a] 82

Table 5.3. Hydrogel Properties.. 83

SI Table 5.1. Experiment summary table.. 101

Table 6.1. Values corresponding to Figure 6.1.. 118

LIST OF FIGURES

Figure 2.1. EO sampling of fluorescent beads 9

Figure 2.2. EO sampling of Thioglo-1 10

Figure 2.3. EO cell loading of calcein AM 12

Figure 2.4*. Fluid velocity as a function position 13

Figure 3.1. The apparatus 21

Figure 3.2. Experimental sequence 27

Figure 3.3. Intensity profiles 28

Figure 3.4. Effective mobility in tissue as a function of the electrophoretic mobility 29

Figure 3.5. A micrograph of an organotypic hippocampal slice culture 31

Figure 4.1. The apparatus 50

Figure 4.2. Sample experimental run 53

Figure S- 4.1. Circuit diagram of the differential amplifier in the four-electrode potentiostat. ... 64

Figure 5.1. Hydrogel cell 78

Figure 5.2. OHSC experimental setup 80

Figure 5.3. Two-pipette experiment 84

Figure 5.4. Solute penetration distances 87

Figure 5.5. Effect of current on concentration and Pe 88

Figure 5.6. Steady-state Pe_E vs. Pe_T 89

Figure 5.7. Injections into an OHSC 90

SI Figure 5.1. Steady state versus non-steady state 100

SI Figure 5.2. Comsol Simulation 105

SI Figure 5.3. Effects of mismatched ζ-potentials 106

SI Figure 5.4a. Digital Midgard^{TM} experimental circuit 108

SI Figure 5.4b. PAR experimental circuit 108

Figure 6.1. Measured thicknesses over time 117

PREFACE

The successful completion of my PhD reflects the patience, encouragement, and intellectual contributions of many individuals along the way. I am most grateful to my parents, Avital and Shimon, who have supplied endless reassurance and strength. They showed me the value of education and were my strongest champions. Deepest thanks go to my brother, Nir, who inspires me to become a happier, more fulfilled person every day. I want to express great appreciation for Todd Bindrim, who supported, listened, and took an interest when I needed it most.

Many thanks go to the people who make up the Department of Chemistry at the University of Pittsburgh. Thank you to each member of the Weber lab, both past and present. You have been good friends and colleagues throughout the years. I would especially like to thank past members Moon Chul Jung and Imants Zudans for their mentorship, technical support, and friendship. To my incredible friend and colleague, Xiaomi Xu, I owe my sanity and motivation to persevere. Thanks to Ryan Stayshich for friendship and library study time. I would especially like to thank Amy Hamsher and Amir Faraji for being both good friends and superb colleagues on this project. Thanks go to Yanhong Yang for being a good friend and supporter. To Manyan Wang, thank you for your efforts in working through the details.

I count myself very fortunate to have encountered some of the best hearted people in the Department of Chemistry. Kind words of the staff within the department made the graduate school years possible, to which a special thank you goes to Michele Monaco. To Chuck

Fleishaker, Dave Emala, and Bob Muha, your endless work has made this dissertation possible-thank you. A very sincere gratitude goes to Jeff Sicher and Tom Gasmire for their creativity and hard work, and mostly for their encouragement.

I am deeply grateful to my advisor, Prof. Stephen Weber, for his guidance and support, and for the many hours spent reading my manuscript and offering useful input. He allowed me to explore my scientific creativity and solidify my scholarly work. I am very grateful to the members of my committee, Prof. Adrian Michael and Prof. Shigeru Amemiya, who have supported me and have taught me to think carefully and purposefully. I owe my scientific bearing to Prof. Mats Sandberg, who introduced me to a new avenue of neuroscience research. Thank you, Mats, for your extensive technical expertise on this project.

This dissertation is dedicated to my two grandmothers, who believed in the value of higher education and a woman’s ability to achieve her goals.

1.0 INTRODUCTION

Studies of electric fields in the brain focus on the effects of endogenous electric fields, environmental electric fields, and stimulation using electric fields for clinical and research purposes. The brain creates endogenous electric fields in the process of communication between neurons. Electric fields are naturally created in the synapse with ion channel openings.[1] Furthermore, local field potentials occur where extracellular (EC) potential fluctuations contribute to synchronizing groups of firing neurons.[2] Orientation of those neurons can further amplify EC electric fields produced by synchronized firing.[3]

Some treatments of neurological diseases are based on the application of electric fields to the brain. Deep brain stimulation is one such treatment that uses electric fields to treat the physical effects of Parkinson's disease, such as tremors.[4] Transcranial magnetic stimulation[5-8] and electric stimulation[9-12] are clinical techniques that are used to treat depression and in stroke rehabilitation. Furthermore, seizures are controlled with the application of electric fields in the brain.[13] Electric fields are also used to achieve electroporation in the brain in order to abolish tumors[14] or for genetic manipulation.[15] In electrophysiology, electric fields are used to stimulate single or small groups of neurons[16] and even to direct neuronal growth[17]. Electric fields are used in solute delivery methods, such as localized[18-20] and transnasal iontophoresis[21]. Despite the presence of endogenous electric fields and the use of exogenous electric fields, the degree to which electric fields in the brain motivate EC solute transport is unknown.

1.1 ELECTROKINETIC TRANSPORT

An electric field applied across a porous medium, such as brain tissue, may produce electrokinetic transport, depending on the nature of the solute and the EC environment. Cell membranes and stationary EC matrix components include phospholipid head groups, proteins, sulfated carbohydrates, and the like that ionize in the presence of an electrolyte solution such as cerebrospinal fluid. An electric field in tissue with surface charges creates an electrokinetic bulk fluid flow called electroosmotic flow (EOF). The charges on cell surfaces and fixed EC matrix components affect the spatial distribution of ions in the EC fluid. A concentration gradient of ions forms near the charged surface: counterions concentrate near the surface, and coions are in low concentration.[22] At a distance of 1 to 10 nm away from the charged surface, the ion distribution in the bulk solution reaches electroneutrality. EOF arises by virtue of the charge distribution in solution and the externally applied electric field.

The electric potential at the slip plane between the moving and stationary ions is termed the ζ-potential.[22] The magnitude of ζ-potential controls the magnitude of the EOF. Electrosmosis, electrophoresis, and streaming current/ streaming potential are common techniques used to experimentally determine the ζ-potential of a stationary surface in a porous medium or a conduit. EOF governs the observed velocity, v_{obs}, of a neutral solute under the influence of an electric field, E. Measuring v_{obs} can be used to determine the ζ-potential, ζ, of the surface. The velocity of the neutral solute is described by the Helmholtz-Smoluchowski equation:

$$v_{\mathrm{obs}} = v_{\mathrm{eo}} = {}^{-\varepsilon\zeta}/_{\eta}\, E = \mu_{\mathrm{eo}} E \qquad (1)$$

where ε and η are the permittivity and viscosity of the medium, respectively. The electroosmotic (EO) mobility, μ_{eo}, is directly related to the ζ-potential of the charged surface.

The ζ-potential of a particle can be determined in much the same way. The surface charges on the particle define its ζ-potential. The migration of charged particles under an electric field, independent of the ζ-potential of the matrix, is called electrophoresis. The ζ-potential of a particle is related to its electrophoretic mobility, as described by Equation 2.

$$v_{\mathrm{ep}} = \mu_{\mathrm{ep}} E = {}^{\varepsilon\zeta_{\mathrm{particle}}}\!/_{\eta}\, E \qquad (2)$$

The electrophoretic velocity, v_{ep}, is a property of the solute related to its mobility, μ_{ep}. The net migration of the solute is zero when μ_{ep} directly opposes μ_{eo}. If μ_{ep} is known, the ζ-potential of the surface can be calculated using Equation 1.

Determination of ζ-potential using streaming currents includes a pressure gradient, sometimes resulting from gravitational or centrifugal forces.[23] Electrodes are placed on either side of the pressure gradient across the charged channel or porous matrix. The current at which the electrode potentials are equal is defined as the streaming current. The streaming current, i_{str}, is used to calculate ζ-potential by the following relationship:

$$i_{str} = {}^{\varepsilon\zeta}\!/_{\eta} \left({}^{\mathrm{a}^2 \Delta \mathrm{P}}\!/_{\mathrm{L}} \right) \qquad (3)$$

where a is the pore radius, ΔP/L is the pressure gradient between the electrodes.

1.2 PHYSICOCHEMICAL BRAIN PROPERTIES

ζ-potentials of isolated biological particles are often determined by measuring their electrophoretic velocities. ζ-potentials have been determined for isolated cells,[24, 25] EC constituents,[26] and synaptosomes[27]. The ζ-potential of cartilage models composed of bone fragments has also been investigated.[28] In general, ζ-potentials of intact biological tissue have not been measured. However, EOF has been quantified in intact skin tissue to understand transdermal iontophoresis. Iontophoresis is an electrokinetic method used to drive solutes into tissue using an applied electric field. Research in transdermal iontophoresis has found that skin pores have an appreciable ζ-potential and the bulk of skin tissue has zero ζ-potential.[29, 30] Ranck estimated brain tissue ζ-potential to be approximately -15 mV by using previously determined ζ-potentials of cell plasma membranes.[31] This dissertation is mainly focused on the determination of brain tissue ζ-potential and tortuosity and applying the knowledge to iontophoresis and reverse iontophoresis (EO sampling).

EC solute transport is dependent on the geometry of the EC space and solute size and shape. Outside of electrokinetic phenomena, solute transport over distances greater than the synapse occurs by diffusion. EC diffusional transport has been thoroughly investigated.[18] Tetramethylammonium ion (TMA^+)[32-58] , dextrans[36, 59-62] and other polymers,[63-65] albumin,[60] radiotracers,[66-69] neurotransmitters,[33] and other molecules[44, 61, 70-75] have been used as solutes for diffusion experiments in the brain to investigate tortuosity. Tortuosity is a quantitative measure of the twists and bends of the EC space. Various definitions of tortuosity exist. Volumetric tortuosity is defined as a purely geometric length ratio: the effective distance a solute must travel in the EC space between two points divided by the linear distance between those two points, i.e., as if there were no obstacles in the solute's path.[76] definition of volumetric tortuosity is valid where the solute path is restricted to a single axis. The Multiple three dimensional pathways in the brain, cannot be described by distance of the solute path. Therefore, neurobiologists define tortuosity as apparent tortuosity. The square of the apparent tortuosity is equal to the ratio of a diffusion coefficient in free solution to the diffusion coefficient in the tissue matrix, i.e., apparent diffusion coefficient.[18] The apparent diffusion coefficient, and thus apparent tortuosity, accounts for the three dimensional structure of the EC space, the solute properties, such as size and shape, and any frictional or viscous drag the solute experiences in the EC space.

Different areas of the brain have different values of tortuosity, and anisotropy can exist within individual brain regions. The methods used to determine ζ-potential described in this dissertation require solutes to travel through the EC space under the influence of an electric field, and therefore subject solute movement to the tortuous environment of the brain.[77, 78] We designate this tortuosity electrokinetic tortuosity. Electrokinetic tortuosity describes the possible dependence of solute flow on pore orientation with the electric field.[79, 80] Published methods of determining diffusional tortuosity in the brain measure diffusional tortuosity, absent of an applied electric field.[81, 82] Both ζ-potential and electrokinetic tortuosity of tissue can be defined using the experimental methods described later.

1.3 THE MODEL SYSTEM: ORGANOTYPIC HIPPOCAMPAL SLICE CULTURE

In order to determine the ζ-potential of brain tissue, which had not been determined before the research presented here, we need an appropriate experimental platform. Organotypic hippocampal slice cultures (OHSCs) are used in electrophysiology and pharmacology experiments.[83] OHSCs serve as an *in vitro* model system for the brain for determining the ζ-potential and electrokinetic tortuosity. There are two different preparations of OHSCs: roller tube and interface. Both methods start with acute tissue slices that are extracted from specific brain regions and sliced at 100 to 500 μm thick. The roller tube preparation embeds the tissue slice in a plasma clot or collagen matrix on a microscope coverslip and the tissue is rotated slowly during incubation. This preparation yields a monolayer of cells that retains the cytoarchitecture of the original tissue slice. The interface preparation, originally developed by Stoppini, places slices on a porous hydrophilic PTFE membrane.[84] The tissue is incubated over medium, such that nutrients from the medium permeate through the membrane into the tissue from below and oxygen is obtained from above. The initial thickness is critical for the interface method. Tissue slices larger than 500 μm are likely deprived of oxygen and nutrients. The interface method yields three dimensional cultures, about 4 cell layers thick, in which the cytoarchitecture and biochemistry are largely retained. This research employs the interface OHSC method.

OHSCs are ideally prepared with early postnatal rat pups, p0 to p10. At this age, the brain is easiest to dissect, brain regions are mostly established, and cells have a higher rate of survival following the surgical process. Some cell adaptability still exists, such that once in culture, the tissue slice recovers from the trauma of explantation with a degree of synaptic rearrangement. Thus, complete tissue systems are established. Explantation from adult rats is possible, but requires oxygenation to avoid necrosis. Therefore, we chose to explant tissue from p6-p9 rats.

The hippocampus is the most widely studied organotypic culture using the interface technique. The hippocampus is part of the limbic system of the brain, and plays an important role in learning spatial navigation and long-term memory. The hippocampus is one of the main brain regions affected by Alzheimer’s disease, epileptic seizures, and ischemic conditions such as stroke. Each OHSC contains the laminar structure of the hippocampus. Pyramidal cells make up the cornu ammonus (CA), which is itself divided into 4 subgroups: CA1, CA2, CA3, and CA4. The CA2 and CA4 are small relative to the CA1 and CA3 and are often not pointed out in morphological studies. Granule cells make up the dentate gyrus. The dentate gyrus sits at the end of the CA4. Signals travel along the laminar structure from the dentate gyrus to the CA1. OHSCs also include the subiculum and entorhinal cortex. The CA1 dispatches signals to the subiculum. Both the subiculum and entorhinal cortex subregions contain axons that project to other brain regions. The laminar structure of the hippocampus has been shown to generate endogenous EC electric fields of tens of millivolts per millimeter by the synchronous activation of multiple neurons.[3]

1.4 QUANTITATIVE ANALYSIS OF THE EXTRACELLULAR SPACE

Quantitative analysis of solutes in the EC space in living systems has proven difficult. EC sampling can provide insight to EC solute concentrations, but the available methods bear disadvantages. Microdialysis uses a probe to sample a broad spectrum of solutes, but the probe damages the surrounding tissue.[85, 86] Thus, results are a consequence of a perturbed system. Furthermore, the time resolution of published microdialysis samples is on the minutes timescale.[87] Other methods, such as chronoamperometry and fast-scan cyclic voltammetry (FSCV) use microelectrodes that are small in diameter, avoiding cell death as a result of probe placement. FSCV has millisecond time resolution, but can only detect changes in levels of electrochemically active species.[87-89] Micropush-pull sampling uses induced pressure to sample from the EC space. Disadvantages of this sampling method include sample dilution, mixing, and inferior time resolution to FSCV.[90-92]

Ranck's estimation of a brain tissue ζ-potential of -15 mV[31] leads to the possibility of motivating electrokinetic flow in the EC space of the brain via an applied electric field. Provided a significant ζ-potential, such as -15 mV, electrokinetic flow can be directed within the brain. This implies that EOF could be therefore be directed from the brain and into a conduit such as a sampling capillary for separation and analysis of the EC contents.

2.0 INITIAL MOTIVATION

We have proposed an EC sampling method using the principles of electrokinetic forces. The method would include the advantages of sampling a broad spectrum of analytes and short time resolution, without damaging cells in the sampling region. The basic principles of this sampling idea, termed EO sampling, were tested by sampling fluorescent beads into a fused-silica capillary, as shown in Figure 2.1.

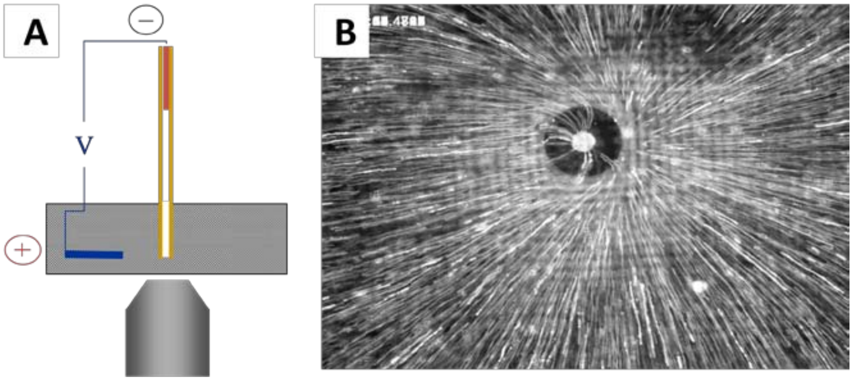

Figure 2.1. EO sampling of fluorescent beads

A: A 50 μm inner diameter (30 cm long) fused-silica capillary, filled with electrolyte solution, is placed in a suspension of 2 μm diameter fluorescent beads over an inverted fluorescence microscope objective lens. The distal end of the capillary is in a vial containing electrolyte solution and a platinum electrode. A circuit is created such that the electric field emanates in the bath and into the capillary. B: Fluorescent bead position tracking shows the beads moving into the lumen of the capillary with the application of voltage.

Figure 2.1 displays the tracked positions of the fluorescent beads over a period of time in which an electric field is applied. The beads are transported into the capillary lumen by virtue of EOF produced in the capillary. Therefore, Figure 2.1 shows that we are able use EO sampling to sample from an electrolyte bath, into a fused-silica sampling capillary.

By knowing the overall ζ-potential of brain tissue and applying an electric field through the brain, we can direct EOF within the EC space. EOF can be directed from within the brain into a conduit to sample electroosmotically. Furthermore, we can direct fluid flow from the conduit into the brain as a possible application for drug delivery. EOF also could be useful for encouraging volume transmission within the EC space. Figure 2.2 demonstrates EOF directed from below an OHSC membrane, through the OHSC, and into a sampling capillary.[93]

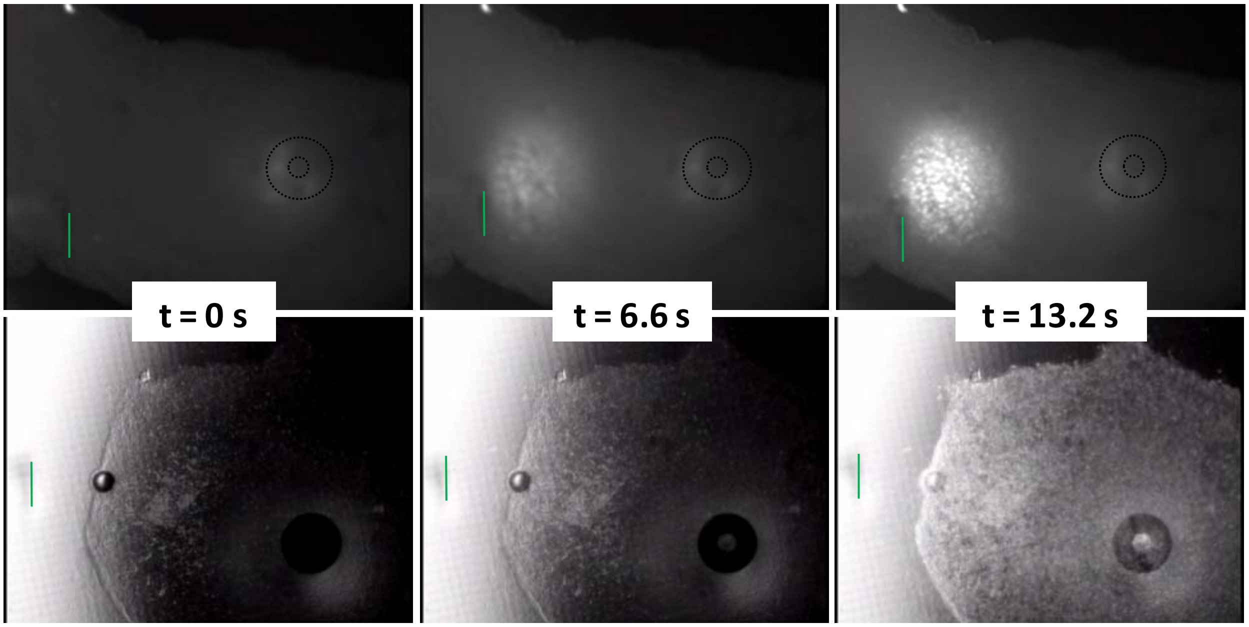

Figure 2.2. EO sampling of Thioglo-1

The injection capillary, filled with Thioglo-1, is placed over a gold minigrid and under the OHSC membrane. The edge of the injection capillary is indicated by a green line. A sampling capillary is placed orthogonally to the OHSC. The lumen of the sampling capillary is emphasized by the dotted circle in the top row, where it was otherwise not obvious. The top row displays the injection of Thioglo-1 in the case where no voltage is applied between the gold minigrid and the sampling capillary. The bottom row displays the progression of a similar injection of Thioglo-1, while 3 kV are applied. An inverted fluorescence microscope (4X objective lens) imaged the experiments.

The control experiment in the top panel shows the pressure ejection of Thioglo-1 under the OHSC membrane. Thioglo-1 fluoresces in the presence of cell thiols, mainly glutathione. Cells near the ejection capillary (indicated by the green line) fluoresce over time as Thioglo-1 diffuses into the OHSC. By contrast, application of an electric field through the OHSC and into the sampling capillary, as shown in the bottom panel of Figure 2.2, directs Thioglo-1 into the OHSC under the sampling capillary lumen by virtue of EOF. Thus, this set of experiments shows that the principles EOF can be used for EC sampling.

Interestingly enough, the same basic experiment can be used to measure enzyme kinetics. Such is the example with calcein acetoxymethyl (AM) ester shown in Figure 2.3. The top series shows the control experiment in which calcein AM diffuses from below the OHSC membrane and into the OHSC without an applied electric field. The OHSC does not fluoresce after 15 minutes, indicating calcein AM has not diffused into the cells. The second series shows the same setup under the influence of an electric field. After 15 minutes, the cells under the sampling capillary fluoresce. Uncharged calcein AM enters living cells, and esterases within the cell hydrolyze calcein AM generating a fluorescent green calcein complex.[94] Calcein AM hydrolysis generally takes 15 minutes to 1 hour.[95, 96] Therefore, Figure 2.3 indicates EOF of calcein AM occurred almost instantly with the application of electric field. Cell death analysis of OHSCs confirms no additional cell death occurs as a result of EO sampling under controlled conditions.[97]

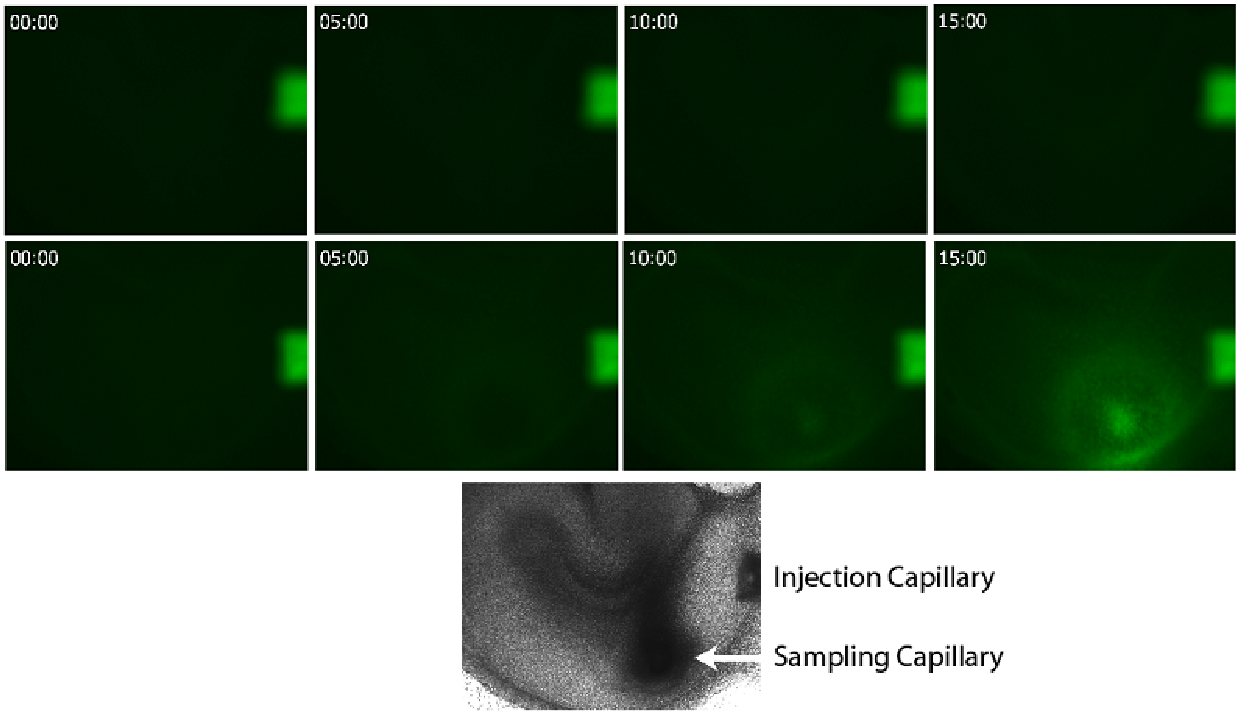

Figure 2.3. EO cell loading of calcein AM

The images are taken at 5 minute intervals using an inverted fluorescence microscope. The fluorescent injection capillary filled with calcein AM lies under the OHSC membrane. We replaced the gold minigrid used in experiments described earlier (refer to Figure 2.2) with a platinum electrode. The top series shows the control experiment where calcein AM has been injected under the membrane without application of voltage. The bottom series shows the application of 1.8 kV following calcein AM injection. After 15 minutes, cells in the bottom panel fluoresce. The bottom image shows a bright field image of the OHSC with the injection capillary under the OHSC membrane and the sampling capillary orthogonal to the OHSC.

Using capillary electrophoresis, the ζ-potential of a fused-silica capillary filled with physiological buffer, such as those shown in the previous three figures, was found to be approximately -50 mV - more than double that of an OHSC.[77, 78] Despite the ζ-potential mismatch at the capillary-OHSC interface, simulations of EO sampling show a relatively low pressure generated at the interface of the capillary and the OHSC under fairly aggressive conditions (-2000 V, with a 30 cm-long 100 μm inner diameter capillary) however there is nonetheless a pressure-induced flow generated. Three dimensional Comsol simulations using the geometry described above show that the fluid velocity in the sampling capillary is lower due to pressure created by a ζ-potential mismatch (refer to Figure 2.4*) in comparison to the case where there is no mismatch. On the other hand, an increase in fluid velocity occurs at the same time within the simulated OHSC.

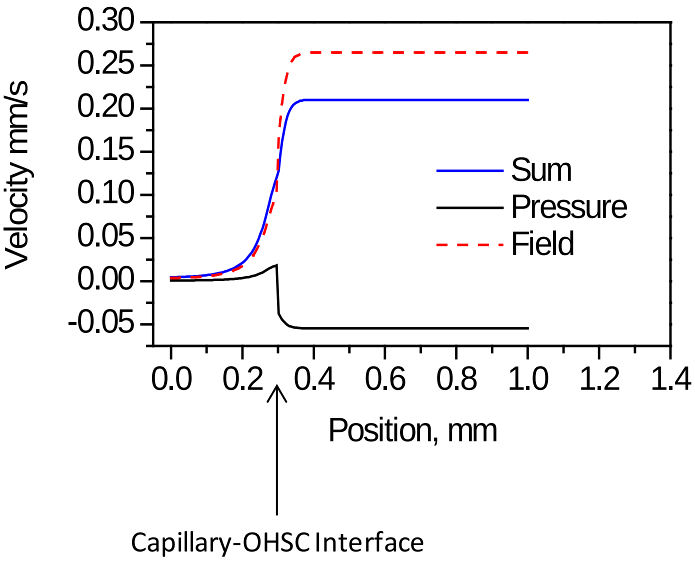

Figure 2.4*. Fluid velocity as a function position

***Courtesy of Dr. Imants Zudans. Fluid velocity as a function position is separated into two components: the pressure-induced velocity (black line), and the EO velocity (shown as a red dashed line). The sum of the two velocities (shown in blue) is the observed fluid velocity. The capillary ζ-potential is set to -50 mV and the OHSC ζ-potential to -15 mV. The OHSC is 300 μm thick, hence the interface is at position 0.3 mm on the plot. A schematic of the setup is shown to the right of the plot.**

In this chapter, we were able to prove that EOF can be produced in an OHSC. Moreover, EOF can be directed from the OHSC into a sampling capillary. Pressure-induced flow during EOF sampling likely exists due to a ζ-potential mismatch between the OHSC and the sampling capillary. In order to quantitatively understand EO sampling from the OHSC EC space, we need to know the ζ-potential of the OHSC.

3.0 DETERMINATION OF ZETA POTENTIAL IN RAT ORGANOTYPIC HIPPOCAMPAL CULTURES

This work is published in *Biophysical Journal* **2008**, 94 (11), 4561-4569.

ABSTRACT

ζ-potentials of entities such as cells and synaptosomes have been determined, but ζ of brain tissue has never been measured. Electroosmotic flow, and the resulting transport of neuroactive substances, would result from naturally occurring and experimentally or clinically induced electric fields if ζ is significant. We have developed a simple method for determining ζ in tissue. An electric field applied across a rat organotypic hippocampal slice culture (OHSC) drives fluorescent molecules through the tissue by both electroosmotic flow and electrophoresis. Fluorescence microscopy is used to determine each molecule's velocity. Independently, capillary electrophoresis is used to measure the molecule's electrophoretic mobilities. The experiment yields ζ-potential and average tissue tortuosity. The ζ-potential of OHSCs is –22 ± 2 mV and the average tortuosity is 1.83 ± 0.06. In a refined experiment, ζ-potential is measured in various subregions. The ζ-potentials of the CA1 stratum pyramidale, CA3 stratum pyramidal and dentate gyrus are -25.1 ± 1.6 mV, -20.3 ± 1.7 mV and -25.4 ± 1.0 mV respectively. Simple dimensional

arguments show that electroosmotic flow is potentially as important as diffusion in molecular transport.

3.1 INTRODUCTION

An understanding of brain function, especially extracellular transport, requires a quantitative understanding of the physicochemical properties of the extracellular space. Diffusion in the extracellular space of the brain and slice preparations is fairly well understood. Nicholson[98, 99] and Sykova[100] measured the transport of tetramethylammonium ion (TMA$^+$) and polymers to reveal the details of extracellular diffusion. Other methods such as cortical surface photobleaching,[101] magnetic resonance,[102-105] integrative optical imaging,[106] and dual-probe microdialysis[107, 108] have been used to evaluate the diffusive transport of markers and biomolecules as well as water in living brain tissue. A detailed understanding of variations in diffusion caused by changes in extracellular volume fraction has led to applications of these techniques in assessing, e.g, edema.[101] The dimensions of the intercellular space have been determined by measuring particle diffusion rates.[109] Tortuosity has a large effect on transport rates in heterogeneous media. Tortuosities vary depending on the local geometry of the tissue.[110, 111] In addition, certain brain regions are anisotropic[112] leading to a valuable method in magnetic resonance imaging called "diffusion tensor imaging".[102, 105] We conclude that there is a rather firm understanding of diffusive transport in the brain, which is critical for understanding extrasynaptic (paracrine or volume) transmission,[113, 114] neuronal development[115] as well as for making inferences from measurements.[89, 116]

On the other hand, there is less known about electrically mediated transport in the brain. Electric fields and currents in heterogeneous media create a fluid flow, called electroosmotic (EO) flow, by virtue of the field's motivating force on the mobile counterions to fixed charges on surfaces or immobile macromolecules in the extracellular space. The fixed charges create a ζ-potential, the potential at the shear plane between a charged surface and a moving electrolyte solution[22]. The magnitude of the ζ-potential controls the magnitude of the EO flow. The ζ-potential in brain tissue is a consequence of cell-surface functional groups, such as phospholipids, proteins, and carbohydrates as well as fixed components of the extracellular matrix.

The focus of this work is to create and apply a method for the determination of the ζ-potential in nervous tissue. In the paragraphs below, we justify the need to understand this currently undetermined parameter of brain tissue, and demonstrate how a method similar to electrophoresis can be used.

Certainly, electric fields naturally occur in brain. Recently, Savtchenko et al. showed how the electrical field created in the synapse during ion-channel opening can influence molecular transport in the synapse, normally viewed as occurring by diffusion.[117] Several clinical techniques such as transcranial direct current stimulation[118-121] and magnetic stimulation,[122-125] also create electric fields in brain.[126] These treatments are effective in depression,[120, 123] stroke,[119] and other diseases. Electric fields are also used in seizure control.[127] In research laboratories, electric fields are applied to brain tissue to direct neuronal growth,[17] to perform iontophoresis in the brain,[128] carry out electroporation in brain[15] and embryos,[129, 130] and for transnasal delivery of a charged peptide (by an electric field created between the nasal cavity and the back of the head[21]). As far as we are aware, EO flow is largely overlooked in these endeavors.

EO flow and/or ζ-potential have been measured in some biologically relevant matrices by a variety of techniques. EO flow is knowingly created in transdermal iontophoresis.[30, 131-136] EO dewatering of tumors also depends on the existence of a ζ-potential within tissues.[17, 137] Outside the fields of transdermal iontophoresis and transdermal sampling (reverse iontophoresis[136, 138]), measurements of ζ-potential, or EO mobility, are rare in biological systems. Values of ζ-potential have been reported for isolated cells using electrophoresis,[139] microelectrophoresis,[140] and microcapillary electrophoresis on a chip.[141] Electrophoretic methods have also been applied to bone particles[142] as well as isolated nuclei,[143] vesicles,[144] and synaptosomes[145] from brain tissue. Measurements of transport through tissue, such as skin that can act as a film separating two liquid phases, are based on quantitative determination of the flux of a solute from a "source" phase to a "receiving"' phase. Similarly, EO mobility in plant tissues[146] can be made this way. Alternative measurements using an oscillating electric potential,[147] or scanning electrochemical microscopy on individual skin pores are also used.[30] None of these methods is suited to whole brain, acute brain slices, or slice cultures.

At a more fundamental level, knowing the ζ-potential in intact tissue is vital to understanding molecular movement between cells. Electroosmosis has been proposed as a contributor to learning and memory[31] Even local electric fields, such as those that materialize during epileptic seizures, may generate fluid motion. In tissues other than brain, i.e., lung[148] and epithelial tissue,[149] naturally occurring potential gradients are thought to drive fluid flow. A mathematical theory, including double layer overlap and coupling of mechanical and electrical forces, has been applied to glycogen-containing cartilage models.[28]

We conclude that EO phenomena have been studied in tissues where it clearly must contribute to the observed phenomena, e.g., skin (iontophoretic drug delivery and sampling) and bone (stimulated bone growth). However, there is virtually no understanding qualitatively, and certainly no understanding quantitatively of the ζ-potential in nervous tissue.

We have developed a method to measure EO mobility, thus ζ-potential as well as average tortuosity in organotypic slice cultures of the rat.[84] The velocities of fluorescent molecules are measured in the cultured tissue under an applied field. Data analysis is guided by simple theory, shown below.

3.1.1 Theory

Consider a set of fluorescent molecules with various electrophoretic mobilities. A spot consisting of a single fluorophore is placed in an OHSC. In an electric field, the fluorophore will move at an observed velocity, v_{obs}, as given in Eq. 1, which can be inferred from Boyack and Giddings(62) and Rathore et al.(63)[150, 151] (λ_ε=tortuosity; v_{eo}=electroosmotic velocity; v_{ep}= electrophoretic velocity):

$$v_{obs} = \left(1 \big/ \lambda_e^{\,2} \right)\left(v_{eo} + v_{ep} \right) \tag{1}$$

We assume that v_{eo} and v_{ep} experience the same tortuosity. Note that the definition of tortuosity is consistent with Boyack and Giddings[150] and Rathore et al.[151] We denote that the tortuosity influences an electrokinetic process with the subscript "e". This tortuosity may not be the same as the ratio of free and effective diffusion coefficients (see Discussion for more detail). Equations 2 and 3[22, 151] define the velocities as the products of mobilities, μ, and a field, E.

$$v_{ep} = \mu_{ep} E \tag{2}$$

$$v_{eo} = -\frac{\varepsilon\zeta}{\eta} E = \mu_{eo} E \tag{3}$$

Equation 3 shows that μ_{eo}, is a function of ζ, the ζ-potential, the medium's viscosity (η) and permittivity (ε). Values of μ_{ep} can be determined for each fluorophore independently in HBSS by CE; thus they are known quantities. The observed mobility, μ_{obs}, can be defined as Eq. 4 for an individual fluorescent species. If the tortuosity is not dependent on the fluorophore, a plot of μ_{obs} versus μ_{ep} will yield a straight line with a slope of $\left\langle 1/\lambda^2 \right\rangle$ where the brackets indicate "average". The intercept provides μ_{eo}, and thus ζ.

$$\mu_{obs} = \frac{v_{obs}}{E} = \left(1/{\lambda_e}^2 \right)\left(\mu_{ep} - \frac{\varepsilon\zeta}{\eta} \right) = \left(1/{\lambda_e}^2 \right)\left(\mu_{ep} + \mu_{eo} \right) \tag{4}$$

Another approach involves the use of two molecules simultaneously (molecule 1 and molecule 2). Each molecule is independently described by Eq. 5. Thus the term λ^2/E can be eliminated, as shown in Eqs. 6 and 7 (subscripts 1 and 2 refer to individual molecules).

$$\mu_{eo} = \frac{v_{obs}{\lambda_e}^2}{E} - \mu_{ep} \tag{5}$$

$$\mu_{eo} = \left(\frac{v_{obs1}}{v_{obs2}} \right)\left(\mu_{eo} + \mu_{ep2} \right) - \mu_{ep1} \tag{6}$$

$$\mu_{eo} = \frac{\left(\frac{v_{obs1}}{v_{obs2}} \right)\left(\mu_{ep2} - \mu_{ep1} \right)}{1 - \left(\frac{v_{obs1}}{v_{obs2}} \right)} = -\frac{\varepsilon\zeta}{\eta} \tag{7}$$

3.2 MATERIALS AND METHODS

3.2.1 Chemicals and solutions

The following materials were purchased from Sigma (St. Louis, MO) and were used as received. The culture medium contained basal medium Eagle (50%), Earl's basal salt solution (20%), horse serum (23%), penicillin/streptomycin (25 units/ml), L-glutamine (1 mM), and D-(+)-glucose (7.5 g/L). The culture medium was stored in a refrigerator and warmed to 37°C before use. Gey's Balanced Salt solution (GBSS) was supplemented with 27.5 mM D-(+)-glucose and 2.7 mM $MgSO_4$. The following solutions were prepared with 18 MΩ purified water from a Millipore Synthesis A10 system (Millipore, Billerica, MA): NaOH solutions, HEPES-buffered salt solution (HBSS) containing (mM): 143.4 NaCl, 5 HEPES, 5.4 KCl, 1.2 $MgSO_4$, 1.2 NaH_2PO_4, 2.0 $CaCl_2$, and 10 D-(+)-glucose. HBSS was filtered, stored in the refrigerator and warmed to 37 °C before use. Approximately 3% agarose type-VII in HBSS filled the apparatus shown in Fig. 3.1.

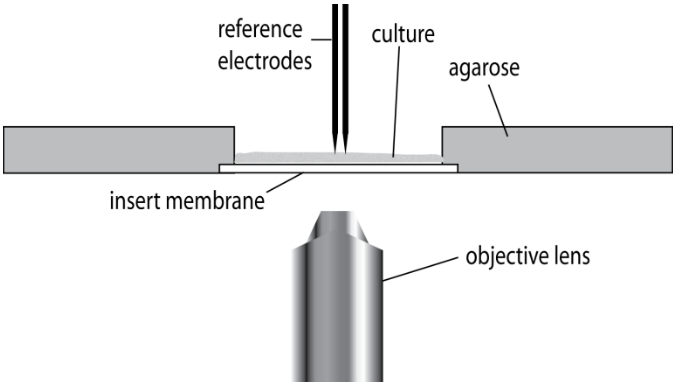

Figure 3.1. The apparatus

The OHSC and its insert membrane are placed against the cast agarose gel. The apparatus is placed on an inverted fluorescence microscope for data acquisition. Reference electrodes measure the field strength near the fluorophore spots.

Each of the fluorescent molecules was diluted with HBSS, filtered, and frozen until use. The concentration of each probe was empirically determined to accommodate its intensity under experimental conditions. See Table 3.3 in Supporting Material, for the concentrations. Fluorescent dextran conjugates **1-6** were purchased from Invitrogen/Molecular Probes (Eugene, OR). **7** and **8** were obtained from Sigma (Table 3.1).

Table 3.1. Values of μ_{ep} in HBSS

Fluorescent Compound	μ_{ep}/(10^{-9} m^2/Vs)	SEM/(10^{-9} m^2/Vs)
AlexaFluor 568 dextran conjugate 10 kDa‡ (**1**)	-1.92	± 0.15
BODIPY FL dextran conjugate 10 kDa‡ (**2**)	-0.89	± 0.22
Fluorescein dextran conjugate 70 kDa‡ (**3**)	-9.75	± 0.82
Oregon Green dextran conjugate 10 kDa‡ (**4**)	-18.0	± 0.1
Rhodamine Green dextran conjugate 3 kDa‡ (**5**)	-1.72	± 0.19
Texas Red dextran conjugate 70 kDa‡ (**6**)	-0.55	± 0.19
Fluorescein sodium salt (**7**)	-26.3	± 0.3
tris(2,2'-bipyridine)ruthenium (**8**)	26.0	± 0.0

‡Dextran conjugate

3.2.2 Instrumentation

3.2.2.1 Capillary electrophoresis:

Electrophoretic mobilities in HBSS were determined using an ISCO Capillary Electropherograph (Lincoln, NE) with vacuum injection (10 s, 0.5 psi) and ultraviolet-visible absorbance detection. A section of the polyimide coating was removed with a low-temperature flame to create the window. New capillaries were flushed with base overnight. Before each series of experiments, capillaries were flushed with 200 μL of distilled, deionized water, followed by the same volume of the running buffer. The high voltage was then applied to the capillary, and the system equilibrated for 5-20 min. All injections included rhodamine B as the EO flow marker, and were performed at ambient temperature (23°C ± 2°C). The EO flow marker is a neutral molecule with a mobility equal to zero. Its velocity in a capillary electrophoresis (CE) experiment is the electroosmic velocity.

CE measurements of mobilities were performed using 360 μm outside diameter (OD) capillaries with inner diameters (IDs) of 40 or 50 μm. The total capillary length ranged from 50.3 to 118.4 cm, with 25.5-48.1 cm from the injection end to the detection window using -9.0 to -22.1 kV. Detection was at 495, 505, or 595 nm. See Table 3.4 for the parameters used for each particular molecule.

3.2.2.2 Apparatus for tissue experiments

The apparatus in Fig. 3.1 was manufactured from Lucite locally. A 40-V direct current power supply (Heath, Benton Harbor, MI) applies a low homogeneous field (~22 V/cm at the tissue) across the organotypic hippocampal slice culture (OHSC). Two Goodfellow (Cambridge, England) tubular platinum electrodes (1 mm OD, 0.1 mm wall thickness, and ~3.8 cm long) were placed into separate cylindrical reservoirs (19 mm in diameter and 12 mm deep) separated by a narrow rectangular channel 44 mm in length. These reservoirs are not shown in Fig. 3.1. The OHSC remained on the insert membrane during the measurements. Electrical contact between the OHSC and the electrodes was made by agarose-containing HBSS.

3.2.2.3 Ag/AgCl electrodes

A pair of in-house fabricated Ag/AgCl microelectrodes measured the potential gradient in the tissue. The electrodes were made from 0.1-mm-diameter silver wire from JMC Ltd. (Hertfordshire, England). Two sets were made: one spaced 0.80–0.90 mm apart and another spaced 0.35–0.40 mm apart. Distances were determined using a scale bar and micrographic images of each individual experiment.

3.2.2.4 Injection capillary

A 250 μm (ID) fused-silica capillary was pulled to a tip (~12 μm OD) using a P-2000 capillary puller from Sutter (Novato, CA). A Sutter MP-285 micromanipulator lowered the capillary into the OHSC. The distal end of the capillary was attached to a Harvard PHD 4400 Hpsi syringe pump (Holliston, MA) with a 50 μL Hamilton Gastight syringe (Reno, NV). The pump delivered fluid at a flow rate of 120 nL/min for ~1 s.

3.2.2.5 Imaging

An inverted fluorescent microscope (Model IX71) with a U Plan Apo 4× objective lens (both from Olympus, Melville, NY) imaged the tissue experiment using a charge-coupled device camera (ORCA-285 Hamamatsu, Hamamatsu City, Japan). Depending on the fluorescent properties, an appropriate cube was chosen. The Olympus fluorescence cubes are a wide interference filter blue cube (exciter 460–495 nm, dichromatic mirror 505 nm, emitter 510-550 nm interference filter) and wide interference filter green cube (exciter 530–550 nm, dichromatic mirror 570 nm, emitter 575 nm interference filter). A Semrock (Rochester, NY) DA/Fl/TA-3X-A Triple-band “Pinkel” filter set (exciter 1 387 nm, exciter 2 494 nm, exciter 3 575 nm, dichromatic mirror: 394–414 nm, 484–504 nm, 566–586 nm, emitter: 457, 530, 628 nm) was used for multiple fluorophore experiments.

Image processing and distance measurements were done with SimplePCI 6.0 software (Compix, Cranberry, PA). Images of the paired Ag/AgCl electrodes using the microscope camera were captured daily to measure the distance between the electrodes. The same was done for measuring IDs of new injection capillaries.

3.2.3 Procedures

3.2.3.1 Hippocampal organotypic slice cultures

The Stoppini culturing method was used with small variations.[84] The procedures described here have been approved by the University of Pittsburgh IACUC. The hippocampi were dissected bilaterally from decapitated, 7-day postnatal Sprague-Dawley albino rats. The hippocampi were cut transversely into 500 μm thick slices with a McIlwain tissue chopper from The Mickle Laboratory Engineering (Surrey, England). The cultures were placed on Millicell membrane inserts from Millipore and incubated over culture medium at 95% air/5% CO_2. Cultures may be incubated for up to 2 weeks. All data reported here are from cultures incubated for 3–7 days. The mean slice thickness in this time period was 148 μm consistent with other reports.[84, 152, 153] On the day of the experiment, 37°C GBSS replaced culture medium, followed by 30 min of tissue incubation. This procedure was repeated once more. Lastly, 37°C HBSS replaced GBSS before the experiment.

Using an X-Acto knife, the insert membrane was cut to liberate the tissue and the insert membrane under it from excess insert membrane. Edges of the insert were left to allow moving the OHSC into the apparatus without damage as in Fig. 3.1. A portion of the agarose gel was cut away to make room for the OHSC. The OHSC was placed into the apparatus in such a way that the insert edges are under the agarose, but the slice is adjacent to the gel, as shown schematically in Fig. 3.1.

3.2.3.2 ζ-potential determination

The tip of the injection capillary, preloaded with fluorescent probe-containing solution at room temperature, was inserted approximately midway (~75 - 150 μm) into the OHSC with the aid of a micromanipulator. The pump delivered ~2 nL of the fluorescent material. On occasion, placing the capillary into tissue alone delivered enough fluorophore by capillary effects. The capillary was carefully pulled out of the slice, and the microelectrodes were placed in the tissue. Before the voltage supply is turned on, the exposure time is set using autoexposure and the SimplePCI 6.0 software begins recording the fluorescence. The voltage supply was switched on, applying ~22 V/cm through the slice. Measurements of electric field and velocity are taken once the electric field stabilizes (a few seconds). Images were acquired once per second. Movement of a fluorophore toward the cathode is defined as positive.

3.2.3.3 Two-fluorophore experiments

Two sets of paired molecules were used. One set was **1** and **7**, and the other set was **3** and **8**. To measure the velocity of each fluorophore simultaneously, the “Pinkel” filter set was used. At first, each fluorophore is injected into an OHSC separately. The separate exposure times are set using the autoexposure command for a two color image in the SimplePCI 6.0 software. A mixture of the paired fluorophores is then injected into a different OHSC for measurement.

3.3 RESULTS

Table 3.1 shows the CE-determined mobilities for each fluorophore. Fig. 3.2 shows images from an experiment in an OHSC. The OHSC received three injections, labeled *A*, *B* and *C*. *A* and *C* are injections into the insert membrane, and *B* is in the OHSC. We find that fluorophore injected into the insert membrane is immobile regardless of the selected fluorophore or applied field. Each point in Fig. 3.2 (*1-8*) functions as an intensity detector. We measure the intensity at each point as a function of time (Fig. 3.3).

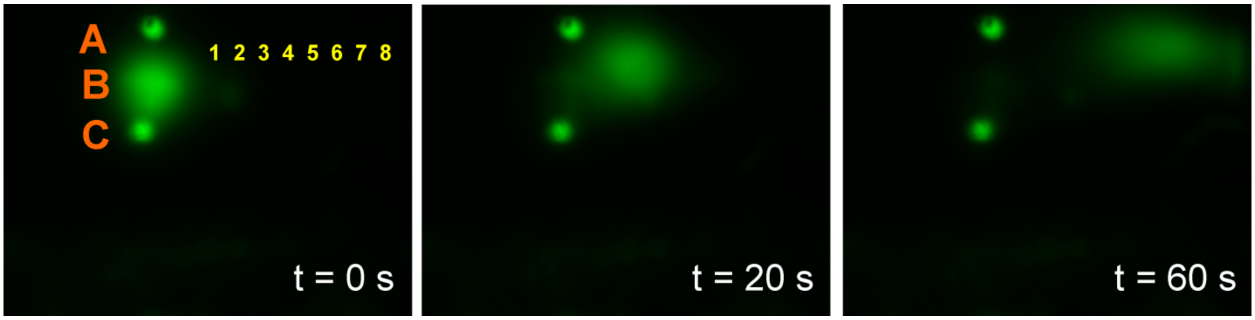

Figure 3.2. Experimental sequence

Alexa Fluor 568 10 kDa dextran conjugate was injected into the insert membrane (injections *A* and *C*) and into the tissue culture (injection *B*). After applying the potential, injection *B* migrates toward the cathode, as shown in the sequence of images. Injections *A* and *C* remain in place despite the electric field. Intensities are measured at points 1-8 as a function of time. The smaller injections *A* and *C* are ~135 μm in diameter. Injection *B* is ~500 μm in diameter.

v_{obs} corresponds to the slope of a plot of the relative positions of the detection points versus the peak times (Fig. 3.3, *inset*). This plot routinely yields straight lines, indicating that fluorophore velocity and electric field are constant during the experiment. Dividing the velocity by the applied electric field, measured using an Ag/AgCl reference electrode pair placed in the tissue, yields the observed mobility (μ_{obs}) as shown in Eq. 4.

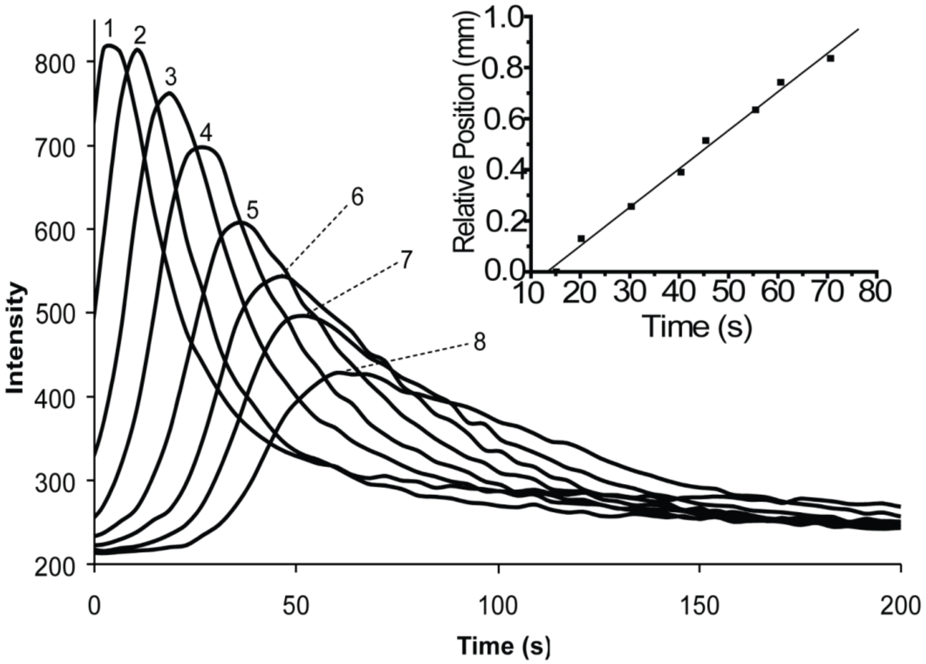

Figure 3.3. Intensity profiles

The intensity profiles recorded at each of the eight detection points on the cathodic side of the original injection. Inset: The relative position of the detection points (1-8) in Fig. 3.2 are plotted as a function of the times of the peak maxima (*inset*). The linearity implies that the fluorophore's velocity is constant throughout the experiment.

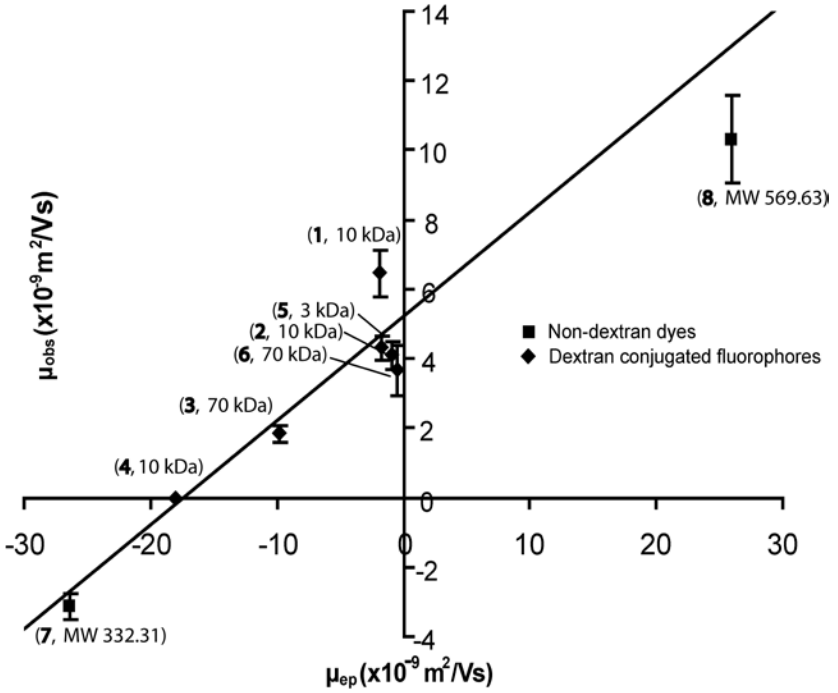

Figure 3.4. Effective mobility in tissue as a function of the electrophoretic mobility

The line is the best fit to all of the data (linear regression). The labels at each point identify the identity of the fluorophore (see Table 3.1) and its molecular weight.

Fig. 3.4 is a plot of μ_{obs} versus μ_{ep}. The errors are the mean ± SE and are also given in Table 3.2. Analysis of the results (linear regression) according to Eq. 4 leads to Eq. 8.

$$\mu_{\mathrm{obs}} \Big/ \left(\mathrm{m}^2 / \mathrm{Vs}\right) = 0.30(\pm 0.02)\mu_{\mathrm{ep}} + 5.2(\pm 0.3)\times 10^{-9} \tag{8}$$

The slope of 0.30 ± 0.02 is equal to the inverse square of the average tortuosity. The average (electrokinetic) tortuosity is therefore 1.83 ± 0.06. The ζ-potential in the OHSC is -22 ± 2 mV.

Table 3.2. A summary of the average observed mobilities in tissue and their SEMs

Fluorophore	μ_{obs} /(10^{-9} m^2/Vs)	SEM/(10^{-9} m^2/Vs)	n
1	6.46	± 0.67	58
2	4.09	± 0.39	19
3	1.85	± 0.24	22
4	0[a]	-	14
5	4.31	± 0.35	13
6	3.66	± 0.71	12
7	-3.15	± 0.39	55
8	10.3	± 1.3	10

[a]No measureable movement

n is the number of experimental runs for that specific fluorophore.

The zeta potential described above is an average from all areas of the OHSC in the direction of the line, as indicated in Fig. 3.5 (approximately along the medial-lateral axis). As noted in the introduction, there are regional differences in the hippocampus. Are there different ζ-potentials in different regions? A micrograph of an OHSC (Fig. 3.5) shows areas interrogated with the two-fluorophore experiments; **1** was paired with **7** in 41 experimental runs. The **3** and **8** pair was run twice.

The CA1 stratum pyramidale, CA3 stratum pyramidale, and dentate gyrus have ζ-potentials (respectively) of (mV) -25.1 ± 1.7 (n = 12), -20.3 ± 1.6 (n = 14), and -25.4 ± 1.0 (n = 34). Analysis of variance reveals that there is a significant difference among the regions ($p < 0.05$), which is accounted for by the difference between the value in CA3 and the other two.

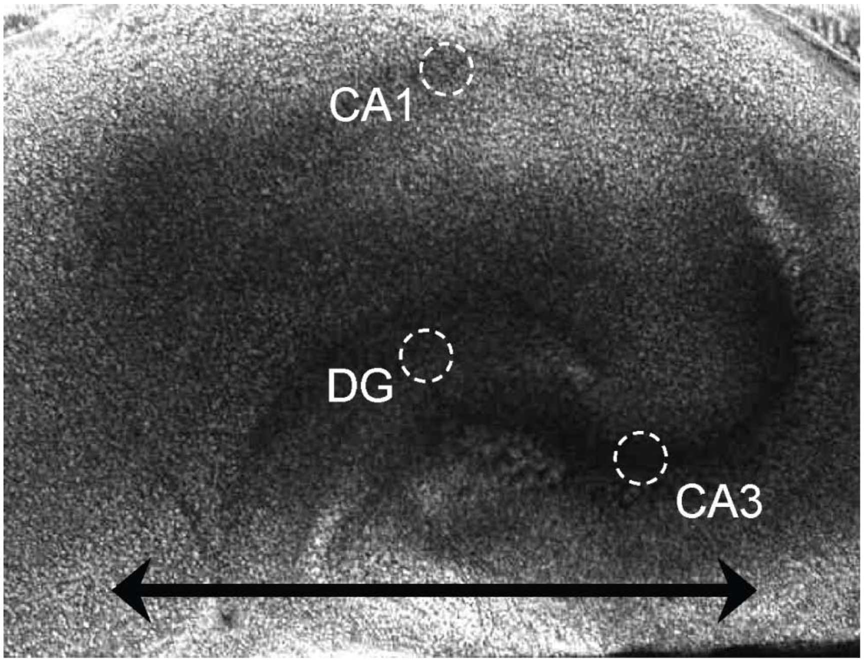

Figure 3.5. A micrograph of an organotypic hippocampal slice culture

The circumscribed areas represent the portions of the CA1, CA3, and dentate gyrus (DG) investigated. The horizontal line represents the direction in which the tortuosity is measured in the single-fluorophore experiment.

3.4 DISCUSSION

3.4.1 Analysis of the method

CE measures the electrophoretic mobility of the fluorophores used in the tissue experiment. As a result of the high electrolyte concentration, we had to modify typical CE procedures. To minimize the effect of thermal gradients, a narrow (40 μm ID) and long (~100 cm) capillary replaces the more common 75 μm ID, 50-cm-long capillary. With the longer, narrower capillary, peak shape is good.

Labeled dextrans (Supporting Materials) are the most successful category of fluorophores for our experiments. Dextran fluorophores are easily visible with a fluorescence microscope; they have minimal “nonspecific” binding;[98, 154, 155] and their CE results are unambiguous. Apparently, the fluorescent labels on each of the dextrans account for their different mobilities.**7** and **8**, both nondextran conjugate fluorophores, also have similar characteristics, thus are acceptable for our study. Several other fluorophores, on the other hand, do not meet the necessary criteria (Supporting Materials).

Although an in vivo model preserves the true environment of tissue, several advantages make the OHSC the optimal model for our purposes. We can easily track temporal changes in tissue slice cultures using an inverted microscope. Moreover, tissue slices are viable models because the cytoarchitecture and electrophysiology are preserved after explantation.[98, 151-153, 156-158] Additionally, cultured slices are easier to manipulate than acute slices.

A tissue culture is easily placed in the apparatus as shown in Fig. 3.1. We use the apparatus to apply a potential gradient along the tissue by providing electrical contact through agarose gel. The design of the apparatus is such that the tissue sits in a narrow channel between two reservoirs, thus increasing the resistance in the channel. The increased resistance amplifies the electric field. The change in depth from the agarose gel to the OHSC further concentrates the field in the tissue. Thus, the field is largest within the OHSC. Applying a large field through a tissue can alter its permeability, or electroporate the cells.[159] Typical fields in electroporation, ~1 kV/cm, are ~45 times larger than the field strengths applied in the apparatus. To isolate the experiment from any electrolysis products created at the platinum electrodes, the electrodes are placed in deep reservoirs far from the tissue. Early designs of the apparatus had much smaller reservoirs. pH-responsive fluorophore experiments showed that electrolysis products moved into the channel within 6 min and altered the properties of the gel. The same pH-responsive fluorophore experiments repeated in the current apparatus design show that the electrolysis products remain in the reservoirs for well over 30 min. This provides plenty of time to run the tissue experiment.

To preserve the integrity of the tissue while injecting fluorescent material, several provisions are taken. Primarily, the injection capillary is pulled to a 12 μm OD tip to minimize tissue damage. A micromanipulator allows control over the depth of the injection. The injection capillary delivers ~2 nL of fluorophore into the tissue to maintain the microenvironment. There is no obvious damage to the tissue as a result of injection.

The membrane insert has completely different properties than tissue. The membrane itself is made of poly(tetrafluoroethene) with a proprietary hydrophilic surface modification. When fluorescent material is injected into the membrane it appears to stay in place (Fig. 3.2, injections *A* and *C*). Therefore, fluorescent compounds moving in the visual field are in fact injected into the tissue and not into the insert membrane.

3.4.2 Analysis of the results

The measured ζ-potential is -22 ± 2 mV. The value is in the range of isolated biological materials, such as mouse N-18 cells measured by a microelectrophoretic apparatus with a ζ-potential of -15 mV,[140, 160] chromaffin granules, -14.4 mV,[144] and rat brain synaptosomes using particle electrophoresis, -11.8 mV.[145] Theoretical calculations determined a cartilage model containing glycogen to have a ζ-potential of -27 mV.[28] Ranck estimated the ζ-potential in brain to be -15 mV based on the constituents of the plasma membranes of neurons and glial cells.[31]

The ζ-potential determined using two fluorophores simultaneously is independent of the average tortuosity factor and field (Eq. 7). The mean ζ-potential from the simultaneous fluorophore experiments is essentially the same as that in the single fluorophore experiments. We infer from this either of two things: the values of the field and tortuosity from the single-fluorophore experiments are correct, or there is a fortuitous cancellation of deterministic errors. We view the latter conclusion as a remote possibility. Thus, the two-fluorophore-experiment further validates the experimental method.

The two-fluorophore method is capable of distinguishing small differences in ζ-potential between different structures in the brain: CA1 (-25.1 ± 1.7 mV), CA3 (-20.3 ± 1.6 mV) and dentate gyrus (-25.4 ± 1.0 mV). The CA1 and dentate gyrus regions have statistically the same ζ-potential at a 95% confidence level. However, a single-factor analysis of variance analysis reveals that there is a statistical difference among the three areas ($p < 0.05$). It is interesting to note that these regions have different vulnerabilities to excitotoxicity correlated with the differences in ζ-potential. The CA1 and dentate gyrus regions are more susceptible to N-methyl-D-aspartic acid excitotoxicity than the CA3 region.[161] Perhaps the ζ-potential differences between the regions take part in mechanistic differences.

The experiments yield an average (electrokinetic) tortuosity. Tortuosity in the neurochemical context as determined through diffusion measurements is defined as $\lambda_D = \left(D / D_{\mathrm{obs}}\right)^{1/2}$ where D is the molecular diffusion coefficient in an unobstructed medium, D_{obs} is the observed diffusion coefficient, and the subscript D denotes diffusion. It is noteworthy that tortuosity influences fluid flow[22] and electrophoresis[150] through porous media. Boyack considers two contributions to tortuosity in electrophoresis: one is purely geometrical- the ratio of the actual distance that a molecule travels in its path around obstacles to get from point A to point B to the straight-line distance between A and B- whereas the other is related to the amplification of the electric field in narrow conduits. Similarly, tortuosity as measured by diffusion is related to a geometrical component and other factors, e.g., local viscosity.[106] Thus measurements made by diffusion and by electrokinetic experiments may not yield the same result.

In the development of the data treatment (Eq. 4), we assumed that the tortuosity (as determined by electrokinetic experiments) is independent of brain region and fluorophore size and charge. In fact, there is a dependence of tortuosity (as measured by diffusion) on molecular mass and type of polymer (in acute cortical slices).[98, 162, 163] Using a small probe molecule, TMA^+, differences in tortuosity (as measured by diffusion) in different regions of the hippocampus have been found.[110, 112, 164] In cortical slices, Nicholson found that the range of tortuosities for fluorescein conjugated dextrans in the same molecular mass range that we used (3-70 kDa) was from 1.77 to 2.25.[163] Thus, to the degree that the tortuosities measured electrokinetically and diffusionally are the same, our measured tortuosity has to be considered an average over the molecular masses and the brain regions studied.

If there is a correlation between the observed mobility and fluorescent species molecular mass, molecular mass effects on tortuosity may lead to a deterministic error in ζ. If there is no correlation, differences in tortuosity will add to the error in ζ, but will not affect its magnitude. From Fig. 3.4, it can be seen that there is no significant pattern of deviation from the line due to molecular mass. The correlation coefficient of the molecular mass and electrophoretic mobility (data in Table 3.1) is -0.07 demonstrating the lack of correlation. Thus, the assumption of an average tortuosity adds to the error in ζ, but does not influence the measured magnitude of ζ. Furthermore, recall that the two-fluorophore experiment yields a result that is independent of tortuosity (if it is again assumed that one tortuosity applies to both dyes). The average ζ-potential from these results, as mentioned above, is indistinguishable from the value determined from Eq. 4. Thus, although the assumptions about the tortuosity certainly must add to the uncertainty, they are apparently not influencing the result for ζ-potential.

3.4.3 Potential applications and implications

A plot of μ_{obs} vs μ_{ep} (e.g. Fig. 3.4) relates an easily measured quantity, μ_{ep}, to information about how fast a molecule moves in the brain. This is useful in the context of experimental procedures like iontophoresis. The μ_{obs} for a solute dictates whether it will move into or away from an iontophoresis capillary. A neutral molecule, for example, has a μ_{ep} of 0 m^2/Vs. By applying Eq. 8, the μ_{obs} is expected to be 5.2×10^{-10} m^2/Vs. Therefore, in the OHSC and with the proviso that the iontophoresis capillary ζ-potential matches the tissue ζ-potential, a neutral compound would move toward the cathode. To eject a neutral compound iontophoretically, it must be in the anodic chamber.

It is instructive to consider under what conditions EO flow contributes to the transport of a neutral molecule by comparing the magnitudes of EO velocity and diffusive velocity. This is done with the Peclet number, Pe. The Peclet number is the ratio of the time required to diffuse a characteristic distance a, ($\sim a^2/D$), to the time required to move with the fluid flowing at velocity v over the same distance, a (a/v).

$$Pe = \frac{va}{D} \tag{9}$$

For a neutral solute, the Smoluchowski equation (Eq. 3) for ζ with the Stokes-Einstein equation for D yields the following Peclet number.

$$Pe = \frac{6\pi r a \varepsilon \zeta E}{kT} \tag{10}$$

In Eq. 10, r is the radius of the presumed spherical solute, k is Boltzmann's constant, and T is temperature. If we assume that tortuosity influences diffusion and migration to the same degree, it does not appear in Pe. The field at which diffusive and electrokinetic velocities are equal, E_c, is thus

$$\mathrm{E_c} = \frac{\mathrm{kT}}{6\pi \mathrm{ra} \varepsilon \zeta} \tag{11}$$

Finally, equating E_c with a critical voltage difference over the characteristic length, $\Delta V_c/a$, the critical voltage is given as Eq. 12:

$$\mathrm{V_c} = \frac{\mathrm{kT}}{6\pi \mathrm{r} \varepsilon \zeta} \tag{12}$$

Note that the characteristic distance divides out. We can use a correlation[165] to relate molecular radius and molecular mass. For a 1 kDa (r = 0.84 nm) neutral molecule, the critical voltage is 19 mV (for the ζ-potential that we measured, -22 mV). For a 10 kDa neutral (r = 2.6 nm), the critical voltage is only 6 mV. Clearly, this magnitude of potential difference is plausible, leading to the conclusion that EO flow may in fact play a role in extracellular transport.

If EO flow does play a role, how would it influence charged neurotransmitters/ modulators? The direction of EO flow when ζ is negative is the same as the electrophoretic direction of a cation. Thus, an electric field would drive a cation more rapidly, and an anion less rapidly, in the presence of EO flow in comparison to the absence of EO flow. It is interesting to note that the influence of dopamine, a cation, is felt outside the synapse. Further, its local concentration and concentration dynamics are important in its actions.[33, 166] The presence of an electric field would cause dopamine to move relatively rapidly. In vertebrate brain, the anionic amino acid glutamate is responsible for fast neurotransmission. Unrestricted diffusion of glutamate over larger areas may cause synchronous activation of neurons and epilepsy. Thus this type of transmission has to be tightly localized to the individual synapse from which glutamate is released. The main system to regulate this process is reuptake. However, it is worth noting that any electric field that exists would have very little impact on glutamate's motion- its electrophoretic velocity and the extracellular fluid's EO velocity will counteract each other.

3.5 ACKNOWLEDGMENTS

The authors thank National Institutes of Health (R01 GM 44842) and the Swedish Research Council/Medicine for grants that supported this work.

3.6 SUPPORTING MATERIAL

3.6.1 Results

Several other small dyes were also potential candidates for this study, but were excluded for the following reasons: Quantum yield too low: neutral red, tris(2,2’-bipyridine)osmium(II), tris(4,7-bis(4-sulfophenyl)-1,10-phenanthroline) ruthenium(II), bis(2,2’-bipyridine)(4,7-bis(4-sulfo-phenyl)-1,10-phenanthroline) ruthenium(II), bis(2,2’-bipyridine)(4-carboxy-2,2'-bipyridine) ruthenium(II). Atypical capillary electropherogram: Fluoresceinamine, isomer 1. Interacts with tissue: Rhodamine 6G, Rhodamine B.

3.6.2 Discussion

3.6.2.1 Analysis of the method

Most omitted dyes simply have a low quantum yield under our conditions. Fluoresceinamine, isomer 1, on the other hand, has multiple peaks in the CE, indicating impurities. The rhodamine dyes appear to associate with the cell surface or components of the extracellular matrix. Their μ_{ep} values appear reasonable according to their sizes and charges, but rhodamine 6G does not move in tissue at all, while rhodamine B has a μ_{obs} of -4.28 ± 0.86 x 10^{-10} m^2/Vs. The latter μ_{obs} is smaller in the OHSC by a factor of 10 from what is expected from Eq. 8.

3.6.3 Materials and methods

3.6.3.1 Chemicals and solutions

Each of the following fluorescent dyes was diluted with HBSS, filtered, and frozen until use. Rhodamine 6G, Rhodamine B, Neutral Red, tris(2,2'-bipyridine)osmium, and Fluoresceinamine, isomer 1 were all obtained from Sigma. Three dyes, tris(4,7-bis(4-sulfophenyl)-1,10-phenanthroline)ruthenium,[167] bis(2,2'-bipyridine)(4,7-bis(4-sulfophenyl)-1,10-phenanthroline) ruthenium,[168] and bis(2,2'-bipyridine)(4-carboxy-2,2'-bipyridine)ruthenium,[169] were synthesized in the laboratory using materials obtained from Sigma and previously reported procedures.(1-3)

3.6.3.2 Capillary electrophoresis

CE analyses of rhodamine 6G and rhodamine B were performed in a 40 μm inner diameter (ID), 360 μm OD capillary (118.4 cm total length, 26.8 cm from injection to detection) using -22.1 kV. CE of fluoresceinamine, isomer 1 used a 50 μm ID, 360 μm OD capillary (70.9 cm total length, 48.1 cm from injection to detection) using -9.9 kV. These 3 dyes were detected at 495 nm. The remaining dyes listed above were not analyzed by CE.

Table 3.3. Dye concentrations

Dye	Concentration (mM)
1	2.00
2	3.06
3	0.60
4	2.00
5	1.00
6	1.00
7	1.00
8	0.30

Table 3.4. CE parameters

Fluorescent Compound	Capillary Inner Diameter (μm)	Total Length (cm)	Lenth to Window (cm)	Applied Potential (kV)	UV absorbance (nm)
AlexaFluor 568 10 kDa‡	50	50.3	31.5	-10.5	505
BODIPY FL 10 kDa‡	50	50.3	31.5	-9.0	505
Fluorescein 70 kDa‡	40	89.4	26.5	-22.0	505
Oregon Green 10 kDa‡	40	87.4	25.5	-22.0	505
Rhodamine Green 3 kDa‡	40	89.4	26.5	-22.0	505
Texas Red 70 kDa‡	40	89.4	26.5	-22.0	595
Fluorescein sodium salt	40	118.4	26.8	-22.1	495
tris(2,2’-bipyridine)ruthenium	40	118.4	26.8	-22.1	495
Rhodamine 6G	40	118.4	26.8	-22.1	495
Rhodamine B	40	118.4	26.8	-22.1	495
Fluoresceinamine, isomer 1	50	70.9	48.1	-9.9	495

‡Dextran Conjugate

4.0 DETERMINATION OF ζ-POTENTIAL AND TORTUOSITY IN RAT ORGANOTYPIC HIPPOCAMPAL CULTURES FROM ELECTROOSMOTIC VELOCITY MEASUREMENTS UNDER FEEDBACK CONTROL

Reproduced with permission from *Analytical Chemistry* **2009**, 81 (8), 3001-3007.

ABSTRACT

Extracellular translational motion in the brain is generally considered to be governed by diffusion and tortuosity. However, the brain as a whole has a significant ζ-potential, thus translational motion is also governed by electrokinetic effects under a naturally occurring or applied electric field. We have previously measured ζ-potential and tortuosity in intact brain tissue, however the method was tedious. In this work, we use a four-electrode potentiostat to control the potential difference between two microreference electrodes in the tissue, creating a constant electric field. Additionally, some alterations have been made simplify our previous procedure. The method entails simultaneously injecting two 70 kDa dextran conjugated fluorophores into rat organotypic hippocampal cultures and observing their mobility using fluorescence microscopy. We further present two methods of data analysis: regression and two-probe analysis. Statistical comparisons are made between the previous and current methods as well as between the two data analysis methods. In comparison to the previous method, the

current, simpler method with data analysis by regression gives statistically indistinguishable mean values of ζ-potential and tortuosity, with a similar variability for ζ-potential, -21.3 ± 2.8 mV, and a larger variability for the tortuosity, 1.98 ± 0.12. On the other hand, we find that the current method combined with the two-probe analysis produces accurate and more precise results, with a ζ-potential of -22.8 ± 0.8 mV and a tortuosity of 2.24 ± 0.10.

4.1 INTRODUCTION

Translational motion of molecules in the extracellular space of functioning tissues is typically viewed as being governed by diffusion and tortuosity.[18] Although not as well studied, electroosmotic effects occur in tissues due to natural processes[117] or experimentally applied fields.[15, 17, 21, 126-128, 170] Electroosmotic flow is the bulk fluid flow created by an electric field in a heterogeneous medium with a non-zero ζ-potential. In the brain for example, fixed charges on cell-surface functional groups and constituents of the extracellular matrix create a ζ-potential.[78] The electroosmotic velocity is governed by the magnitude of the ζ-potential.

In order to determine the electroosmotic velocity in brain tissue, it is necessary to know the ζ-potential. Some methods exist for determining the ζ-potentials of particulate objects (e.g., cells) and film-like objects (e.g., skin). ζ-potentials of particulate objects have been determined by electrophoretic techniques.[139-145] Electroosmotic flow in thin samples, such as plant tissue can be determined by flux through the tissue.[146] Electroosmotic flow is described and quantitated as an influential parameter in transdermal iontophoresis[30, 131-136] and transdermal sampling (reverse iontophoresis[136, 138]). Transport through individual skin pores can be observed by applying an oscillating electric potential[147] or by scanning electrochemical microscopy.[30] The experimental arrangement for determining the electroosmotic velocity through pores, such as in skin or leaf epidermis, is simplified by the geometry of these biological film-like samples. A potential difference can be generated across the film-like sample. Electrokinetic phenomena then occurs perpendicular to the film-like sample, carrying fluid from one side of the film-like sample to the other.[146] Quantifying ζ-potential and electroosmotic flow in a heterogeneous tissue matrix, on the other hand, is technically challenging.

We have previously published a method of determining ζ-potential and tortuosity in intact organotypic hippocampal slice cultures (OHSCs) using fluorescent probes.[78] The hippocampus is of great interest because it is the center of spatial learning and memory. Conditions such as Alzheimer's disease and ischemia that occur in this region are particularly devastating. The experimental method places an OHSC on the stage of a fluorescence microscope. The velocities of several fluorescent probes in the tissue experiencing an applied electric field are measured. Relating the measured velocities, which are the sums of the electrophoretic and electroosmotic velocities, to the probes' electrophoretic mobilities in free solution leads to a determination of ζ-potential and tortuosity. While successful, the method is not without drawbacks. The focus of this work is to simplify and reduce the effort required to make these measurements while decreasing or at least not increasing the variability in the previous method.

Potential drawbacks in the previous method include: 1) using agarose gel containing a HEPES buffered salt solution (HBSS) as a contact between the electrodes and brain tissue. The contact between the gel and tissue is difficult to reproduce; 2) measuring, not controlling, the electric field. While the field is apparently constant (measured zone velocity independent of time), it would be better to control the field; 3) using eight probes. Using eight probes was helpful to establish experimentally the predicted linearity in a plot of observed vs. electrophoretic mobilities. Now that the linearity is proven, there is no need to repeat the process. Consequently, it may be possible to use fewer fluorescent probes; 4) using probes of various molecular weights. Using probes of similar composition and molecular weight is preferred because tortuosity is dependent on probe composition and molecular weight.[109, 171, 172] In this work, the measured ζ-potential and tortuosity are compared to our previous work to assess accuracy and precision. Furthermore, we compare two data analysis approaches to obtain ζ-potential and tortuosity from measurements using only two probes.

4.2 THEORY

We have previously published the general theory for determining ζ-potential and tortuosity.[78] The experimental design relies on fluorescent probes with a range of electrophoretic mobilities. In the work presented here, solutions of fluorescent probes are injected simultaneously in pairs into an OHSC on the stage of an inverted microscope. Under the influence of an electric field applied perpendicular to the optical axis, each fluorescent probe will move by electroosmosis, electrophoresis, or both at an observed velocity, $\mathrm{v}_{\mathrm{obs}}$, which is the product of the mobility, μ, and the electric field, E. The electroosmotic mobility is called μ_{eo}. Equation 1 defines the relationship between μ_{eo} and ζ-potential, ζ.[22, 151]

$$\mathrm{v}_{\mathrm{eo}} = -\frac{\varepsilon\zeta}{\eta}E = \mu_{\mathrm{eo}}E \qquad (1)$$

Equation 1 shows that μ_{eo} is a function of ζ, the viscosity of the medium, η, and the permittivity, ε. The same relationship (with a change in sign) exists for electrophoretic velocity, v_{ep}, and mobility, μ_{ep}. Thus, an observed mobility, μ_{obs}, is defined by equation 2 for an individual molecule, where λ is the tortuosity[78].

$$\mu_{obs} = \frac{v_{obs}}{E} = \left(1/\lambda^2\right)\left(\mu_{ep} + \mu_{eo}\right) = \left(1/\lambda^2\right)\left(\mu_{ep} - \frac{\varepsilon\zeta}{\eta}\right) \tag{2}$$

One method of analysis, implemented in our prior work, uses linear regression to determine the parameters of interest. A linear regression of μ_{obs} on μ_{ep} yields ζ and λ from the intercept and slope using values of ε and η for water. Another method, which we will call the 'two-probe' method, takes advantage of the fact that we use a solution containing two electrophoretically and spectroscopically different fluorescent probes (1 and 2). Each probe moves independently at an observed mobility. The two probes' observed mobilities, measured simultaneously in one experimental run, are used to calculate a single value of ζ and a single value of λ. Values of ζ and λ are determined as shown in equations 3 and 4. Here, the numerical subscripts refer to the two probes.

$$\zeta = \mu_{obs1}\frac{\left(\mu_{ep1} - \mu_{ep2}\right)}{\left(\mu_{obs1} - \mu_{obs2}\right)} - \mu_{ep1} \Big/ \left(-\varepsilon/\eta\right) \tag{3}$$

$$\lambda_e = \sqrt{\frac{\mu_{ep1} - \mu_{ep2}}{\mu_{obs1} - \mu_{obs2}}} \tag{4}$$

Reported values for ζ and λ are obtained by averaging the results of the individual, two-probe experiments.

4.3 EXPERIMENTAL SECTION

4.3.1 Chemicals and solutions

The culture medium was comprised of Basal medium Eagle (50%), Earl's basal salt solution (20%), horse serum (23%), penicillin/streptomycin (25 units/ml), L-glutamine (1 mM), and D-(+)-glucose (7.5 g/L). All components were acquired from Sigma (St. Louis, MO) and used as received. The culture medium was warmed to 37 °C before use, but otherwise was kept in a refrigerator. D-(+)-glucose (27.5 mM) and $MgSO_4$ (2.7 mM) were added to Gey's Balanced Salt solution (GBSS), all also purchased from Sigma, as were the following: HEPES-buffered salt solution (HBSS) containing (mM): 143.4 NaCl, 5 HEPES, 5.4 KCl, 1.2 $MgSO_4$, 1.2 NaH_2PO_4, 2.0 $CaCl_2$, and 10 D-(+)-glucose. HBSS was prepared with 18 MΩ purified water from a Millipore Synthesis A10 system (Millipore, Billerica, MA), filtered and refrigerated at 2.6 °C. It was warmed to 37 °C before use.

Fluorescent probes, Texas Red dextran conjugate 70 kDa (**TR7**) and Fluorescein dextran conjugate 70 kDa (**Fl7**) were purchased from Invitrogen/Molecular Probes (Eugene, OR). **TR7** and **Fl7** were dissolved in HBSS to make 0.34 mM and 0.67 mM solutions, respectively, then filtered with 13 mm, 0.45 μm PTFE Millex filter units or equivalents (Millipore) and frozen until use. The final solution containing both fluorophores had a concentration of 0.19 mM for **TR7** and 0.29 mM for **Fl7**.

4.3.2 Organotypic hippocampal slice cultures

OHSCs were prepared according to the Stoppini culturing technique with small variations.[84] The procedures below were authorized by the University of Pittsburgh IACUC. Seven-day postnatal Sprague-Dawley albino rats were decapitated and the hippocampi dissected bilaterally. The hippocampi were cut perpendicular to the septo-temporal axis using a McIlwain tissue chopper (The Mickle Laboratory Engineering, Surrey, England) into 500 μm thick slices. The OHSCs were placed on Millicell membrane inserts (Millipore CM), pore size 0.4 μm, over culture medium and incubated in 95% air/5% CO_2 at 37 °C. The cultures are roughly ellipsoidal, with the major axis approximately running from the CA3 to the subiculum.

All OHSCs used for the data reported here were cultured for 3 to 10 days, when the tissue thickness is ~150 μm.[84] Prior to an experiment, the culture medium was replaced with 37 °C GBSS and incubated for 30 minutes. This exchange and incubation was repeated two more times, where the final exchange was with 37 °C HBSS. The following manipulations took place at room temperature. The insert membrane was cut using an X-Acto knife to separate the OHSC and the membrane directly beneath it from the insert, as shown in Figure 4.1. To facilitate handling of the tissue, a millimeter or two of membrane was left extending along the major axis, and the combined membrane/culture was placed in the apparatus with the major axis parallel to the applied field.

4.3.3 Four-electrode potentiostat

We have converted a three-electrode potentiostat (Princeton Applied Research Model 173, Princeton, NJ) to a four electrode potentiostat using a differential amplifier in order to convert the two measured reference electrode potentials into a single difference potential.[173] This potentiostat is capable of applying up to 100 V between the two ‘counter’ electrodes in our apparatus (described below). To accommodate a high common mode voltage, a high voltage operational amplifier, AD445 (shown as U1 and U2 in Supporting Information Figure S-4.1) from Analogue Devices (Norwood, MA), with a power supply range of +/- 50 volts was used. The amplifier has a typical input bias current of +/- 1.4 pA and a typical input offset current of +/- 0.2 pA. These amplifiers were connected as buffer amplifiers and were the inputs to an AD629 differential amplifier (U3), also from Analog Devices. The amplifier that consists of U1, U2, and U3 allows a common mode range of +/- 42.5 V. Two reference electrodes were connected to the input ends of the amplifier. The reference electrode closest to the cathode was connected to the negative input end of the U3 differential amplifier by way of the buffer amplifier U1 (AD445). Another AD445, U2, was the buffer amplifier connected to the positive input end of U3 and to the other reference electrode. Buffer amplifiers U1 and U2 were connected to a +/- 45 V HP 6205C Dual DC Power (currently Agilent, Santa Clara, CA). A homemade +/- 15 V DC power supply supplied power to U3. Capacitors were used in the power supplies to remove noise, as shown on the bottom of Figure S-4.1. The output end of U3 was connected to the reference electrode input of the potentiostat. Platinum electrodes in each reservoir of the cell (described below) were the two counter electrodes. They were connected to the auxiliary and working inputs of the potentiostat. This configuration created a feedback loop such that the potential difference between the sensing regions of the two reference electrodes was constant.

4.3.4 Apparatus for tissue experiments

Illustrated schematically in Figure 4.1, the cell was manufactured locally using Lucite. The cell was comprised of a narrow, 44 mm long, rectangular channel separating two cylindrical reservoirs (19 mm in diameter and 12 mm deep). Each of the reservoirs contained a tubular platinum electrode (1 mm OD, 0.1 mm wall thickness, and ~3.8 cm long) obtained from Goodfellow (Cambridge, England). The OHSC, already removed from the excess insert membrane as described in a previous section, was placed in the middle of the channel. Electrical contact between the OHSC and the platinum electrodes was made by filter paper, Grade 1 Whatman (Maidstone, England), soaked with HBSS. A piece of filter paper, with one side in the HBSS reservoir, was laid just over one end of the tissue. The same was done with another strip of filter paper from the other reservoir to the other end of the OHSC, as shown schematically in Figure 4.1. Two 100 μm (ID) fused-silica capillaries, separated by a fixed distance of 2.5 mm, were used as Luggin capillaries. They were each pulled to a tip of ~20 μm (OD) using a P-2000 capillary puller from Sutter (Novato, CA) and inserted into the ends of the OHSC facing each of the platinum electrodes. HBSS filled the Luggin capillaries and their associated vials. The vials each contained a Bioanalytical Systems Ag/AgCl reference electrode (3 M NaCl, West Lafayette, IN). These reference electrodes were connected to the input ends of the differential amplifier as described previously.

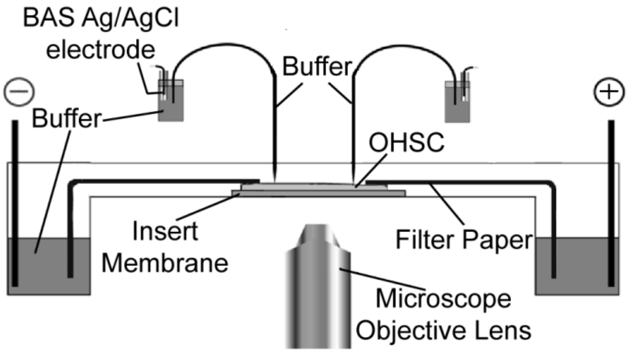

Figure 4.1. The apparatus

The apparatus sits on an inverted fluorescence microscope for image analysis. Reservoirs on either side of the apparatus each contain a platinum counter electrode (labeled '-' and '+') and is half filled with HBSS. A HBSS-saturated piece of filter paper spans from inside each reservoir to either end of the OHSC, which sits on a piece of membrane in the center of a channel. Pulled Luggin capillaries are inserted into the OHSC 2.5 mm apart. The distal ends of the capillaries are in vials containing Ag/AgCl electrodes filled with HBSS.

4.3.5 Injection capillary

Using the same capillary puller, a 250 μm (ID) fused-silica capillary was pulled to a tip of ~12 μm (OD). The capillary was lowered perpendicularly into the OHSC with a Sutter (Novato, CA) MP-285 micromanipulator. The distal end of the injection capillary connected to a FemtoJet® express from Eppendorf (Hamburg, Germany), which was pressurized by a compressed nitrogen tank from Valley Natural Gas (Wheeling, WV). The FemtoJet® express was set to deliver an injection pressure of 200 to 300 hPa for 0.2 seconds, with a compensation pressure of 40 to 70 hPa.

4.3.6 Imaging

Imaging of the experiment was done with an inverted IX71 fluorescent microscope with a UPlan Apo 4× objective lens, both Olympus products (Melville, NY), and a charge-coupled device camera (ORCA-285 Hamamatsu, Hamamatsu City, Japan). A DA/Fl/TA-3X-A Triple-band "Pinkel" filter set from Semrock (Rochester, NY), with exciter 1 387 nm, exciter 2 494 nm, exciter 3 575 nm, triple-band dichroic mirror: 394–414 nm, 484–504 nm, 566–586 nm, emitter: 457, 530, 628 nm was used according to the fluorescent properties of the probes. SimplePCI 6.0 software from Compix (Cranberry, PA) was used for image acquisition and processing.

4.3.7 ζ-potential determination

Prior to the start of the ζ-potential measurements, an OHSC is injected with each fluorophore solution separately to set each exposure time using the autoexposure command for a two-color image on SimplePCI 6.0. In preparation for each measurement, a fresh OHSC was prepared and placed in the measuring cell on the stage of the microscope. The tip of the injection capillary was loaded with a solution containing both fluorophores at room temperature. It was lowered perpendicularly ~75 μm (approximately midway) into the new OHSC using the micromanipulator. We estimate that the FemtoJet® express delivered about 60 pL of the solution most of the time. Occasionally, mere placement of the capillary in the tissue delivered a larger quantity of the fluorophore solution through capillary effects. Once the injection was complete, the injection capillary was raised from the OHSC and the Luggin capillaries were lowered into the tissue. The time lag from the injection to the application of the electric field is long enough that convective flow from the injection does not interfere with the electroosmotic flow during the measurement.

An electric field between 320 V/m and 2000 V/m was chosen arbitrarily for each run. This range of values was limited on the low end by the need to measure accurately the motion of the fluorescent zones, and on the high end to avoid electroporation.[159] The potentiostat's applied voltage was determined based on the chosen field and the 2.5 mm reference electrode spacing. Following application of the potential, one image was acquired every one, five, ten, or twenty seconds. The electric field was measured at the two Luggin capillaries by a multimeter to ensure that the system was controlling the field accurately. The same was done for the two platinum electrodes in the reservoirs.

Figure 4.2 shows still images taken at two times during an experiment. The Supporting Information includes unenhanced and enhanced movies showing the fluorophore movement. Positive movement of a fluorophore was defined as movement toward the cathode. Using the imaging software, we determined the velocities of the fluorescent zones as follows. The positions of the zones prior to the application of the field (t=0) are defined by the location of the maximum in fluorescence intensity. We then observed the movement of the zones under the influence of the field (using a software-generated video) to determine the point at which a well-defined zone was discernable from the initial zone, as a considerable amount of fluorescence typically remains at or near the position at t=0. The location at a particular time of the intensity maximum of the moving zone defined the zone velocity (N.B. – a multiple-point approach demonstrating constant velocity was used for 203 measurements in the previous publication[78]). The distance that the zones moved in and experiment varied from about 50 to several hundred μm.

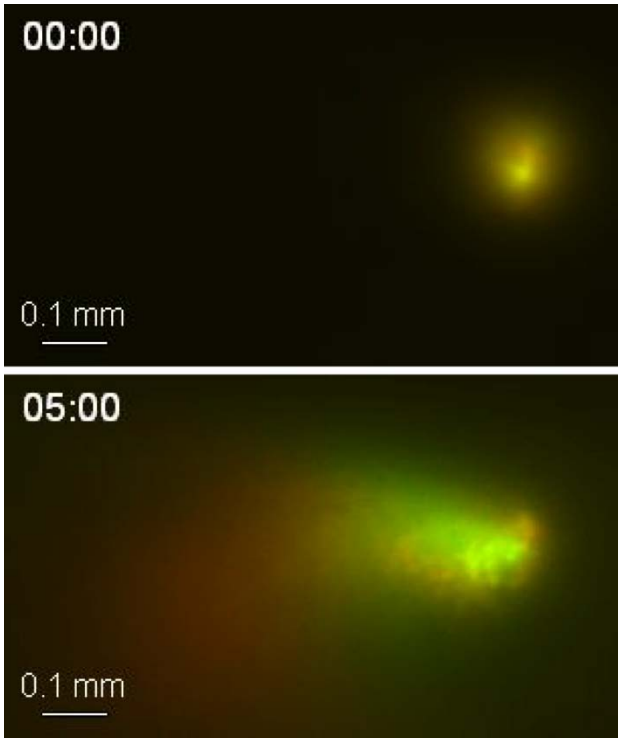

Figure 4.2. Sample experimental run

The two images show both fluorophores injected into the CA1 of the OHSC. TR7 is red, and Fl7 is green. The top image is taken at time 0. The bottom image shows, at a time of 5 minutes, that the probes have moved towards the cathode. The bottom image's contrast has been increased to increase the visibility of the fluorophores.

4.4 RESULTS

We measured fifty pairs of electroosmotic mobilities (one for each fluorescent probe) in OHSCs. One pair's derived values of ζ-potential and tortuosity (based on equations 3 and 4) were obviously outliers (ζ = -132 mV and λ = 8.4). This pair was not included in the following analysis. We will first compare results (previous vs. current) for the directly observed quantity, μ_{obs}. We then compare results (previous vs. current) for the derived parameters, ζ-potential and tortuosity. Finally, we compare the two data treatments, regression vs. two-probe, using the ‘current’ data.

Table 4.1a compares the observed mobilities for each fluorescent probe from the previous experimental method to those of the current method using a Student’s t-test. The number of runs is n; t is the Student’s t value; and p is the probability that the observed difference (t value) is due to chance alone, also known as the p-value. Table 1b shows the analogous variances, s^2, the degrees of freedom, abbreviated as df, as well as the F statistic, F_s, and its p-value, p. It is worth restating that there are several differences between the previous method and the current method. The statistical testing will determine whether the current, much simpler, method gives acceptably equivalent results (t-test) with no poorer precision (F-test) than the previous method. The t-test in Table 4.1a shows that for both **Fl7** and **TR7** the null hypothesis, that the two mobilities are the same, should be accepted. Additionally, the change in the method modestly improves the precision in both observed mobilities as shown by Table 4.1b with p-values of 0.07 for both fluorophores. Thus, the observed mobilities are equivalent to, and perhaps more precisely determined, by the simpler current method than the previous method. An increase in precision is helpful because it reduces the number of experiments required to establish a value of the ζ-potential with a given confidence interval.

Table 4.1a. Comparison of observed mobilities

	Previous Method			Current Method				
	μ_{obs}†	SEM†	N	μ_{obs}†	SEM†	n	t	p
Fl7	1.85	0.24	22	1.76	0.13	49	0.40	0.69
TR7	3.66	0.71	12	4.12	0.26	49	0.88	0.38

Table 4.1b. Comparison of variances

	Previous Method		Current Method			
	s^{2} ‡	df	s^{2} ‡	df	F_s	P
Fl7	1.32	21	0.78	48	1.69	0.07
TR7	6.10	11	3.24	48	1.88	0.07

†Units: 10^{-9} m^2/Vs
‡Units: 10^{-18} m^4/V^2s^2

A linear regression of μ_{obs} vs. μ_{ep} from the current method (n=98) yields a slope of 0.26 ± 0.03 and a y-intercept of $4.3 \pm 0.2 \times 10^{-9}$ m^2/Vs. The stated errors are the SEMs. The slope is equal to the inverse square of the average tortuosity. Therefore, the average tortuosity is 1.98 ± 0.12 (see Table 4.2a). Inserting the intercept into equation 2 yields an average ζ-potential of -21.3 ± 2.8 mV. Table 4.2a shows two-tailed t-test comparisons of ζ-potential and tortuosity determined with the current method vs. the values from the previous method.[78] With probabilities of 0.84 for ζ-potential and 0.26 for tortuosity, we infer statistically indistinguishable values. F-test comparisons, as shown in Table 4.2b (p-values of 0.60 for ζ-potential and 5.2×10^{-5} for tortuosity), show the variability in ζ-potential is indistinguishable from the previous method's. However, this table shows we have increased the variance in the tortuosity determined by the current method using linear regression for data analysis in comparison to the previous method (which also used linear regression).

Table 4.2a. Comparison of ζ-potential and tortuosity of the two experimental methods

	Previous Method			Current Method				
	Mean*	SEM*	N	Mean*	SEM*	n	t	p
ζ	-22	2	203	-21.3	2.8	98	0.20	0.84
λ	1.83	0.06	203	1.98	0.12	98	1.1	0.26

Table 4.2b. Comparison of variances

	Previous Method		Current Method			
	$s^{2\,\S}$	df	$s^{2\,\S}$	df	F_s	p
ζ	812	201	773.82	96	0.95	0.60
λ	0.73	201	1.42	96	1.93	5. 2 × 10^{-5}

*Units: for ζ, mV; for λ, unitless
§Units: for ζ, mV^2; for λ, unitless

We now turn to a comparison of data analysis methods. This comparison is based only on data from the current method. In the regression analysis, all 98 data are used to find ζ-potential and tortuosity. In the two-probe analysis, 49 values of ζ-potential and tortuosity are averaged. Table 4.3a displays the results of the two analysis methods, namely linear regression and the two-probe method. The two analysis methods yield statistically indistinguishable values for both ζ-potential and tortuosity, as shown by their p-values of 0.60 and 0.24, respectively. However, the F-tests in Table 4.3b show that the precision greatly improves with the use of the two-probe analysis.

Table 4.3a. Comparison of ζ-potential and tortuosity of the two analysis methods

	Regression Analysis			2-Probe Analysis				
	Mean*	SEM*	N	Mean*	SEM*	n	t	p
ζ	-21.3	2.8	98	-22.8	0.8	49	0.52	0.60
λ	1.98	0.12	98	2.24	0.10	49	1.18	0.24

Table 4.3b. Comparison of variances

	Regression Analysis		2-Probe Analysis			
	$s^{2\,\S}$	df	$s^{2\,\S}$	df	F_s	p
ζ	773.82	96	29.48	48	26.2	< 0.0001
λ	1.42	96	0.52	48	2.74	0.0001

*Units: for ζ, mV; for λ, unitless
[§]Units: for ζ, mV^2; for λ, unitless

4.5 DISCUSSION

4.5.1 Comparison of methods

We made several alterations to the original experimental setup and procedure to simplify and improve the method of determining ζ-potential and tortuosity in intact OHSCs. One such alteration is the use of HBSS in conjunction with filter paper instead of agarose gel slabs. This eliminates the variability in the contact between the tissue and the agarose and eliminates the potential for variability among agarose compositions. Furthermore, the fluid flows more easily within the filter paper than in the agarose gel. This lower resistance to flow minimizes possible pressure differences. Originally, Ag/AgCl electrodes were inserted into the tissue cultures in the experimental region to measure the electric field during the experiment.[78] These electrodes, although small, were invasive and cumbersome. By replacing them with Luggin capillaries, pulled to a tip, the experimental manipulations become easier. The pulled tips of the Luggin capillaries are smaller (~20 μm OD) than the diameters of the Ag/AgCl electrodes (~100 μm each). Also, the capillaries allow the use of larger, more stable, commercially available (BAS) Ag/AgCl electrodes placed in remote vials. By using larger electrodes, amplifiers demanding larger currents are useable, thus simplifying potentiostat design and decreasing drift due to changes in the reference electrode potential occasioned by the operational amplifier current requirement. Most importantly, these electrodes no longer measure the electric field throughout the experiment, but participate in controlling the field between the capillaries with the use of a four-electrode potentiostat. Controlling the field in this manner reduces the variability in the field throughout the experiment. Lastly, the capillaries are now spaced further apart within the tissue culture, so as not to interfere with the fluorophore migration.

The four-electrode potentiostat replaces the use of a voltage supply and reference electrodes for measurement. A three-electrode potentiostat controls the potential between a working electrode and a reference electrode by applying current through an auxiliary electrode. Coupling a differential amplifier to the reference electrode permits the use of two reference electrodes[173] allowing for the control of a potential difference without the requirement that one of the electrode potentials is zero (ground). In this configuration, the potentiostat controls the potential between the two reference electrodes in a feedback loop. Each reference electrode's sensing point is defined by a Luggin capillary. The Luggin tips are small and do not interfere with the experiment. They are inserted along the major axis of the tissue such that the electric field within the tissue is maintained by current between the counter electrodes. The potentiostat maintains the potential difference between the counter electrodes in a range of 14 to 46 V (depending on the tissue and the field that we are trying to achieve). Therefore, the potential at the reference electrodes can be considerably larger than about 15 V vs. ground. This necessitated the use of amplifiers that can manage a high common mode voltage.

The hippocampus is a highly structured region. There are three areas that contain neuronal cell bodies, and thus show up clearly in images of sections of the hippocampal region, namely, the CA1, CA3, and the dentate gyrus. From the previous work, we know that there are small differences in ζ-potential and tortuosity among these three regions.[78] Of the 98 measurements in the data set for the current experiments, 26 are in the CA1, 36 are in the CA3, and 36 are in the dentate gyrus. A single-factor (regions) analysis of ζ-potential shows a p-value of 0.1 indicating borderline statistically insignificant differences among the regions. In this paper, we have chosen to ignore those (small) differences, thus including observations from the all the regions in a single data set. As Table 3.1 shows, the current method yields equivalent results for the experimentally observed quantity (in comparison to the previous method) and it is possibly more precise ($p = 0.07$).

Since the linearity of the relationship between μ_{obs} and μ_{ep} is established for OHSCs,[78] it is simpler to use only two probes for the regression analysis rather than eight probes. The potential disadvantage of the two particular probes used here is their relatively similar electrophoretic mobilities. The electrophoretic mobility range in the previous method is almost six times larger than the range in the current method. The range of the experimentally observed mobilities is similarly reduced by about a factor of six. The smaller range in the current method creates a greater sensitivity to additive random errors in the observed mobility than in the previous method. We are thus concerned about suffering an increase in variability of the ζ-potential and tortuosity because of the lower mobility range. Although two-tailed t-tests of both ζ-potential and tortuosity show that the current method (using only two probes) yields statistically indistinguishable results from the previous method (see Table 4.2a), the F-test in Table 4.2b test reveals that the alterations increase the variability of tortuosity. The variability in ζ-potential, however, does not increase. The result that there is no observable change in the error of the ζ-potential is favorable, but the increased variance in the tortuosity is disappointing. Fortunately, the two-probe method of analysis leads to improved precision as discussed next.

According to the two-tailed t-tests in Table 4.3a, the two-probe analysis is a viable analysis method. The significantly better precision of the two-probe analysis method is a result of reduced variability probably due to differences in tissue cultures. The two-probe procedure measures two observed mobilities in the same conditions, since they are injected simultaneously into the same location on the same tissue culture. The hippocampal formation is a highly structured entity in which there are variations in composition (cell bodies vs. projections) over small (~100 μm) distances. While we attempt to inject the probes into the cell-body-containing parts of the tissue, there is certainly a good chance for variability in this aspect of the measurement. Thus, it is not entirely unexpected to find that the variability in the measurement is reduced with the two-probe approach for data analysis.

4.5.2 Accuracy of the method

As Figure 4.2 and the video clips in the Supporting Information show, the fluorescent probes not only move linearly in the direction of the electric field, but also the initially well-defined zone disperses as it passes through the tissue. It has been shown by computations relating to capillary electrochromatography that in a packed bed, even with a constant ζ-potential, there is a distribution of velocities because of the locally varying electric field.[174] Over the several minute experimental time, the root mean square diffusion distance based on known diffusion coefficients[106, 171] and tortuosity is approximately 40 – 60 μm. As the observed dispersion is greater than this value, it is unlikely that diffusion plays an important role in the observed processes, at least in the two dimensions defined implicitly in Figure 4.2. On the other hand, we have observed earlier that the fluorescent probes can reside in the insert membrane below the cultured tissue.[78] This population of probe molecules in the membrane moves very slowly in the electric field. Consequently, the injection site is always visible, as is a tail of fluorophore behind the zone moving in the tissue. The tail arises, we think, from probe diffusing out of the membrane into the tissue and vice-versa.

The only extant value of ζ-potential is the value from the previous method. To the degree that the previous method is accurate, the current method is accurate. Tortuosity has been more widely investigated. The two dextran-conjugated fluorophores, **Fl7** and **TR7**, were chosen and paired because they have the same molecular weight, 70 kDa. Previous research has shown correlations between probe molecular weight, or more properly, hydrodynamic radius, and tortuosity.[78, 109-111] Using probes with the same molecular weight decreases error in tortuosity resulting from variations in probe radii.[171] As far as we are aware, there are no measurements of tortuosity in OHSC other that the value from the previous method. However, there are values for 70 kDa fluorescent dextran in the cortex of rat. The value of the tortuosity in acute rat cortical slices is 2.25[171]. The value in cortex *in vivo* is 2.68[109]. Values of tortuosity for 3 kDa fluorescent dextran in acute hippocampal slices are lower than comparable values in cortex and neocortex.[18] While there are not enough data for a firm conclusion, it appears that measurements of tortuosity by this method are accurate.

Such measurements could be extendable to *in vivo* conditions. However, several challenges arise in an *in vivo* experiment. The most significant is imaging of a fluorophore that is no longer in an optically thin sample. ’Seeing’ the region of interest is essential. Consequently, many *in vivo* diffusion measurements are in the easily accessible cortex.[18] Multiphoton experiments,[175] with currently available fluorescent probes, or the use of near IR probes[176] may be helpful. Injections of the fluorophore remain in the tissue following the conclusion of the experiment. Therefore, the fluorophore must be non-toxic to the animal. In addition, electrodes must be placed appropriately for electroosmotic flow to occur. This would be especially challenging for measurements in the interior of the brain. Current neurosurgical methods use transparent conduits,[177] for example, for endoscopic visualization and manipulation with corresponding instruments to access inner brain regions. Similar arrangements can be imagined for an *in vivo* ζ-potential and tortuosity determination. By slightly changing the approach to using contrast agents instead of fluorescent dextran conjugates, magnetic resonance imaging (MRI) and computed tomography (CT) scans can visualize probe movement without a full craniotomy. Electrodes and the injection capillary would still need to be inserted, but this can be minimally invasive.

In conclusion, the new experimental method reduces the variability of the experimentally measured mobilities. Moreover, the two-probe analysis method is accurate and more precise in determining ζ-potential and tortuosity, while also being simpler than the previous method.

ACKNOWLEDGMENT

The authors gratefully acknowledge funding from the National Institutes of Health (R01 GM 44842) and the Swedish Research Council/Medicine.

4.6 SUPPORTING INFORMATION

ABSTRACT

The supporting information section contains Figure S-4.1, the circuit diagram of the differential amplifier in the four-electrode potentiostat, and two video clips. Video S.2 is a contrast enhanced version of Video S.1. Both movies show three injections: in the CA1, CA3, and dentate gyrus regions. An electric field of 1.4 V/mm is applied across the tissue. Images are acquired every 20 seconds. During the course of 5 minutes, as shown by the time stamp in the upper left corner, **TR7** (in red) and **Fl7** (in green) move according to their observed mobilities. **TR7** separates from **Fl7** as it moves towards the cathode at a greater velocity than **Fl7.**

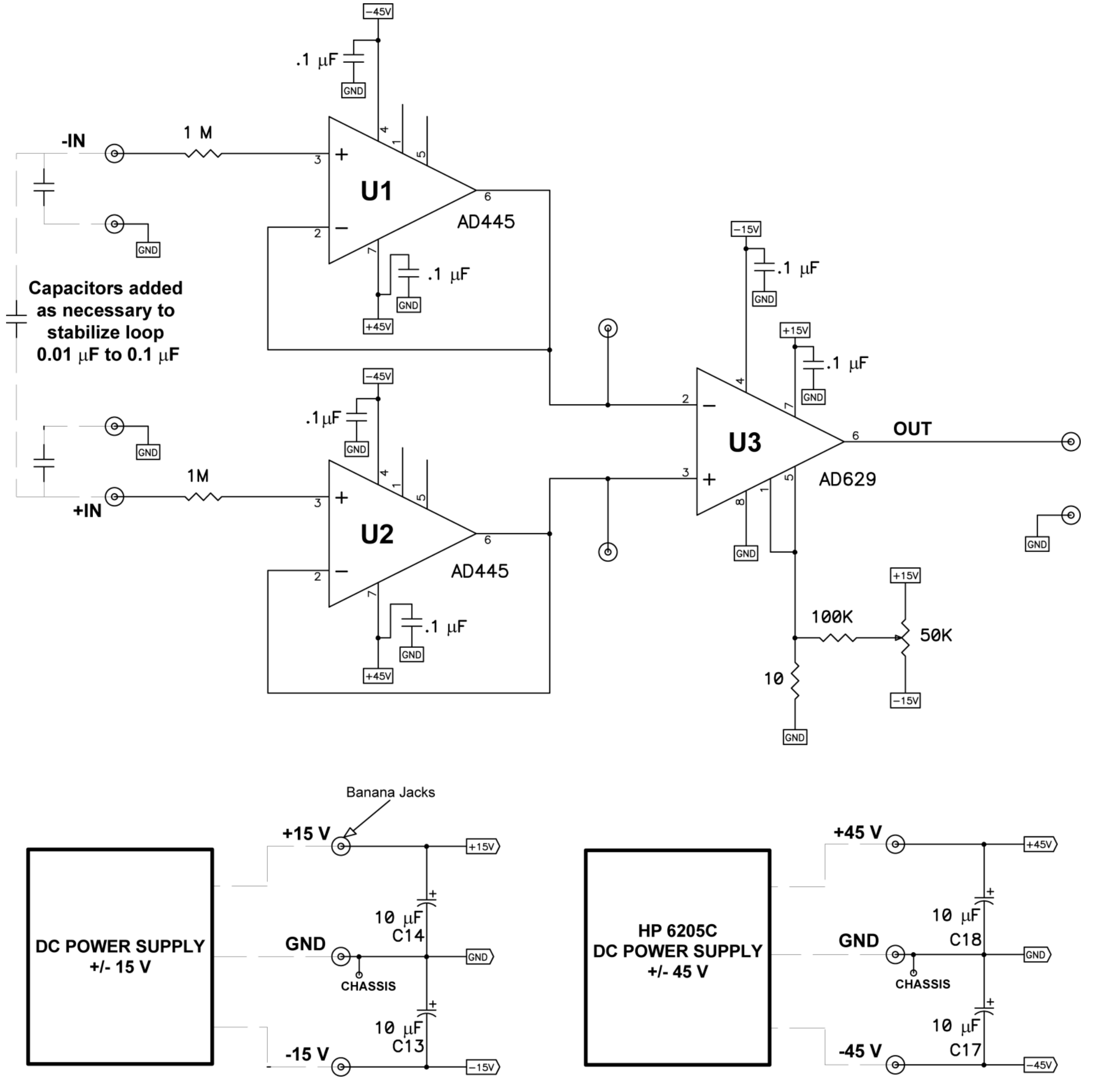

Figure S- 4.1. Circuit diagram of the differential amplifier in the four-electrode potentiostat

5.0 IONTOPHORESIS INTO A POROUS MEDIUM DEPENDS ON THE ZETA POTENTIAL OF THE MEDIUM

ABSTRACT

Iontophoresis uses electrically facilitated transport to deliver solutes into living tissue. Often, iontophoretic ejections into brain tissue are confined to millisecond pulses for highly localized delivery. This paper investigates solute penetration using extended iontophoretic ejections into brain tissue. Furthermore, the effect of the ζ-potential on ejections is examined using poly(acrylamide-co-acrylic acid) hydrogels with various magnitudes of ζ-potentials, including that similar to hippocampal brain tissue. Parameters that effect solute penetration distance include the magnitude of the applied current, solute properties, and the ζ-potential of the matrix. A theoretical calculation is presented as a quantitative method of predicting solute ejection profiles using the measured properties of the system. The theory eliminates the need for calibration of each iontophoretic experiment. Experiments also show that with an appreciable matrix ζ-potential, such as that of brain tissue, solute transport may be directed to specific locations following the direction of current flow.

5.1 INTRODUCTION

Iontophoresis is a popular method of solute delivery that uses the application of an electric field via constant current to deliver solutes to tissue. Electrokinetic processes motivate solutes to be transported into tissue. In addition to delivering solutes directly from a pipette into the brain, Lerner *et al*. use iontophoresis to deliver compounds to the brain through the nasal mucosa.[21] Brain iontophoresis is also used to stimulate neuronal pathways[128] and understand the brain's physicochemical properties and transport mechanisms.[128] Outside of brain delivery, iontophoresis is used to deliver solutes transdermally, transocularly,[178, 179] and transurethrally.[180]

Iontophoresis into the brain has the advantage of localized delivery that circumvents the blood-brain barrier. The main drawback to iontophoresis is its unpredictability. Historically, the transport number was used to correlate the number of moles of ejected ionic solute with the applied current.[181, 182] The correlation between the transport number and the ejected solute concentration is inadequate.[170] In practice, there is significant variability from one iontophoretic ejection pipette to another. Previous attempts to quantify iontophoretic ejections have had limited success.[183-185] Researchers have used ion-selective microelectrodes,[18, 186-188] carbon fiber microelectrodes,[189-191] and fluorescence microscopy[192] to measure solute ejection outside of the ejection pipette. Today, each ejection pipette must be pre-conditioned and calibrated in order to obtain a predictable distribution profile outside of the pipette tip.[170, 191, 193]

Trubatch and Van Harreveld proposed that electrokinetic processes within the tissue may account for some of the lack of agreement between predicted and experimental ejection profiles.[194] The theory was quickly refuted by Norman and others, stating that pulsed iontophoretic currents are low (≤100 nA) and ejections are too short to create appreciable electrokinetic contributions within the tissue.[193, 195-197] Until recently, the standard view was that iontophoresis into the brain can only convey charged solutes into tissue via charge migration in the iontophoretic pipette and diffusion thereafter into the tissue.[120, 193, 195-198]

Recently, Herr *et al.* demonstrated the significance of electrokinetic flow in the pipette during iontophoretic ejections into buffer solution using electrochemical detection adjacent to the pipette tip.[198] Applying an electric field within the pipette creates an electrokinetic bulk fluid flow known as electroosmotic flow, EOF.[22] EOF arises as a result of an electric field's motivating force on the mobile counterions to the fixed charges on the pipette walls. A solute in an electric field moves according to its electrophoretic velocity and the fluid's electroosmotic velocity in addition to diffusion. Therefore, Herr *et al.* were able to demonstrate ejections of neutral solutes as a result of the EOF in the pipette.[191, 198] The magnitude of EOF is proportional to the ζ-potential. The ζ-potential is the potential at the shear plane between the moving electrolyte solution and the immobile counterions along the surface. The magnitude of ζ is governed by the surface charge density and the electrolyte concentration. Skin tissue, for example, has an appreciable ζ-potential within pores and a low ζ-potential elsewhere.[30, 135, 149, 199] Incorporating EOF into transport models leads to better predictions of solute delivery in transdermal iontophoresis.[30, 199] EOF is used in tumor dewatering, for example, where an electric field is used to direct the migration of water out of tumors.[137] Furthermore, Xu *et al.* were able to show sustained EOF in brain tissue during extracellular electroosmotic sampling.[93] However, EOF is not addressed in brain iontophoretic applications.

We have recently reported that brain tissue cultures have a ζ-potential of approximately -22 mV.[77, 78] We propose that a solute can be transported by virtue of the significant ζ-potential of brain tissue and the resulting EOF. Such transport will most easily be seen by prolonging iontophoretic ejections, as concentration gradients, and thus transport by diffusion, is fast on short timescales. It is possible that EOF plays a part under conditions such as Nicholson's iontophoretic ejections using 60 – 100 nA for 50 second time intervals[196] and in Herr's iontophoretic ejections periods of 30 to 60 seconds[191].

5.1.1 Theory

The degree to which electrokinetic processes take part in iontophoresis is can be assessed by knowing the Peclet number, Pe. Pe, as shown in Equation 1, is a dimensionless ratio of the time a solute requires to diffuse a characteristic distance, ā, and the time a solute requires to move the same distance with a velocity, *v* . *D* is the solute diffusion coefficient in solution.

$$\mathrm{Pe} = \frac{v\bar{\mathrm{a}}}{D} \tag{1}$$

Solute velocity, *v*, contains three components: an electrophoretic velocity, v_{ep}, an electroosmotic velocity, v_{eo}, and a pressure-induced velocity, v_{p}. We assume that v_{p} is small compared to v_{ep} and v_{eo}, and therefore is not accounted for in this derivation (refer to SI for further information). Each of the remaining two velocities is governed by the magnitude of the electric field. Equation 2 relates the electric field, *E*, to the current applied to the system, i:

$$E = j\rho_{\mathrm{E}} = {}^{i}\!/\!{}_{\mathrm{A}}\,\rho_{\mathrm{E}} \tag{2}$$

where *j* is the current density, ρ_{E} is the resistivity of the fluid, and A is the cross-sectional area. Equations 3 and 4 define electrophoretic and electroosmotic velocities as products of electric field and the corresponding mobility, μ.

$$v_{\mathrm{ep}} = \mu_{\mathrm{ep}} E \tag{3}$$

$$v_{\mathrm{eo}} = \left({}^{-\varepsilon\zeta}\!/\!{}_{\eta} \right) E = \mu_{\mathrm{eo}} E = \left({}^{-\varepsilon\zeta}\!/\!{}_{\eta} \right) \frac{i\rho_{\mathrm{E}}}{\mathrm{A}} \tag{4}$$

Equation 4 shows that the electroosmotic velocity is a function of the ζ-potential of the matrix (ζ), and the permittivity (ε) and viscosity (η) of the fluid. Incorporating Equations 2 through 4 into Equation 1 yields a theoretical calculation of Pe, Pe_T, in Equation 5 based on measurable properties.

$$\mathrm{Pe_T} = \frac{i\rho_E \bar{a}}{A D}\left[\mu_{ep} - \varepsilon\zeta / \eta\right] \tag{5}$$

The concentration profile of a solute being transported into tissue by iontophoresis in the case where μ_{ep} and μ_{eo} are both zero is governed only by diffusion. For the case in which the iontophoretic current is on long enough to reach steady-state,[191] the concentration profile takes on the familiar shape described by Equation 6.[200] Here, we have made the assumption that the solute emanates from a hemispherical source. In Equation 6, the concentration, C, is a function of the concentration at the surface of the hypothetical hemisphere of radius, ā, the maximum concentration, C_0, and the distance from the hemispherical surface, r.

$$C = C_0\,\frac{\bar{a}}{r} \tag{6}$$

In the case where there is convection as well as diffusion, we can solve for the steady-state condition in the hemispherical coordinate system as follows. Equation 7 describes solute flux:

$$J = Cv - D\nabla C \tag{7}$$

where *J*, and *v* are the flux and velocity of the solute, respectively. The first term in the equation refers to the flux due to convection, which includes both v_{eo} and v_{ep}. The second term relates to the diffusional flux resulting from a concentration gradient. We assume the electric field distribution from the pipette tip is equal to the field distribution from a hemispherical electrode, i.e., $E(\mathrm{r}) = \frac{\bar{a}^2}{\mathrm{r}^2}E_0$ where E_0 is the field at r = ā, leading to Equation 8.

$$J = C(\mathrm{r})\mu_{obs}\frac{\bar{a}^2}{\mathrm{r}^2}E_0 - D\,\frac{dC(\mathrm{r})}{d\mathrm{r}} \tag{8}$$

The observed mobility, μ_{obs}, is the sum of μ_{eo} and μ_{ep}. Note that in the case of no electric field, the electrokinetic mobility is zero and the flux is governed solely by the diffusion of the solute. Steady-state is achieved in a spherical coordinate system when $dr^2 J/dr = 0$. Thus, Equation 9 describes the steady-state condition.

$$\mu_{obs} E_0 \bar{a}^2 \frac{dC}{dr} - 2rD\frac{dC}{dr} - r^2 D\frac{d^2C}{dr^2} = 0 \tag{9}$$

$$\left(\frac{Pe}{\rho^2} - \frac{2}{\rho}\right) C' = C'' \tag{10}$$

Equation 10 is Equation 9 with the derivatives with respect to radius indicated as primed quantities, the dimensionless distance, ρ, is r/ā, and Pe is the based on the electric field at the tip ($\rho = 1$), i.e,

$$\mathrm{Pe} = \frac{\mu_{obs} E_0 \mathrm{a}}{D} \tag{11}$$

This equation can be solved by solving the first order differential equation for the function F = C', and then solving the resulting equation for C' by integration with boundary conditions:

Boundary Condition 1: $C(\rho \to \infty) = 0$

Boundary Condition 2: $C(\rho \to 1) = C_0$

$$C(\rho) = C_0\left(\frac{1 - e^{-\mathrm{Pe_E}/\rho}}{1 - e^{-\mathrm{Pe_E}}}\right) \tag{12}$$

where $\mathrm{Pe_E}$ is the experimental Peclet number. When the electrokinetic effects are negligible, $\mathrm{Pe_E}$ tends to zero. Expanding the exponentials as Taylor series and truncation of quadratic and higher order terms leads to the recovery of Equation 6.

We hypothesize that a larger magnitude tissue ζ-potential will be associated with larger ejection distance in a given time period. As a tissue's ζ-potential cannot be altered, we will test this concept, using synthetic poly(acrylamide-*co*-acrylic acid) hydrogels are used as tissue models with varying ζ-potentials. We examine the degree of fluorescent dextran penetration as a function of matrix ζ-potential and applied current. We also show that prolonged ejections do not create cell death in brain tissue as compared to controls. Finally, we use tris(2,2'-bipyridine)ruthenium ($Ru(bpy)_3^{2+}$) as a representative cationic solute for which electrophoresis and electroosmosis are significant and in the same direction. By understanding the EOF in both the delivery system and in the tissue itself, we can estimate the ejected solute distribution.[198]

5.2 EXPERIMENTAL

5.2.1 Chemicals and Solutions

Unless otherwise noted, the following materials were purchased from Sigma (St. Louis, MO) and used as received. Solutions were prepared with Millipore Synthesis A10 system 18 MΩ purified water (Millipore, Billerica, MA). Glucose-free HEPES-buffered salt solution (G-f HBSS) contained in mM: 143.4 NaCl, 5 HEPES, 5.4 KCl, 1.2 $MgSO_4$, 1.2 NaH_2PO_4, and 2.0 $CaCl_2$. G-f HBSS was filtered, stored frozen, warmed to room temperature, and ultrasonicated for ten minutes before use. HBSS contained the same quantities as G-f HBSS with an additional 10 mM D-(+)-glucose and underwent the same preparation and storage process. GBSS was made up of 27.5 mM D-(+)-glucose and filtered 2.7 mM $MgSO_4$ supplemented Gey's Balanced Salt solution. GBSS was stored in the refrigerator and warmed to 37 °C before use.

Culture medium contained the following from Gibco (Invitrogen, Eugene, OR): 50 % Opti-MEM, 25 % heat-inactivated Horse Serum, and 25 % Hanks' Balanced Salt Solution, supplemented with 2 % B-27 vitamin and 1 % D-(+)-glucose from Sigma.[201] Medium was filtered, refrigerated for storage, and warmed to 37 °C before use.

5.2.2 Fluorophores

The following dextran conjugates were obtained from Invitrogen. Texas Red dextran conjugate 70 kDa (**TR70**) and Texas Red dextran conjugate 3 kDa (**TR3**) were diluted to 0.06 mM and 0.2 mM, respectively with G-f HBSS, filtered, and frozen until use in the current ejection experiment. Tris(2,2'-bipyridine)ruthenium (abbreviated $Ru(bpy)_3^{2+}$) from Sigma was diluted to 1.3 mM in 150 mM NaCl supplemented with 5 mM HEPES, pH 7.4 in the high electrolyte solution, and diluted to 1.3 mM in 5 mM NaCl supplemented with 5 mM HEPES, pH 7.4 in the low electrolyte solution.

A **TR70/F70** mixture was made in G-f HBSS with the final concentration of 0.19 mM **TR70** and 0.29 mM **F70** for use in ζ-potential measurements. For diffusion coefficient measurements, the following fluorophores were dissolved in G-f HBSS to final concentrations of: **TR70** (0.03 mM), **F70** (0.03 mM), **TR3** (0.67 mM), and $Ru(bpy)_3^{2+}$ (3.51 mM). A stock solution of 0.35 mM propidium iodide in GBSS was frozen until use for cell death analysis.

5.2.3 Determination of Diffusion Coefficients

Diffusion coefficients were determined as described in Beisler *et al.*[202] G-f HBSS mobile phase pumped through the system using a Pico Plus syringe pump (Harvard Apparatus, Holliston, MA). The sample solutions were injected using an HP 1050 autosampler (Hewlett-Packard, Palo Alto, CA) into a 1 μL loop in a VICI 6-port Cheminert Injector (Houston, TX). The detector from an

ISCO 3850 Capillary Electropherograph (Teledyne ISCO, Lincoln, NE) was used for UV detection (215 nm) of the fluorophores. Signals were collected by Peaksimple 3.29 (SRI Inc., Torrance, CA) for analysis.

Data were imported into Origin 7.5 (Origin Lab Cooperation, Northampton, MA) for differentiation, followed by the determination of the first and second central moments using PeakFit version 4 (Systac Software Inc., San Jose, CA). Diffusion coefficients were calculated from the slopes of second moment versus first moment linear plots. In addition, errors for the diffusion coefficients were calculated based on the error of the slope, assuming negligible error in the flow rate, capillary length and capillary diameter.

5.2.4 Electrophoretic Mobility Determination by Capillary Zone Electrophoresis (CZE)

The electrophoretic mobilities of the fluorophores in G-f HBSS were determined via CZE with diode array UV absorbance detection using 50 μm inner diameter (ID) capillaries and an Agilent CE system (Agilent Technologies, Palo Alto, Ca). Hydrodynamic injection (25 mbar, 4 second) was employed, and all experiments were performed at 25°C. For **TR70** (λ_{detn} = 595 nm), **TR3** (595 nm), **F70** (494 nm), and $Ru(bpy)_3^{2+}$ (452 nm) an unmodified fused silica capillary (Polymicro Technologies, Phoenix, AZ) was employed. The capillary was preconditioned with 1 M NaOH for 15 minutes, 18 MΩ-cm water for 15 minutes and G-f HBSS for 15 minutes, and was flushed with running buffer for 2 minutes in between injections. Rhodamine B (544 nm) was used as a neutral flow marker. The capillary was 33.0 cm in total length, 8.5 cm to the detector, and the separation voltage was 6.0 kV (182 V/cm). Fluorophores were dissolved in G-f HBSS and had concentrations ranging from 0.3 to 1.7 mM.

5.2.5 Synthesis of Hydrogels

Poly(acrylamide-*co*-acrylic acid) hydrogels were prepared with the purpose of creating matrices with different ζ-potentials and tortuosities similar to those of brain tissue[18] with a thermally-initiated radical polymerization reaction. The total weight of acrylic acid, acrylamide, and bisacrylamide was kept constant (279 mg/5.00 mL) while the w/w ratios of acrylic acid and acrylamide were of 25 %, 10 % and 0 %. The bisacrylamide cross-linker was maintained at a fixed weight percentage of approximately 1.4 %.

Table 5.1. Hydrogel compositions

	25%		**10%**		**0%**	
	weight (mg)	mmol	weight (mg)	mmol	weight (mg)	mmol
Acrylamide	206.0	2.90	247.5	3.48	275.0	3.87
Acrylic Acid	69.0	0.96	27.5	0.38	0.0	0.00
Bisacrylamide	4.0	0.03	4.0	0.03	4.0	0.03

The reagents were weighed and dissolved in 4.5 mL of ultrapure water (Cayman Chemical, Ann Arbor, MI) and stirred vigorously for 5 minutes. The solutions were then titrated to a pH range of 7 to 8 using an aqueous 1 M NaOH solution. The final solution volumes were brought to 5.0 mL with ultrapure water. The polyacrylamide solutions were then deaerated with nitrogen for 20 minutes at room temperature. Immediately following, 5.0 mg of APS (0.02 mmol) and 5.2 μL of TEMED (0.03 mmol) were quickly added to each solution, which was then vigorously stirred for another 3 minutes at room temperature. Each clear, colorless solution was poured into a 50 mm x 16 mm Pyrex glass dish and placed inside an oven at 100 ± 5 °C for 2 hours. The Pyrex dishes were removed from the oven and allowed to cool for 10 minutes at room temperature. Using a glass pipette tip, the colorless and clear hydrogels were separated from the Pyrex dish walls and slowly peeled from the bottom of the dish. The hydrogels were independently placed in plastic dishes filled with approximately 25 mL G-f HBSS solution and shaken lightly at 10 °C overnight. The buffer solution was exchanged the following day with 25 mL of fresh G-f HBSS, placed back in the shaker at 10 °C for another 24 hours. Finally, the G-f HBSS was exchanged once more (25 mL), and the hydrogels were placed in the refrigerator where they were allowed to equilibrate. A final pH check was performed to assure the hydrogels were pH 7.40 with full immersion of the probe into the hydrogel before further characterization.

5.2.6 ζ-Potential and Tortuosity

The experimental apparatus was used without modification from our previously reported setup.[77] Briefly, a four-electrode potentiostat coupled with a differential amplifier and a pair of reference electrodes with Luggin capillaries was placed in the hydrogel. G-f HBSS was used as the electrolyte solution in the reservoirs. An Olympus IX71 inverted fluorescence microscope (Melville, NY) imaged the experiment with an Olympus UPlan Apo 4× objective lens and a charge-coupled device camera (ORCA-285 Hamamatsu, Hamamatsu City, Japan). A DA/Fl/TA-3X-A triple-band “Pinkel” filter set (Semrock, Rochester, NY), with exciter 1 at 387 nm, exciter 2 at 494 nm, exciter 3 at 575 nm, triple-band dichroic mirror: 394–414 nm, 484–504 nm, 566–586 nm, emitter: 457, 530, 628 nm was used. Image acquisition and post-processing was completed using SimplePCI 6.0 software from Compix (Cranberry, PA).

In order to set the exposure times, a piece of hydrogel was injected with each fluorophore solution separately. A fresh piece of hydrogel was cut to size and placed in the apparatus channel on the microscope stage. Using a P-2000 capillary puller from Sutter (Novato, CA), a 150 μm ID fused-silica capillary was pulled to a tip opening of approximately 12 μm to create an injection capillary. The injection capillary was filled with the **TR70/F70** fluorophore mixture and lowered into the hydrogel using a Sutter MP-285 micromanipulator to a depth of half the hydrogel's thickness. The injection capillary was connected to the FemtoJet® express (Hamburg, Germany) to deliver a pressure injection via a compressed nitrogen tank (Valley Natural Gas, Wheeling, WV). The injection pressure was set to 200 to 250 hPa for 0.2 to 0.5 seconds and 0 to 20 hPa compensation pressure. The exact parameters were varied within these ranges so that the volume of ejected fluorophore was appropriate for the sensitivity and dynamic range of the CCD camera. Following fluorophore ejection, the injection capillary was removed from the hydrogel. The Luggin capillaries were lowered to a depth of half the hydrogel's thickness on either side of the injection spot. This process was completed an average of two times per hydrogel piece, and all experiments were conducted at ambient temperature.

An electric field between 60 V/m and 250 V/m was applied to each run. One image was acquired every second. The electric field was monitored at the two Luggin capillaries and at the platinum electrodes in the reservoirs by two multimeters to ensure accurate control of the electric field. The velocities of the **TR70** and **F70** fluorophores were measured in post-processing. Fluorophore positions were recorded for 6 to 9 timepoints (30 to 60 seconds apart) per experimental run to arrive at an average velocity. The ζ-potential and tortuosity for each hyrogel were calculated from the average velocities as previously described.[77]

5.2.7 Porosity of Hydrogels

The water content of each hydrogel was determined by dehydration and the mass of water lost. A 10 mm x 10 mm section of hydrogel was cut and placed inside of a pre-weighed 1.8 mL ROBO autosampler vial (VWR, West Chester, PA). The aggregate weight was recorded for each vial, and placed in an oven at 110 °C for several hours until completely dehydrated. The vial was removed from the oven and reweighed. The water content, by weight, was determined by subtracting the post-dehydration weight from the pre-dehydration weight. A minimum of three sections of each type of hydrogel was completed to give with a final porosity data provided as an average with standard error of the mean.

5.2.8 Conductivity of Hydrogels

Due to the high porosity of the hydrogels, the conductivity was assumed to be that of G-f HBSS. The conductivity of G-f HBSS was measured using a CON 6/TDS 6 conductivity/TDS meter (Eutech Instruments Pte Ltd/Oakton Instruments, Vernon Hills, IL).

5.2.9 Organotypic Hippocampal Slice Cultures (OHSCs)

The organotypic hippocampal slice culture (OHSC) method, developed by Stoppini *et al.* was used with slight variations.[84] The following procedures were approved by the University of Pittsburgh IACUC. Bilateral dissections of the hippocampi were done on 9-day postnatal Sprague-Dawley albino rats. The hippocampi were chopped along the transverse axis to 350 μm thick slices using a McIlwain tissue chopper (The Mickle Latoratory Engineering, Surrey, England). The slices were placed on 0.4 μm PTFE insert membranes (Millipore, Bedford, MA) and incubated over 1.2 mL of medium at 36.5 °C in 5 % CO_2/ 95 % air for 6 to 8 days. Culture medium was exchanged every 2 to 3 days. Prior to experiments, culture medium was replaced with 37 °C GBSS and incubated for thirty minutes. A second GBSS exchange followed for another incubation period of 30 minutes. A last exchange to 37 °C HBSS and incubation for 30 minutes was done prior to experimental use.

5.2.10 Electrokinetic Ejections into Hydrogels

Borosilicate pipettes with filaments (1 mm × 0.58 mm, 4 inches long) (A-M Systems, Inc., Carlsborg, WA) were pulled using the Sutter P-2000 capillary puller to tips of approximately 2 μm inner radii. Tip size and shape were measured using an Olympus BX41 optical microscope. Figure 5.1 shows a 1/4" thick PVC cell with a 1 cm by 1 cm space in its center and a 1 mm wide × 1 mm high × 2.2 cm long channel milled at its base. The cell was slightly larger than the standard cover slip that was super-glued to its base. The cell was secured on an Olympus IX81 inverted fluorescence microscope stage and imaged with a high resolution charged-coupled device camera (ORCA-ER).

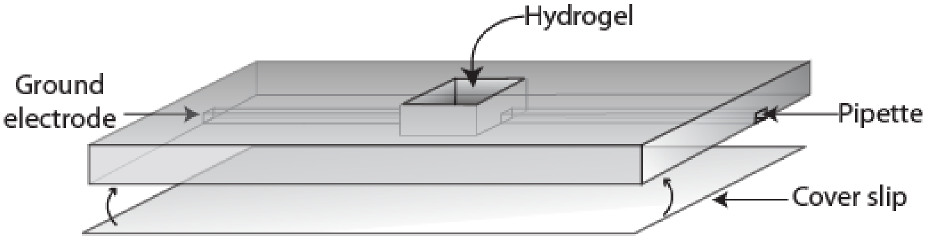

Figure 5.1. Hydrogel cell

A coverslip was super-glued to the base of the cell. An approximately 6 mm thick hydrogel square was placed in the center space of the cell. A pulled borosilicate pipette filled with fluorophore solution was inserted into the cell and hydrogel through the channel. On the other end of the channel, a Ag ground electrode was inserted into the hydrogel.

Hydrogel sections were cut to size and carefully placed in the given space. Careful attention was made to ensure complete hydrogel contact with the exposed cover slip. The pulled borosilicate pipette was carefully threaded through one side of the channel and into the hydrogel. A silver wire ground electrode (0.3 mm diameter) was threaded through the other side of the cell and was inserted a few millimeters into the hydrogel. The distance between the pipette tip and the ground electrode was always more than 3.5 mm. A second Ag wire, which is called the working electrode, was inserted into the back end of the pipette. The current source was either a Digital Midgard™ Precision Current Source iontophoretic pump (Stoelting Co., Wood Dale, IL) or a Princeton Applied Research 173 potentiostat (PAR) (Princeton, NJ). They were attached to the secured electrodes in a circuit containing a relay switch as shown in SI Figure 5.4. Image sequences were acquired using MetaMorph 7.6.2.0 software (MDS Analytical Technologies, Sunnyvale, CA) using one of the following Olympus objective lenses: UPlan Fl 4×, UPlan S Apo 10×, and a long working distance LUCPlan Fl N 40×. MetaMorph software triggered the onset and cessation of current during image acquisition. The PAR was used in **TR70** ejections with currents of 0.1, 0.2, 0.4, 0.5, and 0.6 μA. The PAR setup included a 0.3 mm diameter platinum (Pt) electrode as the working electrode in order to avoid pipette clogging due to the formation of AgCl in the pipette. The potential across the system was monitored by either the Midgard™ pump or the PAR potentiostat. Currents ran for 270 to 840 seconds, depending on estimated times to steady-state.

Image sequences were analyzed by drawing a line scan from approximately the center of the pipette tip to the end of the field of view on the same axis as the pipette lumen. Intensity data were recorded along the line scan before the initiation of current (background intensity), and at 30 seconds intervals after the current was applied. Background intensity was subtracted from line scan intensities. Since concentration is related to intensity measured, we can replace concentration, C, in Equation 12 with intensity, I. Reported intensity values are between 0 and 4095. Values of I_0, I_1, and Pe_E were determined by nonlinear fitting of Equation 13 to data with Mathcad 14 (PTC, Needham, MA). I_1 is included to correct for baseline intensity.

$$\mathrm{I}(\rho) = \mathrm{I}_0\left(\frac{1-\mathrm{e}^{-\mathrm{Pe_E}/\rho}}{1-\mathrm{e}^{-\mathrm{Pe_E}}}\right) + \mathrm{I}_1 \qquad (13)$$

5.2.11 Electrokinetic Ejections into OHSCs

Experiments in the OHSC were set up as shown in Figure 5.2 with the Digital Midgard™ iontophoresis pump. An insert membrane with an OHSC was placed in a dish with HBSS. A Ag ground electrode was remotely secured, such that it made contact with the HBSS bath. A pulled borosilicate pipette filled with fluorophore solution was positioned at a 20° angle using a manipulator arm on a Narishige NMN-21 micromanipulator (Tokyo, Japan). The tip was inserted into the CA1 region of the OHSC. A Ag working electrode was threaded into the distal end of the pipette to make fluid. The electrode circuitry is also the same as the hydrogel experiment. A current of 0.5 μA was applied using the iontophoresis pump for 270 seconds for OHSC experiments.

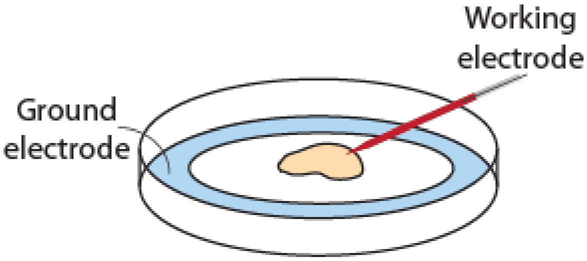

Figure 5.2. OHSC experimental setup

An OHSC and its attached membrane are placed over HBSS in a dish. A ground electrode is placed remotely in the bath. A working electrode is placed distally in a borosilicate pipette that is inserted into the OHSC at a 20° angle.

OHSCs analyzed for cell death following ejection were subjected to identical conditions, with the exception that the ejection solution only contained HBSS, without fluorophore, to avoid interference with propidium iodide (PI) fluorescence. OHSCs were incubated for 24 hours over culture medium supplemented with PI (final concentration of 7 μM) following current ejection experiments. Positive cell death controls were subjected to a drop of methanol placed on top of the OHSCs prior to the 24 hour incubation with PI.[97] Negative controls were subjected to the same procedure as experimental OHSCs, without placement of the pipette and application of current. Following incubation, the medium was exchanged with the same GBSS-GBSS-HBSS procedure described earlier and imaged on the IX81 inverted fluorescence microscope with the 4× UPlan Fl objective lens. PI was imaged using a 560/25 excitation filter, a 625/26 emission filter, both obtained from Olympus, and the Semrock triple-band dichroic mirror described earlier. A circular region of interest (50 μm^2) was used to measure the average intensity within the area of injection. Cell death was analyzed as described by Hamsher et. al.[97] Briefly, PI intensity of OHSCs used in ejection experiments were compared to positive and negative cell death controls. Control OHSC PI intensities were averaged for each experimental day, and compared using Equation 14 to experimental PI intensities of experiments run the same day.

$$\%\ \text{Cell Death} = \frac{\text{PI intensity (experimental control)- PI intensity (negative control)}}{\text{PI intensity (positive control)- PI intenstiy (negative control)}} \times 100\% \qquad (14)$$

5.2.12 Two-pipette experiments

A second channel was milled perpendicular to the long axis of the cell shown in Figure 5.1, from the edge of the cell to the center of the square hydrogel pocket. A hydrogel was placed in the pocket and a pipette filled with **TR70** solution was placed as described for the hydrogel experiments. A counter pipette, filled with G-f HBSS, was placed in the perpendicular channel and inserted into the hydrogel. The pipettes were aligned such that the tips were on the same z-axis plane and 13 μm apart. The control experiment was set up with the ground electrode placed remotely in the hydrogel as described in the hydrogel experiments. The second setup placed the ground electrode in the distal end of the counter pipette, in contact with the solution. 0.5 μA of current was applied for 30 seconds.

5.3 RESULTS

5.3.1 Properties of the fluorophores, hydrogels, and iontophoresis capillaries

Table 5.2 summarizes the diffusion coefficients and mobilities of the fluorophores.

Table 5.2. Fluorophore properties[a]

	Observed Free Diffusion Coefficient (D) (10^{-10} m^2/s)	Electrophoretic Mobilities (μ_{ep}) /(10^{-9} m^2/Vs)
TR70	0.37 ± 0.02 (N = 32)[b]	0.46 ± 0.03 (N = 3)[b]
F70	0.38 ± 0.01 (N = 48)[b]	-8.80 ± 0.2 (N = 3)[b]
TR3	1.05 ± 0.05 (N = 48)[b]	2.56 ± 0.04 (N = 3)[b]
$Ru(bpy)_3^{2+}$	3.70 ± 0.34 (N = 48)[b]	25.86 ± 0.02 (N = 3)[b]

[a]Each entry is a mean ± standard error of the mean (SEM). [b]Number of replicates.

Electrokinetic flow in the hydrogel is partially governed by the properties of the hydrogel. Table 5.3 shows the ζ-potential and electrokinetic tortuosity of each hydrogel. There is a roughly linear relationship between the w/w percentage of acrylic acid and the ζ-potential. The 25% acrylate-content hydrogel has a ζ-potential similar to the OHSC. Hydrogel tortuosity was more difficult to control than ζ-potential, although consistent within each hydrogel. Tortuosities reported in Table 5.3 are determined by 70 kDa dextran conjugates using an electrokinetic method that measures ζ-potential and tortuosity simultaneously.[77, 78] Hydrogel porosity was determined by a series of dehydration experiments. The 25% acrylate-content hydrogel composition had a larger percentage of water than the hydrogels with lower amounts of acrylic acid. The 25% acrylate-content hydrogel contained 98.3 ± 0.1 % water, while the 10 % and 0 % acrylate-content hydrogels contained 97.5 ± 0.6 % and 96.6 ± 0.2 % respectively (N = 3 for each measurement, mean ± SEM). Due to the high porosity values, conductivity was assumed to be equal to the conductivity of the buffer, which was measured to be 1.62 S/m.

Table 5.3. Hydrogel Properties

% Acrylic Acid	ζ-potential	70 kDa Electrokinetic Tortuosity	Number of Runs (N)
0	-0.25 ± 0.04	1.69 ± 0.16	4
10	-9.5 ± 0.2	1.61 ± 0.08	4
10	-15.2 ± 0.8	1.46 ± 0.07	5
25*	-23.0 ± 0.3	2.36 ± 0.18	4
25	-24.7 ± 1.7	1.71 ± 0.18	9
25	-22.1 ± 0.6	1.07 ± 0.03	6
*Note: the pH for this 25% hydrogel was not adjusted to pH 7-8 before radical polymerization.			

Herr et al. were able to quantify iontophoretic solute ejections into free solution relative to a neutral marker.[198] They included a discussion of the effects of ionic strength and pH on the pipette ζ-potential. By accounting for these two parameters, we are able to apply their findings to our electrolyte conditions (G-f HBSS: pH 7.4, ionic strength ≈ 0.15 M). The resulting pipette ζ-potential of approximately -10 mV agrees with the literature on other forms of borosilicate glass.[203-205] This agrees with our experimental observation that the pipette ζ-potential must be more positive than -11 mV because experiments with **F70** ($\mu_{ep} = -8.8 \times 10^{-9}$ m^2/Vs) solution do not result in ejections of **F70** from the pipette (data not shown).

5.3.2 Two-pipette experiment

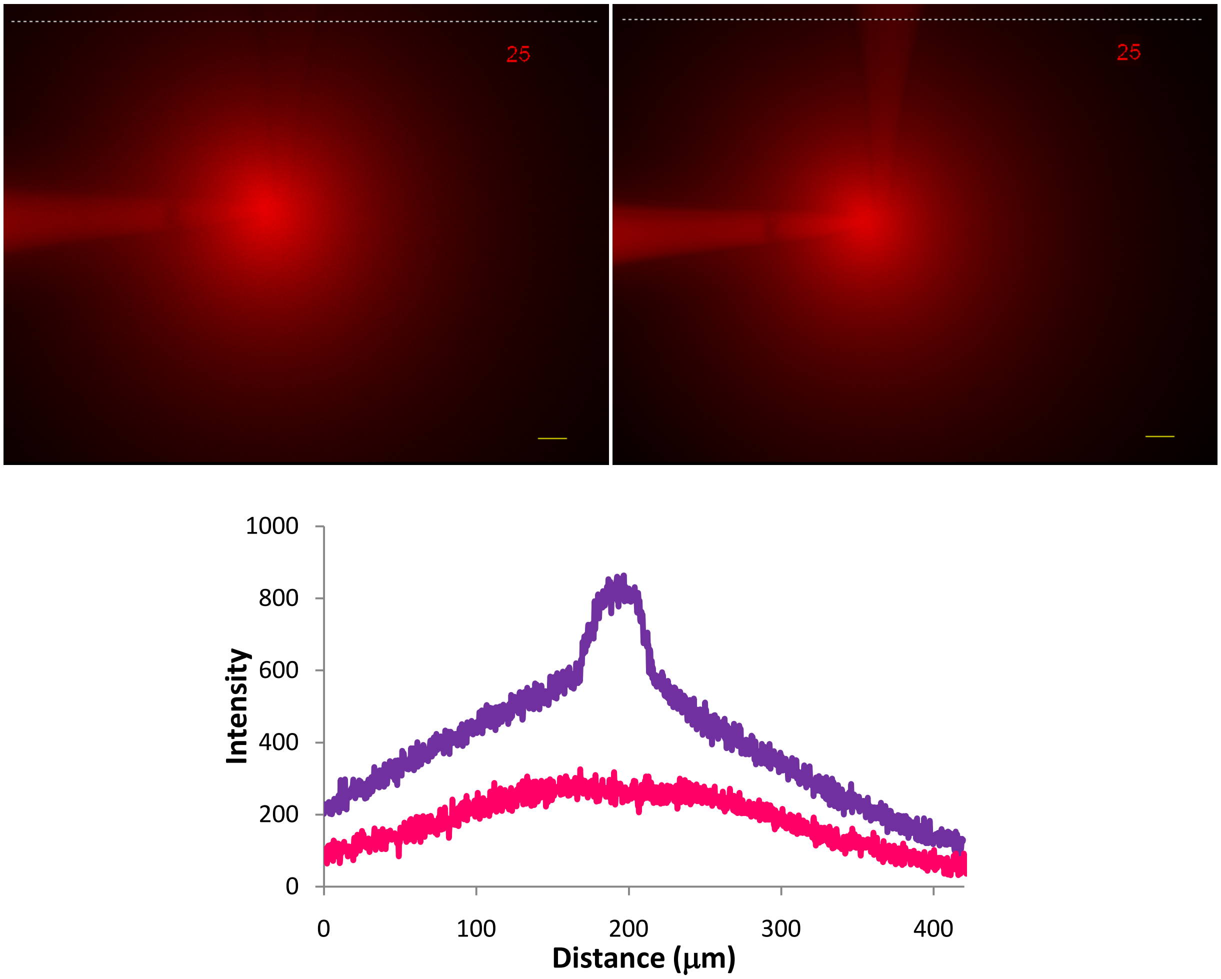

Figure 5.3. Two-pipette experiment

Figure 5.3 shows the results from the two-pipette experiment in the -23.0 mV ζ-potential hydrogel with 0.5 μA applied current. In both panels, two pipettes sit perpendicularly to one another. The horizontal ejection pipette is filled with TR70 solution, and the vertical counter pipette is filled with G-f HBSS electrolyte. The left panel shows an ejection where the ground electrode is placed remotely in the hydrogel. The right panel shows the identical setup with the ground electrode placed in the distal end of the counter pipette. Both images are acquired after 25 seconds of applied current. The scale bar represents 20 μm. Fluorescence intensity is measured along the dotted lines at the top of both images and is shown in the bottom panel. The pink line shows the fluorescence intensity corresponding to the left panel, and the purple line corresponds to

the right panel. The bottom panel demonstrates that fluorescent material moves into the pipette in a directed movement with the current flow. Furthermore, there is a greater intensity outside of the pipette in the right panel than in the left.

We tested the idea that a neutral fluorophore can be directed from one pipette to another. Two iontophoresis pipettes were placed with their tips approximately 13 μm apart in a large ζ-potential (-23.0 mV) hydrogel (see Figure 5.3). **TR70** in the pipette containing the positive working electrode is ejected into the hydrogel. After 25 seconds, the pipette containing the ground electrode shows more fluorescence than the surrounding hydrogel, indicating transport of the fluorophore into the pipette with the ground electrode. However, when the ground electrode is placed in the hydrogel, the same pipette but without the ground electrode has a fluorescence intensity similar to the adjacent hydrogel.

5.3.3 Time to steady-state

Steady-state is defined here as a constant intensity at $\rho = 1$ for two 30 second intervals. SI Figure 5.1 shows intensity versus distance plots as well as a plot of the intensity versus time of two experiments. The first experiment reaches steady-state, while the second is approaching steady-state within the same amount of time. SI Table 5.1 gives times to steady-state. The average times to steady-state are 207 and 423 seconds for **TR70** and **TR3**, respectively in the -0.25 mV ζ-potential hydrogel. The time to steady-state correlates with increasing current for **TR70** in the -24.7 mV hydrogel. Some iontophoretic ejections were truncated prior to steady-state to avoid concerns about electrochemical reactions in the pipette and evaporation of water from the hydrogel.

5.3.4 Correlation between ζ-potential and solute penetration distance:

Figure 5.4 represents intensity profiles from steady-state iontophoretic ejections of **TR70** and **TR3** in hydrogels. Data points are the averages of the dimensionless distance, ρ, from the tip at which the intensity relative to the intensity at $\rho = 1$ is 75, 50, and 25 %. The solid lines represent the intensity profiles (Equation 13, $I_1 = 0$) that pass through the data point for intensity equal to half of the maximum intensity. The dotted lines denote the intensity profile expected for solute transport entirely by diffusion from a hemispherical source ($C / C_0 = 1/\rho$). Curve fitting of the data from each experiment to Equation 13 produced correlation coefficients greater than 0.98. Figure 5.4 shows that at the same point in time, the penetration distance of each solute is higher in the more negative ζ-potential hydrogel. The nearly neutral solute, **TR70**, shows the degree of EOF that occurs in each hydrogel (Figure 5.4a). More negative ζ-potentials result in faster EOF and thus a greater penetration distance. In comparison, Figure 5.4b shows this effect on **TR3**, which is noticeably carried further.

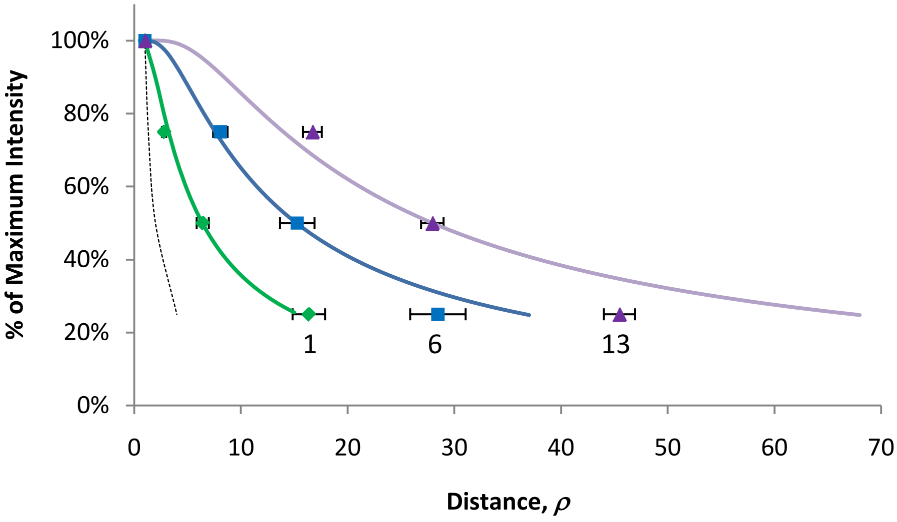

Figure 5.4a

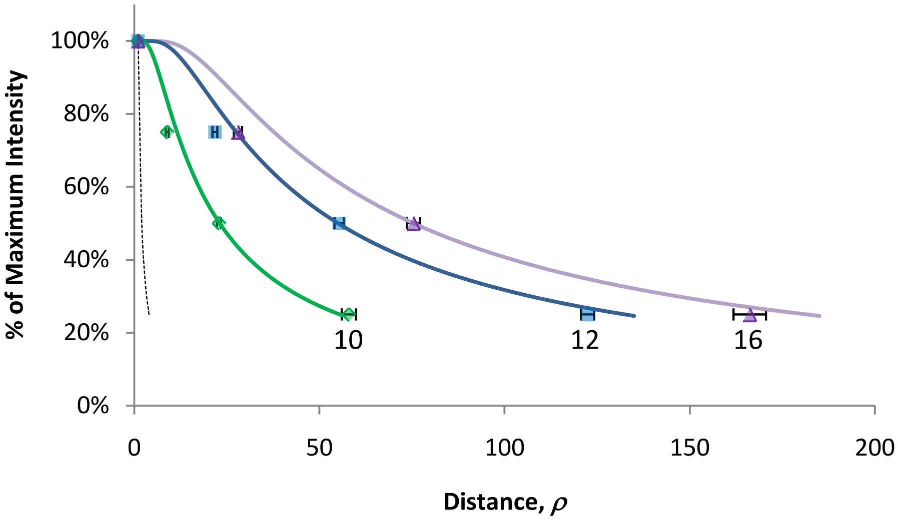

Figure 5.4b

Figure 5.4. Solute penetration distances

Figure 5.4a: Solid lines represent average intensity profiles (t = 270 seconds) from 1 μA ejections of TR70 in hydrogels of varying ζ-potentials: diamond, -0.25 mV (N = 9 intensity profiles); square, -9.5 mV (N = 11 intensity profiles); and triangle, -23.0 mV (N = 9 intensity profiles). Results for the lower ζ-potential hydrogels are at steady-state, while those for the larger ζ-potential hydrogel are approaching steady-state (row 13 in SI Table 5.1). b: average TR3 intensity profiles (t = 540 seconds) in the following hydrogels:

diamond, -0.25 mV (N = 11 intensity profiles); square, -15.2 mV (N = 8 intensity profiles); and triangle, -24.7 mV (N = 6 intensity profiles). The dotted lines show the steady-state diffusion profiles. Labels indicate the corresponding specific row in SI Table 5.1 of the experimental parameters.

5.3.5 Effect of current on concentration and Pe

Figure 5.5 shows the intensity at $\rho = 1$ and Pe_E as functions of current with tip size, exposure time, and hydrogel constant. Each data point represents a mean ± SEM of N runs (see SI Table 5.1 for values). An increase in current yields an approximate linear increase in the intensity at $\rho = 1$, and thus the concentration of ejected solute.

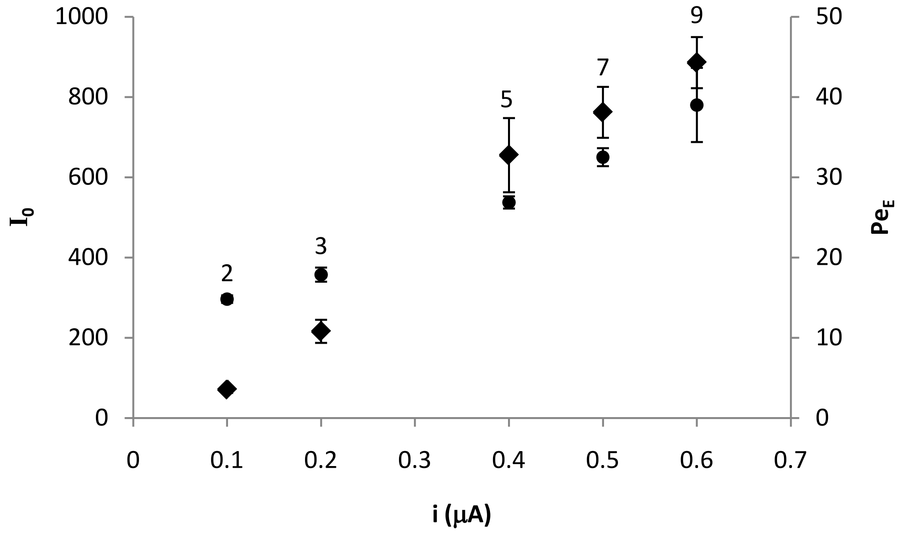

Figure 5.5. Effect of current on concentration and Pe

Figure 5.5: Impact of current on TR70 steady-state values of I_0 (represented by diamonds) and Pe (represented by circles). Ejections were done in the -24.7 mV ζ-potential hydrogel, with the same pipette size and imaged using the same exposure time. Values are taken at time point 270 seconds.

Furthermore, there is a notable approximately linear increase of Pe_E as a function of current. Increasing the current increases the penetration of the solute into the hydrogel.

5.3.6 Comparison of Pe_E with Pe_T

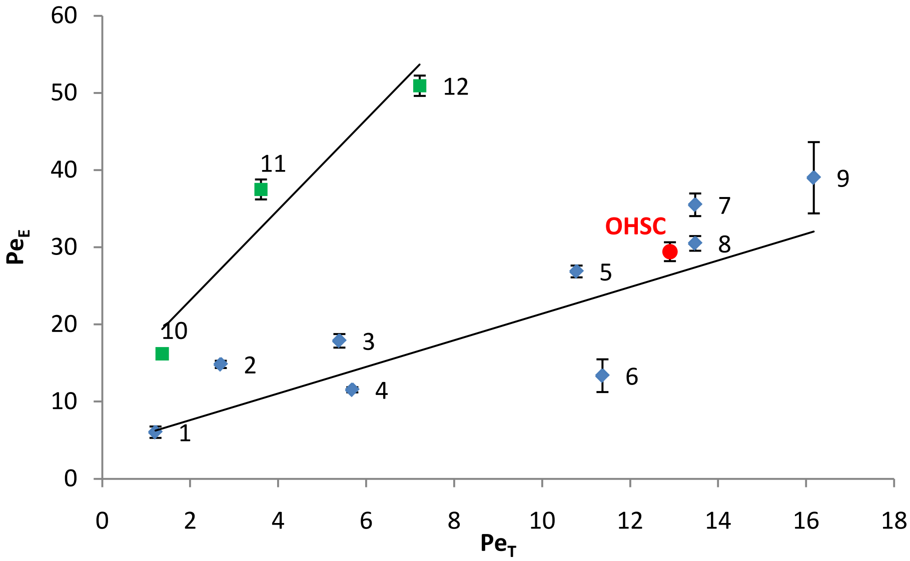

Figure 5.6. Steady-state Pe_E vs. Pe_T

Blue diamonds represent TR70; green squares represent TR3; and the red dot represents TR70 in the OHSC.

Pe_E was determined by fitting Equation 13 to the experimental steady-state intensities. Equation 5 was used to determine Pe_T. Figure 5.6 shows that Pe_E correlates linearly with Pe_T. The resulting linear regressions for **TR70** and **TR3** had respective slopes of 1.7 and 5.9 and intercepts of 4.2 and 11.4. Labels refer to the row in the supplemental table. Of 120 experiments, nine outliers were eliminated due to low correlation coefficients from the fit of Equation 13 to the experimental intensity profiles.

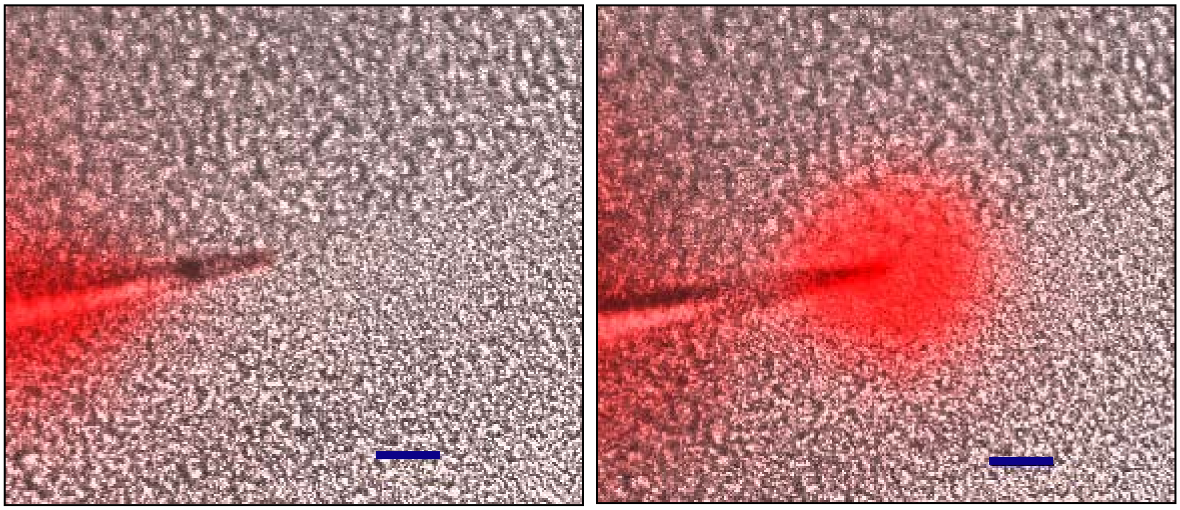

Figure 5.7. Injections into an OHSC

Fluorescence images overlaid on bright field images of the ejection of TR70 into the CA1 region of an OHSC under 0.5 μA. Left: immediately prior to applying current (t = 0 seconds). Right: current has been applied for t = 120 seconds. The scale bar represents 50 μm.

Figure 5.7 shows fluorescence and bright field image overlays of a 0.5 μA ejection of **TR70** into the CA1 region of an OHSC at t = 0 and 120 seconds. The radius of the ejected **TR70** solution, measured at t = 120 seconds, was ~85 μm. Bright field imaging during the ejection showed that applying 0.5 μA often creates a slight, temporary distortion in morphology of tissue. The tissue appears to recover within 24 hours of the ejection experiment. Ejections into the CA1 regions of OHSCs (0.5 μA for 300 seconds) showed no increase in cell death by PI staining in comparison to controls (-6 ± 4 % cell death; negative control = 0%, positive control = 100%).

5.3.7 Small, highly charged solute:

We used tris(2,2'-bipyridine)ruthenium, $Ru(bpy)_3^{2+}$, to demonstrate the effect of matrix ζ-potential and ionic strength of a solution on a small, highly charged solute. Transport of $Ru(bpy)_3^{2+}$ is affected by the hydrogel ζ-potential similarly to the dextran solutes. When distances are compared at 25 % of the maximum intensities, ejections of $Ru(bpy)_3^{2+}$ solution into -22.1 mV ζ-potential hydrogel (Pe_E = 51) reach 1.5 times further than ejections into -0.25 mV ζ-potential hydrogel (Pe_E = 24). $Ru(bpy)_3^{2+}$ was further used to investigate the effect of ionic strength on the solute ejection. Steady-state ejections within a -22.1 mV ζ-potential hydrogel of 1.2 mM $Ru(bpy)_3^{2+}$ in a 5 mM HEPES, 5 mM NaCl buffer (Pe_E = 88) travels 1.8 times further than $Ru(bpy)_3^{2+}$ in a 5 mM HEPES, 150 mM NaCl buffer (Pe_E = 51).

5.4 DISCUSSION

5.4.1 Fluorophore, hydrogel, and pipette parameters

TR70 and **TR3** are commercial products, and as such, their properties are not under our control. While **TR70** is virtually neutral, **TR3** is not (refer to Table 5.2). To assess the relative importance of electrophoresis vs. electroosmosis, we have tabulated the ratio of the ζ-potential of the solute (related to its mobility as in Equation 4, but without the negative sign) to the ζ-potential of the hydrogels in SI Table 5.1. All of these ratios are significantly greater than unity except for two – **TR70** and **TR3** in the 0% hydrogel. Thus, with these exceptions, the observations relating to electric-field-dependent dextran transport are caused by electroosmosis in the hydrogels. Nonetheless, in discussions below concerning Pe_T, we do include the electrophoretic mobility.

We estimate the pipette ζ-potential to be about -10 mV. In situations like this where there are two media with different ζ-potentials, pressure is created.[206] When the hydrogel's ζ-potential magnitude is small, there is the possibility of transport by pressure-induced flow arising from the larger magnitude of ζ-potential in the pipette. In cases where the hydraulic permeability is low in the medium with the larger ζ-potential magnitude (pipette), and the hydraulic permeability is high in the medium with the smaller ζ-potential magnitude (hydrogel), pressure-induced fluid flow in the hydrogel is likely to be small.[22] We cannot, however, rule out some contribution from pressure-induced flow.

5.4.2 Time to steady-state

The time to steady-state appears to be roughly correlated with the solute penetration distance for **TR70** for which we have the most data. In an electrochemical context, Zoski et al. have determined the time to reach a given fraction of the steady-state measured quantity, e.g., current or potential, for spherical and disc microelectrodes under diffusion controlled galvanostatic and potentiostatic conditions.[207] For a constant current flowing at a hemispherical microelectrode, analogous to the data reported here, the time depends on the closeness to steady-state, the diffusion coefficient of the solute, and the size of the electrode. In the diffusion controlled case, the time to steady-state is proportional to the electrode diameter squared. We can calculate the time to steady-state assuming diffusional mass transport only with the parameters of the experiments discussed here. With a tip (i.e., hemispherical electrode) radius of 2 μm and the diffusion coefficient of **TR70**, the time to reach 90 % of the steady-state condition is about 3 seconds, and to reach 95 % is about 14 seconds. These times are short in comparison to our observations of transport from a hemispherical source by both diffusion and electrokinetic processes.

The length of time to reach steady-state could be exceptionally long with certain experimental parameters, bringing concern about the effects of the electrochemical processes occurring at the electrodes and hydrogel/ tissue losing water. To avoid these concerns, experiments did not exceed 15 minutes. Comsol simulations (see Comsol Simulation section in SI) indicate the concentration profile at this time is very similar to that of steady-state. Figure 5.4 includes two experimental conditions that were truncated just short of steady-state: **TR70** and **TR3** with 1 μA applied current in the largest ζ-potential hydrogels. **TR70** and **TR3** experiments are truncated at 270 and 540 seconds.

5.4.3 Solute penetration distance

The ζ-potential of the matrix, magnitude of applied current, pipette properties, and solute characteristics[2] should all affect the solute ejection according to Equation 5. The penetration distance of the ejection (Figure 5.4) clearly depends on the ζ-potential and thus on the EOF. Intensity profiles for the 0 % acrylate-content hydrogel (ζ = -0.25 mV) would be expected to be similar to that for diffusion alone in the absence of electrophoresis. However, the penetration distance is larger than that for diffusion for the solute **TR70**, which has a negligible electrophoretic mobility. It is possible that there is a contribution from pressure-induced flow in this case. For **TR3,** there is a significant contribution to the mass transport from electrophoresis, as well as a potential contribution from pressure-induced flow.

Unlike hydrogels, most biological matrices cannot be altered with the purpose of varying the magnitude of ζ-potential to increase solute penetration distance. Alternatives to control Pe_E are to vary the current applied and the electrolyte concentration. Concentration and Pe_E are linearly proportional to the current (see Figure 5.5). Thus varying current allows the user to influence the degree of solute penetration. To our knowledge, many have observed this phenomenon in brain tissue iontophoresis, but have not shown the quantitative linear correlation of penetration distance with current.[192, 208]

The pipette tip opening, tapering, and ζ-potential influence the electric field at the interface.[150, 192] Therefore, it is imperative to measure the pipette opening dimensions prior to use. The tips are often slightly ellipsoidal, hence we use the average radii of the short (a) and long (b) axes of the pipette tip opening, ā, to represent the radius. Measurements of the tip opening are used in Equation 2 to approximate the electric field at $\rho = 1$, E_0, and thus calculate Pe_T. Hence, the hemispherical area applied to Pe_T at the pipette tip opening is $2\pi ab$. Ejection profiles may also be affected by the pipette ζ-potential. Pipette ζ-potential can be varied with coatings, or alternatively using another pipette material, such as a fused-silica. Fused-silica glass has a more negative ζ-potential than borosilicate.[93, 203, 209]

5.4.4 Two-pipette experiments

In a matrix with significant ζ-potential, such as brain tissue or high acrylate-content hydrogel, EOF can be directed by the current path to desired regions as shown with the two-pipette experiment. Figure 5.3b shows that the fluorophore is concentrated in the pipette containing the ground electrode (the ‘counter’ pipette). The concentration of the fluorophore in the counter pipette cannot occur by diffusion alone. While certainly **TR70** can and does diffuse into the counter pipette, it cannot become more concentrated in the counter pipette (in comparison to the hydrogel nearby) by diffusion alone. Thus, in the control experiment where the ground electrode is in the hydrogel rather than the pipette there is no concentration of fluorophore in the counter pipette. Only when current is directed to flow into the counter pipette do we see concentration of the fluorophore in the counter pipette. As the electrophoretic mobility of **TR70** is on the order of 40 times smaller than the electroosmotic mobility in this experiment, the directed movement of the fluorophore is not by electrophoresis of the nearly neutral **TR70** solute. Therefore, the directed flow is a result of the significant EOF, and thereby ζ-potential of the hydrogel matrix.

5.4.5 $\mathrm{Pe_E}$ versus $\mathrm{Pe_T}$

Figure 5.6 shows that the measured $\mathrm{Pe_E}$ and the calculated $\mathrm{Pe_T}$ are linearly correlated for the two dextran conjugates, but the slopes are not unity. Among the factors that may be responsible for the lack of unit slope are the varying porosities of the media supporting EOF, uncertainty about the tip size and shape, uncertainly about pressure-induced flow, and the tortuosity of the medium. Porosity is not likely to be a factor. The ratio of $\mathrm{Pe_E}$ and $\mathrm{Pe_T}$ is the same for an OHSC and hydrogel, indicating the slope is not a result of specifics of the hydrogel, such as porosity. In simple models of porous media, volume-averaged electrokinetic flow rate is unaffected by changes in porosity.[79, 210] This is because the decrease in porosity increases the electric field (because the current density increases) and thus the local EOF increases within the pores, but at the same time, the fraction of the porous medium that is fluid, and thus is moving, decreases by exactly the same factor. Therefore, the OHSC (porosity of ~0.2)[18] has Pe values that would also be expected with the hydrogels (porosity of ~0.98).

The uncertainty about the tip may be a factor in the slope of the plots in Figure 5.6. The electric field at the tip is approximated a hemisphere in $\mathrm{Pe_T}$ to make the derivation of the steady-state concentration profile possible. In order to obtain intensity-distance profiles from images, we must accurately find the location of $\rho = 1$. This is not a simple matter. An error of ± 1 μm in determining the position of $\rho = 1$ away from a typical 2 μm radius pipette tip opening provides a 5 to 10% error in $\mathrm{Pe_E}$. As the location of $\rho = 1$ is visual, there may be a systematic error the estimation of that point.

Furthermore, a small pressure effect may arise from a ζ-potential mismatch of the pipette and the hydrogel matrix, which is not accounted for in $\mathrm{Pe_T}$ (refer to SI for further information).[211] As Table 5.3 indicates, most hydrogels and the OHSC have different ζ-potentials than the pipette. A pressure effect arises in the case of mismatched ζ-potentials[211] because the law of conservation of mass requires pressure to compensate for differences in EOF. For example, for a neutral solute being ejected into a neutral gel, $\mathrm{Pe_T}$ is zero. However, the negative ζ-potential in the pipette will create a positive pressure at the tip-hydrogel interface, creating pressure induced flow. The magnitude of the pressure depends on many factors other than the ζ-potentials, so estimating the pressure from parameters of the experiment is difficult. Nonetheless, as there is a pressure-induced velocity when $\mathrm{Pe_T}$ is zero, the y-intercept in Figure 5.6 is likely to be a reflection of the pressure at the pipette/ hydrogel interface and thus the ζ-potential mismatch.

Finally, there is the issue of the tortuosities and related factors of a medium that impede solute motion in comparison to free solution. When referring to tortuosity, we strictly imply an effect of path length. Other factors, such as molecular friction, often characterized by the Ogston model, contribute to the effect of a porous medium on molecular motion.[212] To a first approximation, electrokinetic velocity (the sum of v_{ep} and v_{eo}) will be impeded by tortuosity to the same degree as diffusion. Thus, the value of Pe, and therefore the concentration profile, should not depend at all on tortuosity. It is for this reason that we have not included tortuosity explicitly in $\mathrm{Pe_T}$. The slopes of Figure 5.6 give us reason to question this assumption. As is well-known in polyacrylamide gel electrophoresis, the impedance of the gel medium is greater the larger is an object (at constant ζ-potential of the object) traveling by electrophoresis.[212] This is viewed as a steric exclusion of solute giving rise to the molecular weight dependence of its mobility. More recently, models and experiments show that the factor by which diffusion in a hydrogel differs from diffusion in free solution varies strongly with hydrogel porosity in the range of 0.99 to 0.95 and molecular size especially when the molecular size is greater than the characteristic dimension of the fibers (i.e., diameter of a polyacrylamide chain) making up the hydrogel.[213] These are the conditions of our experiments. The foregoing tells us that we might expect a molecular-weight dependence and a hydrogel porosity dependence on the apparent tortuosity. In principle, these are questions that are addressable experimentally. However, the hydrogel porosity is unfortunately correlated with ζ-potential because the more ionic and thus higher ζ-potential hydrogel swells more than the neutral, near zero ζ-potential hydrogel.

Finally, there may be a difference between the electrokinetic and volumetric tortuosities[78]. Electrokinetic tortuosity is different than volumetric tortuosity due to its dependence on pore orientation with the electric field[79, 80] and hydrogel swelling where the electric field is high.[81, 82] The potentially systematic but unknown errors in determining electric field (the tip is not a hemisphere), in determining the location of $\rho = 1$, and pressure effects lead to a scaling factor that should not depend on molecular weight of the solute. The difference in the behavior of **TR70** and **TR3** shown in Figure 5.6 is related to molecular weight, and thus likely due to the tortuosity effects described above. The role of molecular-weight dependent friction in the observed phenomena is under investigation.

5.4.6 Ejections into OHSCs

Ejections of **TR70** solution into the CA1 regions of OHSCs demonstrate significant penetration distances, (ejection radius of ~85 μm of in 120 seconds as shown in Figure 5.7). The supplemental table shows the non-steady-state Pe_E (data points 13 – 16) along with the values for steady-state (data points 1 – 12). Note that the non-steady-state experimental sets are equally as reproducible as the steady-state experimental sets, as demonstrated by the Pe_E SEM displayed in SI Table 5.1. Pe_E of **TR70** ejections in OHSCs fall directly in line with Pe_E determined in hydrogels, indicating the hydrogels are viable models for OHSCs. Hydrogels with ζ-potentials around -22 mV were originally meant to model the OHSC that has a known ζ-potential of -22.8 ± 0.8 mV and an electrokinetic tortuosity of 2.24 ± 0.10.[77] However, ejections in OHSCs show an increased time to reach steady-state than in comparable, 25% acrylate-content hydrogels. Although ejections in OHSCs appear to be approaching steady-state after 270 seconds, the ejection profile continues to grow slightly for more than an hour. As the OHSC is only about 150 μm thick, when the distance traveled reaches distances on the order of 100 μm (ρ ~50) we can no longer assume a spherically symmetrical field or concentration profile. This topic must be further investigated to make any quantitative conclusions.

Propidium iodide analysis demonstrates that 0.5 μA ejections for fewer than 300 seconds into the CA1 region do not increase cell death in the OHSC. However, there is a slight distortion of the morphology around the ejected solute that is largely resolved within 24 hours following ejections. The ejection plume may also be slightly asymmetrical due to any anisotropy and heterogeneity within the OHSC.

Solutes can be transported further by decreasing the electrolyte concentration. Many researchers use low ionic strength solutions for iontophoretic delivery of small charged molecules.[18, 98, 198] To our knowledge, there is no standard for electrolyte concentration.[198] The electrical double layer thickness is proportional to the reciprocal square root of ionic strength. Consequently, the absolute value of the ζ-potential increases with decreasing ionic strength. Hence, the $Ru(bpy)_3^{2+}$ solution containing 5 mM NaCl creates a larger ζ-potential and consequently the solute ejection distance is 1.8 times farther than the 150 mM NaCl solution.

5.4.7 Conclusion

The major conclusion is that under appropriate conditions, the transport of a solute into a porous, aqueous medium depends strongly on the ζ-potential of the medium. We demonstrated that solute ejection distance is affected by the solute, solute-containing medium ionic strength, and hydrogel properties, as well as the current applied. Pe_E, which relates to solute penetration distance, is linearly correlated to Pe_T, which relates to measureable parameters. OHSCs have no added cell death following long-term electrokinetic ejection. Thus, this technique is applicable to living tissue for long-distance solute transport. Furthermore, results of two-probe experiments indicate that the EOF path can be directed in tissue using placement of the counter electrode.

5.4.8 Acknowledgement

We thank the NIH for support through grant GM44842.

5.5 SUPPORTING INFORMATION

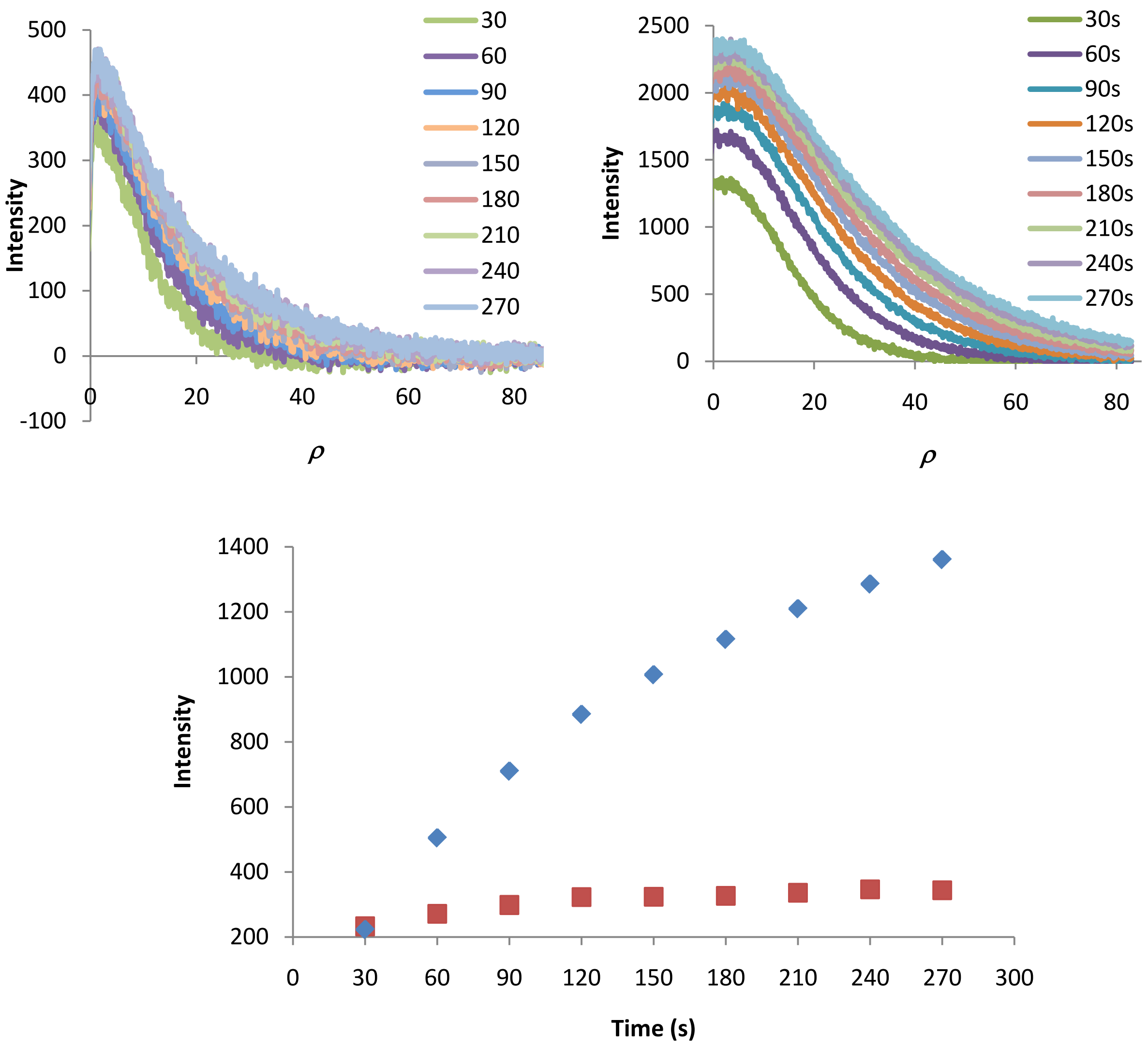

SI Figure 5.1. Steady state versus non-steady state

SI Figure 5.1 shows 30 second interval ejection profiles of **TR70** under 1 μA current in hydrogels with ζ-potentials of -9.5 (left panel) and -23.0 mV (right panel). The left panel reaches steady state by t = 270 s of applied current, while the right panel does not. The bottom panel is a plot of the intensity at ρ = 75% of the maximum intensity versus time. The red squares relate to the left panel that reach steady state as demonstrated by a slope of 0 over several time intervals.

The blue diamonds are associated with the right panel corresponding data. The right panel intensities are increasing steadily, however the slope is decreasing over time, indicating that the experiment is approaching steady state.

SI Table 5.1. Experiment summary table

Solute	Data Point	Hydrogel ζ-potential (mV)	$\left\|\frac{\zeta_{\text{hydrogel}}}{\zeta_{\text{solute}}}\right\|$	Current applied (μA)	Average Time to Steady State (s)	Pe_E	SEM	N
TR70	1	-0.25	0.43	1	207	6	0.74	9
TR70	2	-24.7	43	0.100[a]	366	15	0.47	3
TR70	3	-24.7	43	0.200[a]	492	18	0.88	5
TR70	4	-9.5	16	0.500	240	12	0.34	5
TR70	5	-24.7	43	0.400[a]	780	27	0.76	4
TR70	6	-9.5	16	1	233	13	2.1	11
TR70	7	-24.7	43	0.500[a]	953	36	1.5	4
TR70	8	-24.7	43	0.500	818	30	0.95	4
TR70	9	-24.7	43	0.600[a]	1030	39	4.6	3
TR3	10	-0.25	0.077	1	423	16	0.36	11
TR3	11	-15.2	4.7	0.500	498	37	1.3	13
TR3	12	-15.2	4.7	1	510	51	1.3	8
Solute					Non-steady State Data			
TR70	13	-23.0	40	1	-	27	1.4	9
TR3	14	-22.1	6.8	1	-	52	3.2	10
TR3	15	-24.7	7.6	0.5	-	69	4.9	6
TR3	16	-24.7	7.6	1	-	73	2.5	6

[a] Current applied through the PAR circuit. All other experiments were run using the Digital Midgard™ Precision current source.

The ζ-potential of the solute is calculated by SI Equation 1 using the electrophoretic mobility, μ_{ep}, and the permittivity (ε) and viscosity (η) of the water.

$$\zeta_{\text{solute}} = \frac{\eta}{\varepsilon}\mu_{\text{ep}} \quad \text{(S1)}$$

5.5.1 Comsol Simulations:[¥]

[¥] Comsol simulations were primarily completed by Manyan Wang in the Weber lab.

A commercial finite element method (FEM) was used to calculate simulations with Comsol 3.5a (Comsol, Burlington, MA). The simple model consisted of a free flow pipette (height of 100 µm, radius of 2 µm) adjacent to a large porous hydrogel (height of 5 mm, radius of 5 mm). A two dimensional axis of symmetry was drawn through the pipette lumen. The steady-state solution was the result of three descriptive modes: “conductive media DC” mode, “Brinkman equation” mode, and “electrokinetic flow application” mode. The conductive media mode solves Equation S2 with appropriate boundary conditions

$$\nabla \cdot (\sigma \nabla V - J^e) = 0 \tag{S2}$$

where V is potential, σ is conductivity and J^e is an externally generated current density. An inward current flow of 50000 A/m^2 was set at the distal end of the pipette. The result is the potential distribution for a given J^e.

We make the following assumptions in the Brinkman equation mode: a low Reynolds number, low flow speed, and small pores. This mode solves the continuity Equation S3 and a momentum balance Equation S4.

$$\nabla \cdot \mathbf{u} = 0 \tag{S3}$$

$$\frac{\rho}{\phi}\frac{\partial \mathbf{u}}{\partial t} + \frac{\eta}{\kappa}\mathbf{u} = \nabla \cdot \left[-p\mathbf{I} + \frac{\eta}{\phi}(\nabla \mathbf{u} + (\nabla \mathbf{u})^T)\right] + \mathbf{F} \tag{S4}$$

where $\mathbf{u}$ is the velocity vector, ρ is the density, porosity is ϕ, t is time, η represents the dynamic viscosity, p is the pressure, the identity matrix is described by $\mathbf{I}$, $(\nabla \mathbf{u})^T$ represents the matrix transpose, $\mathbf{F}$ is the body force vector, and κ is the permeability of the porous medium calculated from the Equation S5.

$$\kappa = \frac{\phi\, m^2}{k_0\, \tau} \tag{S5}$$

In Equation S5, m is the pore radius, k_0 is a factor of the pore shape, and τ is the volumetric tortuosity of the medium. Volumetric tortuosity is related to the physical structure of the porous volume. In order to calculate the electroosmotic flow inside the pipette, the pipette was defined as a moving wall, where velocity was calculated by Equation S6.

$$v_{\mathrm{wall}} = -\frac{\varepsilon \zeta_{\mathrm{wall}}}{\eta} E \tag{S6}$$

The electroosmotic flow in the porous gel was set as a body force calculated by Equation S7

$$\mathbf{F} = -\frac{\varepsilon\, \zeta_{\mathrm{hydrogel}}}{m^2 \tau} E \tag{S7}$$

where ζ_{wall} is the ζ-potential of the pipette wall, $\zeta_{\mathrm{hydrogel}}$ is the ζ-potential of the hydrogel and E is the electric field obtained from conductive media DC mode.

The electrokinetic flow application mode solves the Nernst-Planck equation (S8) with a continuity equation (S9).

$$\frac{\partial \mathrm{C}}{\partial t} + \nabla \cdot \left(-D\, \nabla \mathrm{C} + \mathrm{C}\mu_{ep}\boldsymbol{E} + \mathrm{C}\, \mathbf{u}'\right) = 0 \tag{S8}$$

$$\mathbf{n} \cdot (\mathbf{J}_1 - \mathbf{J}_2) = 0 \tag{S9}$$

Diffusion coefficient of the solute is D, C is the concentration of the solute, and μ_{ep} is the electrophoretic mobility of the solute. The velocity, $\mathbf{u}'$, is equal to the velocity of the solvent obtained from the Brinkman equation divided by the square of the apparent tortuosity of the solute in the gel (obtained from the experiments). The solute mass flux vectors on either side of the hydrogel/solution interface, $\mathbf{J}_1$ and $\mathbf{J}_2$, are defined by Equation S10.

$$\mathbf{J} = -D\, \nabla \mathrm{C} + \mathrm{C}\mu_{ep}\boldsymbol{E} + \mathrm{C}\, \mathbf{u}' \tag{S10}$$

The solute contribution to the solvent velocity is assumed to be negligible in comparison to the solvent's contribution to the solute. Note that the boundary condition at the interface of the pipette and the hydrogel was set as a continuity condition in all three modes. The mesh size was set to a maximum element size scaling factor of 0.3 and narrow regions setting of 5, resulting in 172490 degrees of freedom. The mesh size creates a stable solution without too many elements. The 'parametric segregated' stationary solver was chosen for rapid convergence of the calculation.

We also simulated a more realistic geometry using the same three modes as in the simple simulation with a few exceptions. The more realistic simulation calculated the parameters of a pulled pipette tip in -25 mV ζ-potential hydrogel under 1 μA of current. The pipette was drawn using 24 points measured from a micrograph of a typical pipette. The tip opening was rounded in order to avoid problems with the mesh. The simulated pipette consisted of a 0.5 mm non-tapered section and a 2.5 mm tapered section. The hydrogel was represented by a cylinder with a radius of 10 mm and a height of 13 mm. The pipette, filled with free solution, was placed so that the tip was 3 mm below the top surface of the hydrogel. Hydrogel also filled the tip to a depth of 0.5 μm. We applied the default extra fine mesh with the additions of a maximum element size of 5×10^{-5} in the pipette, a maximum element size of 2×10^{-6} around the tip, and a growth rate of 1.1 around the tip, resulting in 122348 degrees of freedom.

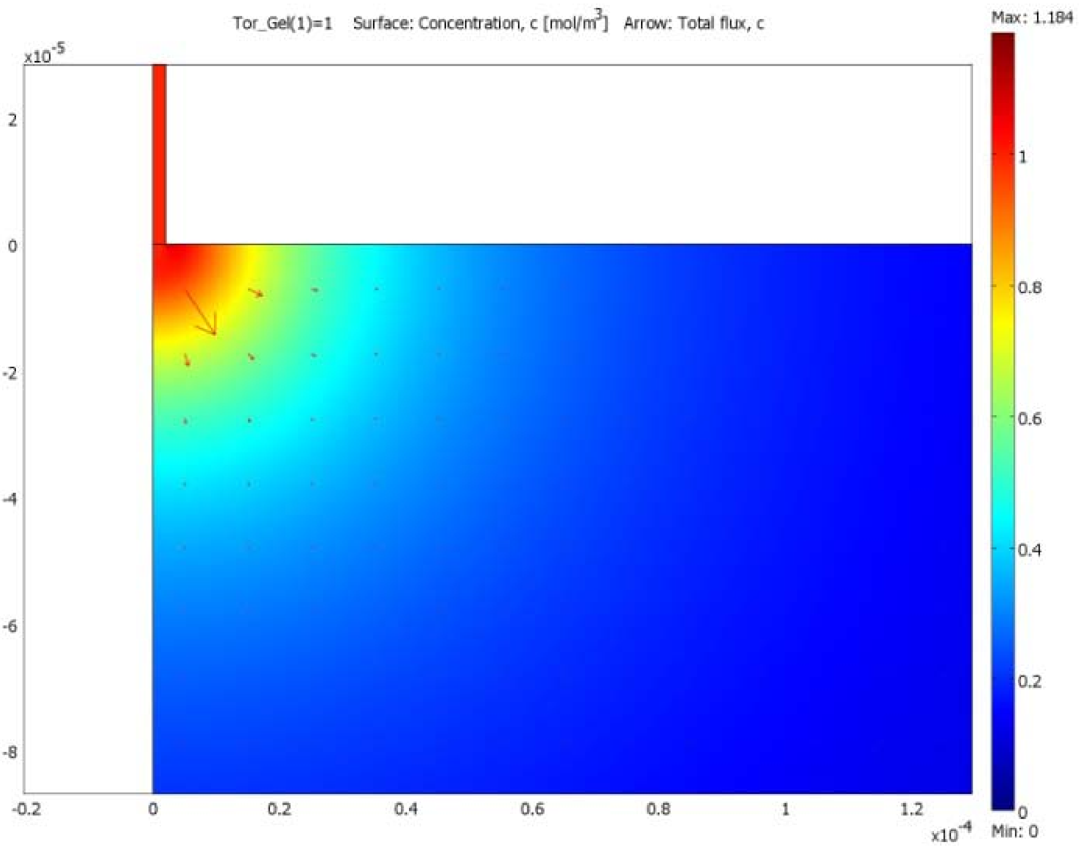

SI Figure 5.2. Comsol Simulation

SI Figure 5.2 shows the result of a simple Comsol simulation of a 2 μm radius pipette (ζ = -25 mV) ejecting a solute into a hydrogel (ζ = -25 mV, λ = 1, pore radius = 200 nm) via an applied current density of 5×10^4 A/m^2 at the distal end of the pipette. Arrows show the direction and magnitude of the solute flux in the hydrogel. The solute has no electrophoretic mobility and a diffusion coefficient of 1×10^{-10} m^2/s. The simulation is pseudo-3-dimensional simulation of the simplified version of our experiment. The concentration profile along the axis of symmetry yields a concentration of approximately 1 at $\rho = 1$ and a Pe_E of 10. Pe_E is determined by fitting Equation 13 to the concentration data along the axis of symmetry outside the tip. By applying the above parameters to Equation 5, the resulting Pe_T is 10. Simplified simulation models such as shown here demonstrate the agreement between Pe_E and Pe_T.

A scaling factor between the two Pe values occurs when there is a difference in the ζ-potentials of the pipette and the hydrogel, as shown in SI Figure 5.3.

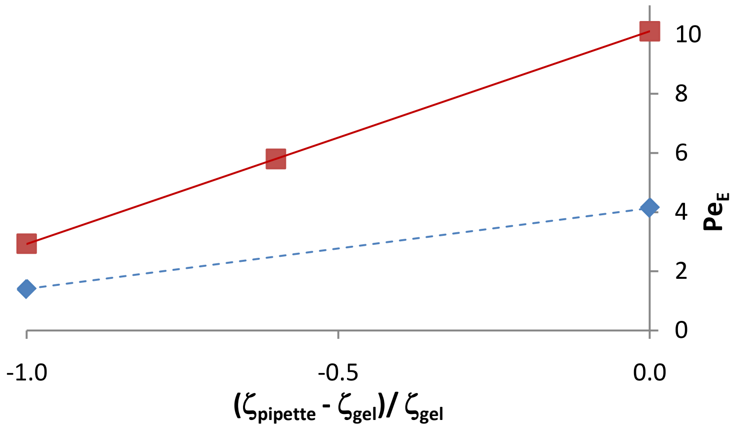

SI Figure 5.3. Effects of mismatched ζ-potentials

SI Figure 5.3 shows the simulated effect of a ζ-potential mismatch at the pipette/ hydrogel interface on Pe_E. The solid red line refers to a -25 mV hydrogel and the dashed blue line refers to a -10 mV hydrogel. The pipette ζ-potential is varied for each line. Tortuosity is 1 in both hydrogels.

SI Figure 5.3 shows Pe_E of a neutral solute as a function of the ζ-potential mismatch:

$$\frac{\zeta_{pipette} - \zeta_{hydrogel}}{\zeta_{pipette}} \tag{S11}$$

In the case where the pipette and hydrogel ζ-potentials match, the ζ-potential mismatch is zero. As the magnitude of the pipette ζ-potential approaches zero, the ζ-potential mismatch approaches -1. The figure shows the relationship between Pe_E of the solute and the ζ-potential mismatch is linear. The slope and intercept depend on the ζ-potential of the hydrogel. The larger slope and intercept result from the larger magnitude ζ-potential (-25 mV) hydrogel. These simplified geometry simulations exhibit increased pressures at the pipette/ hydrogel interface with greater ζ-potential mismatches. In a -25 mV hydrogel, for example, pressures of 32 (-10 mV pipette ζ-potential, mismatch= -0.60) and 47 Pa (0 mV pipette ζ-potential, mismatch= -0.96) are produced at the interface. A -10 mV pipette ζ-potential is approximately that of borosilicate.

However, in a more realistic simulation that accounts for tip tapering, the resulting pressure is 6 Pa. The pressure is proportional to the taper length, defined as the distance between the unpulled pipette diameter and the opening at the tip. Increasing the taper length ultimately increases the pressure. Note that typical iontophoretic pipettes have a taper that is at least five times longer than the ones used in our experiments and that were simulated here.. Thus, typical iontophoretic experiments would likely have greater pressure-induced effects under the condition that all other variables remain the same. This difference in tapering length is a result of the method used to pull the pipette to a tip. The P-2000 capillary puller forms reproducible pipette tips with the use of a laser and a controlled pull velocity. Pressure effects described in the simulation are somewhat inaccurate. The simulations do not account for temperature effects because of the added complexity. The simulations are influenced by temperature.

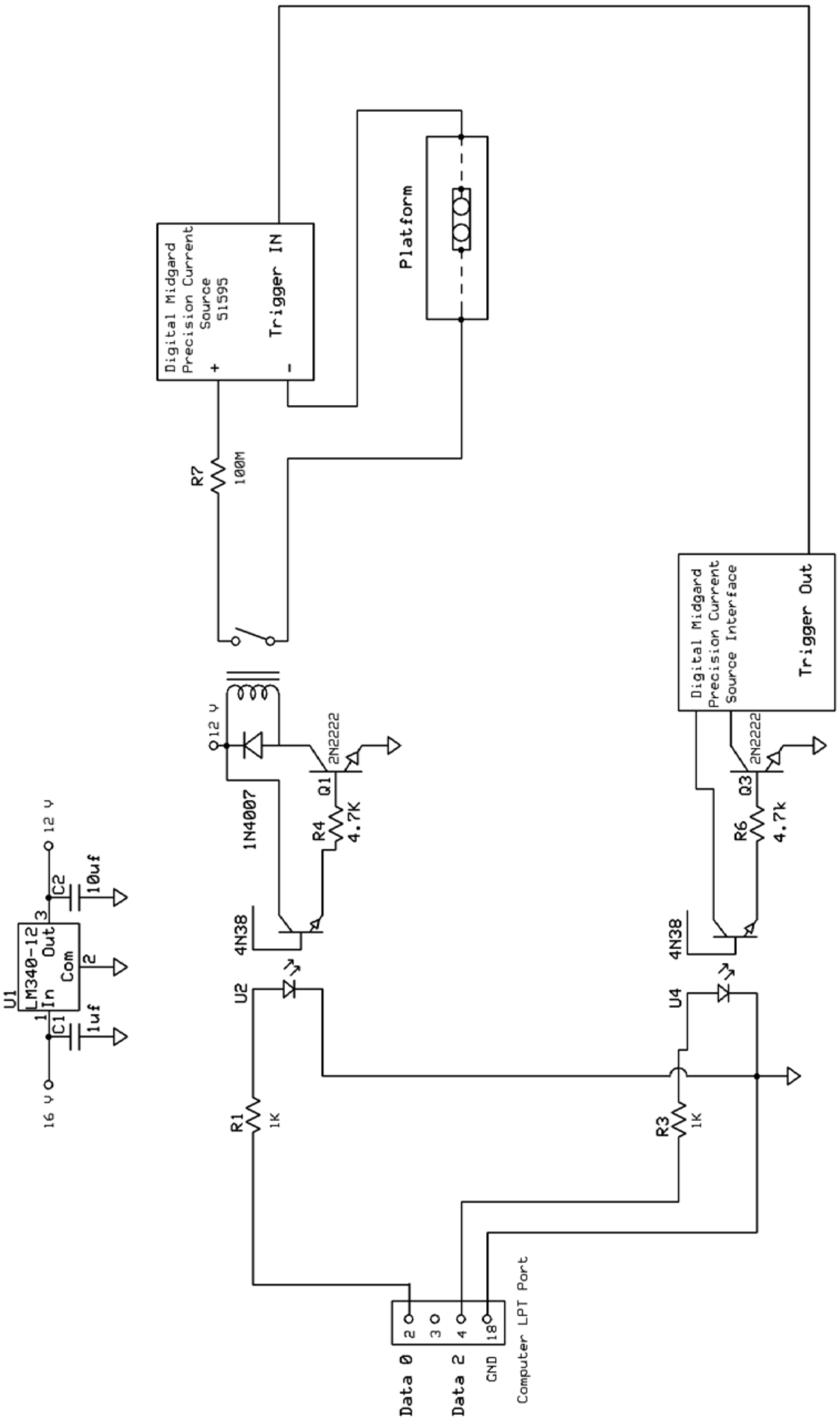

SI Figure 5.4a. Digital Midgard^{TM} experimental circuit

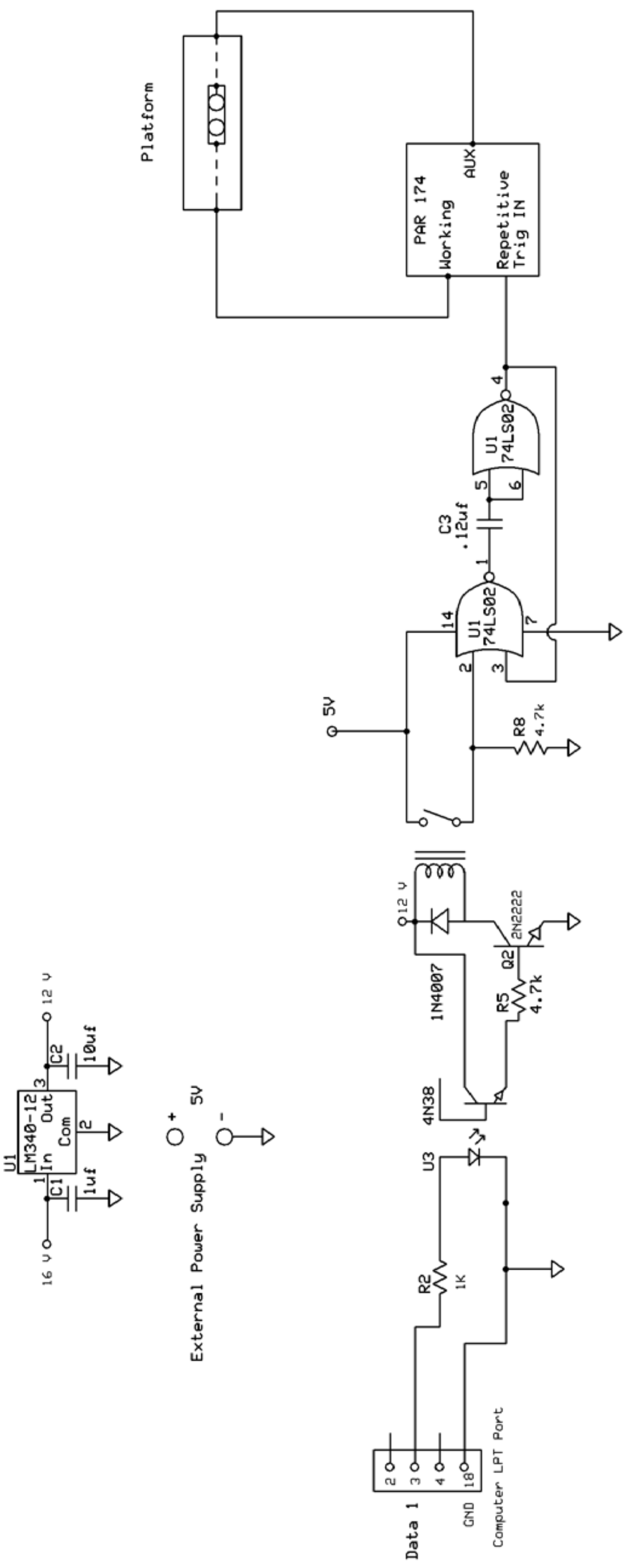

SI Figure 5.4b. PAR experimental circuit

6.0 A SIMPLE METHOD FOR MEASURING ORGANOTYPIC TISSUE SLICE CULTURE THICKNESS

ABSTRACT

This paper presents a simple method to measure tissue slice thicknesses using an ohmmeter. An ohmmeter can detect when a circuit is open or closed. The circuit described here is composed of a metal probe, an ohmmeter, a counter electrode, culture medium or physiological buffer, and tissue. The probe and the electrode are on opposite interfaces of an organotypic hippocampal slice culture. The circuit closes when the metal probe makes contact with the top surface of the tissue. The probe position is recorded and compared to its position when it makes contact with the insert membrane on which the tissue grows, thus yielding a thickness measurement. The method does not reduce the viability of tissue cultures. Thicknesses of the tissue cultures were measured under a number of culturing protocols. An initial drop in thickness occurred between 0 and 4 days in culture. Thicknesses are rather constant thereafter. The type of culture medium and the initial thickness of the tissue explant influence the thickness. The measurement technique described is straightforward and rapid, about one minute per culture.

6.1 INTRODUCTION

Brain tissue slices and slice cultures are frequently used for neuropharmocological and neurophysiological studies [214]. Acute and cultured tissue slices provide easy access for experimental manipulation while maintaining *in vivo* morphology and electrophysiology [152]. Freshly excised tissue is sliced to a desired thickness using either a tissue chopper or a vibratome and is used for experiments immediately, or cultured and used later. The thickness of the tissue slice is essential to its characterization. The overall health [18], the approach to making certain measurements [93, 215-217], and diffusion distances [214, 216, 218-222] are directly correlated to tissue thickness, and are pertinent to neurological experiments. This paper presents a simple, direct, and cost-effective method for measuring thicknesses of tissue slice cultures without causing cell death.

Methods exist for measuring slice thickness; however, those methods involve either sacrificing the tissue,[84, 223] or submerging the tissue in solution[219]. In the first case, the tissue is cut perpendicular to the long axis of the tissue and the thickness is measured optically. In the second case, double-barreled ion-selective microelectrodes measure steep changes in ion concentration gradients once in contact with the tissue [219]. In the latter procedure, the acutely prepared hippocampal tissue slice is in a bath. The microelectrode detects ion concentration gradients which change significantly at the bath-tissue interface due to the difference between the non-tortuous bath and tortuous tissue. Although a useful technique, translating this technique to slices cultured using the interface method would be cumbersome. In the interface environment, oxygen is supplied from the air above the tissue culture and nutrients are supplied from below.[84] Submerging tissue cultures may therefore cause hypoxia if the medium is not oxygenated. There is therefore a need for a simple and safe method for determining the thickness of tissue cultured by the interface method.

This paper describes experiments using organotypic hippocampal slice cultures that are commonly used for neurological studies.[152, 214, 224] The hippocampal laminar architecture is preserved, while the biochemistry, synaptic connections, and electrophysiology are similar to those *in vivo*.[214] Organotypic cultures survive from weeks to months, providing options for long term studies, such as those studying recovery following excitotoxicity, ischemia, and traumatic injury.[224] Recently, we have developed a technique to acquire samples of extracellular fluid from these tissue cultures based on electroosmotic flow.[93, 215] In this or any other approach to obtain information on the concentrations and distribution of freely diffusing solutes, knowledge of the culture's thickness is essential.

6.2 MATERIALS AND METHODS

6.2.1 Chemicals and solutions

Two types of culture media were employed: medium A and medium B. Medium A[78] consisted of the following obtained from Sigma-Aldrich: 50% basal medium eagle, 25% Earle's balanced salt solution, 23% heat inactivated horse serum, 25 U/mL penicillin-streptomycin, 1 mM L-glutamine, and 41.6 mM D-(+)-glucose. Medium B [225] was composed of the following materials obtained from Gibco (Invitrogen, Carlsbad, CA): 50% opti-MEM, 25% horse serum, and 25% Hanks' balanced salt solution with phenol red, and 1% D-(+)-glucose (from Sigma-Aldrich, St. Louis, MO). Medium B was filtered through a Nalgene 0.1 μm polyethersulfone filter (Fisher

Scientific, Waltham, MA). The two culture media were refrigerated until use, at which point they were warmed to 37 °C. The following were also purchased from Sigma-Aldrich unless stated otherwise. Gey's balanced salt solution (GBSS) was supplemented with D-(+)-glucose (27.5 mM) and $MgSO_4$ (2.7 mM, filtered). GBSS was refrigerated until use. HEPES buffered salt solution (HBSS) contained (mM) 143.4 NaCl, 5.0 HEPES, 5.4 KCl, 1.2 $MgSO_4$, 1.2 NaH_2PO_4, 2.0 $CaCl_2$, and 10 D-(+)-glucose diluted with Millipore Synthesis A10 system 18 MΩ purified water (Millipore, Billerica, MA). The pH was adjusted to 7.40 using 0.5 mM NaOH solution prior to filtration through a 0.45 μm nylon Whatman filter (Maidstone, England). HBSS was frozen until use, at which point it was warmed to 37 °C. Propidium iodide (PI) solution was prepared at a final concentration of 0.35 mM in GBSS and frozen until use. 3% agarose type-V (Sigma-Aldrich) in Hanks' balanced salt solution with phenol red was used for method validation.

6.2.2 Tissue culturing procedure

Organotypic hippocampal slice cultures were prepared as described previously.[78] The University of Pittsburgh IACUC authorized the following procedures. Hippocampi were excised from seven-day postnatal Sprague-Dawley albino rats. The tissue was cut into slices (at different thicknesses, as indicated) using a McIlwain tissue chopper (The Mickle Laboratory Engineering, Surrey, England). Tissue slices were laid on a porous Millicell insert membrane (Millipore, Billerica, MA) and incubated at 37 °C in 95% air/5% CO_2 over either medium A or B for up to 14 days in culture. Medium was exchanged twice per week.

6.2.3 Tissue thickness measurements

An insert containing one or two tissue slices was placed over culture medium on an inverted microscope (Olympus IX-71, Melville, NY) in order to monitor visually the procedure under bright field. The inset of Figure 6.1 shows the measurement setup. A 1 mm diameter platinum wire was submerged in the culture medium and connected to a multimeter (Fluka, Everett, WA) to monitor resistance. The other terminal of the multimeter was connected to a 1 mm diameter stainless steel rod. One end of the rod was polished to create a flat surface. The rod was lowered using an electronic micromanipulator (MP-285, with ROE-200 controller and MPC-200, Sutter, Novato, CA) until its polished end made contact with either the insert membrane or the tissue. Contact was indicated by the multimeter reading changing from “open circuit”, to less than 16 MΩ, indicating a completed circuit. Contact and rod location were visually confirmed using the microscope. At the point of contact, the resistance and manipulator position were recorded. Reproducibility of the micromanipulator was tested by recording the position after making contact with the fluid bath, and repeating eight times. For all tissue measurements, the probe was centered primarily on cell bodies of the trisynaptic loop or on apical dendrites of the pyramidal cells, near the pyramidal cell layer. Each tissue culture thickness was calculated from the difference in the averages of four readings from the surface of the insert membrane readings and four tissue readings. With one exception, thicknesses of ten or eleven tissue cultures were measured and averaged for each day in culture. Twenty-five cultures were measured for day zero in medium A. All day zero tissue culture thicknesses were measured 30 minutes to 2 hours following explantation. Errors reported in Figure 6.1 are the standard error of the mean, SEM, for each day in culture. Standard deviations reported in Table 5.1 are the standard deviations of the measured values at each condition.

To compare the proposed method to a known method of measuring thickness, 5 (400 μm initial slice thickness) and 3 (350 μm initial slice thickness) were cultured for 5 days. On day 5 in culture, each of the tissue culture thicknesses was measured using the probe. The 8 tissues were divided into 3 groups. The first group of tissue cultures (N = 3 tissue cultures) was separated from any excess membrane using an X-Acto knife, and the tissue cultures were sliced to 600 μm thick along the same axis as CA1 axons using the tissue chopper. Each tissue culture yielded approximately 4 slices that contained at least one of the following regions: dentate gyrus, CA1-CA4, or the subiculum. The slices were set on a coverslip along the freshly sliced edge and imaged over the IX-71 microscope under bright field using an Olympus U Plan Apo 4× objective lens. The second group of tissue cultures (N = 3 tissue cultures) were fixed using 4 % paraformaldehyde in PBS (Boston Bioproducts, Ashland, MA) for 1 hour, after which the tissue cultures were sliced and imaged as in the first group. Tissue cultures in the third group (N = 2 tissue cultures) were sliced, then fixed in paraformaldehyde and imaged. Each image yielded 3 to 8 thickness measurement and measurements of the insert membrane thickness. The thickness measurements of all the sections of the same tissue culture were averaged and compared to the measured thickness of the same tissue culture using the probe method.

6.2.4 Viability measurements

Thirty tissue cultures were selected at random to check if the process of measuring tissue thickness compromised viability. Following the thickness measurements, medium was exchanged with fresh 37 °C medium supplemented with PI solution, to a final PI concentration of 7 μM. Following a 24 hour incubation period, the medium was exchanged with 37 °C GBSS and incubated for 30 minutes. The GBSS was exchanged and incubated again for a second 30 minute interval. A final exchange to 37 °C HBSS and incubation for 30 minutes preceded imaging analysis. Negative control tissues followed the same exchange procedure. The negative control tissues remained in the incubator following exchanges. To serve as a set of positive controls, a drop of methanol was placed on top of tissue cultures prior to PI exposure. Methanol ensures cell death of both glia and neurons throughout the tissue culture.[215] PI fluorescence indicating cell death was imaged using a U-MGIW2 cube (Olympus) and Simple PCI software (Compix, Cranberry, PA). Exposure times were set according to the fluorescence intensity of the positive controls. Analysis of tissue culture images were done with Simple PCI. Average intensities of regions of interest encompassing the laminar structure of the tissue cultures were collected and analyzed using Equation 1.[215] The intensity results for all the controls were averaged within their given treatments, resulting in an average PI intensity for the specific day in culture.

$$\%\ \text{Cell Death} = \frac{\text{PI intensity (experimental)-Average PI intensity (negative control)}}{\text{Average PI intensity (positive control)- Average PI intenstiy (negative control)}} \times 100\% \qquad (1)$$

6.2.5 Method validation

Agarose gel (3% w/v) was cut to approximately 3.5 mm thick slab. The gel was laid on its end on a coverslip over the microscope and was imaged in bright field. Several thickness measurements were made at different points along the length of the slab. The procedure was repeated for the same gel slab on the opposite face. The gel was then laid on an insert membrane over HBSS, like the tissue setup. The thickness of the slab was measured by averaging manipulator readings from 4 points of contact with the steel rod, and subtracting from the readings of 4 points of contact with the membrane. Once complete, two sides of the slab were again imaged and measured using Simple PCI software on a coverslip.

6.3 RESULTS

6.3.1 Tissue culture thickness

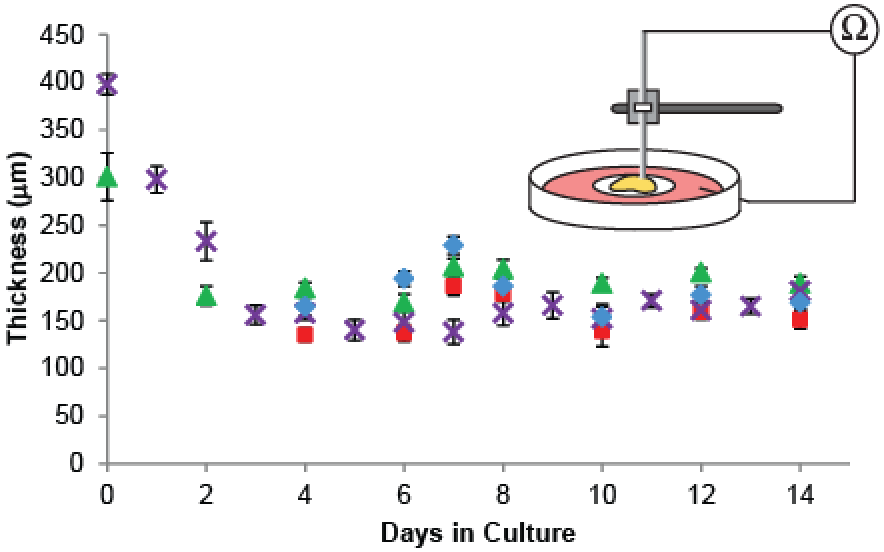

Figure 6.1. Measured thicknesses over time

Points show the average thicknesses on the specified days in culture and the standard errors of the mean. Purple exes represent medium A tissues with an initial slice thickness of 500 μm. Red squares represent medium B and 300 μm initial slice thickness. The blue diamonds represent medium B and 400 μm. The green triangles represent medium B and 500 μm. Inset: The setup of the measurement circuit.

Table 6.1. Values corresponding to Figure 6.1

Medium A

Slice Thickness (μm)	Day	Average Thickness (μm)	SEM (μm)	n	Standard Deviation (μm)
500	0	398	11	25	56
500	1	298	14	10	45
500	2	233	20	10	63
500	3	156	10	10	32
500	4	158	7	10	22
500	5	140	11	10	35
500	6	148	15	10	47
500	7	138	13	10	40
500	8	158	13	10	41
500	9	166	14	10	44
500	10	152	15	10	46
500	11	171	7	10	22
500	12	161	9	10	27
500	13	165	8	10	24
500	14	181	8	10	25
Medium B					
300	4	135	7	10	22
300	6	137	9	10	30
300	7	186	9	10	27
300	8	178	8	10	25
300	10	139	16	10	52
300	12	159	7	10	23
300	14	151	10	10	30
400	4	165	9	10	30
400	6	194	8	11	28
400	7	229	9	10	29
400	8	186	8	10	24
400	10	154	11	10	34
400	12	177	9	10	28
400	14	169	7	10	22
500	0	301	25	10	78
500	2	176	10	10	31
500	4	184	6	10	20
500	6	169	9	10	27
500	7	207	8	11	25
500	8	204	10	10	31
500	10	189	6	10	18
500	12	201	4	10	13
500	14	189	7	11	23

The proposed method measured tissue culture thicknesses to be 40 ± 9 μm (N = 8) more thick than when the same tissue cultures were sacrificed and measured in bright field images. Figure 6.1 shows the average thicknesses of tissue cultures for three different initial slice thicknesses (set by the tissue chopper) and two different culture media. See Table 6.1 for a table list of values corresponding to Figure 6.1. Day 0 tissue culture thicknesses were measured 30 minutes to 2 hours following explantation. Tissues cultured in medium A were measured every day in culture from day 0, directly after tissue extraction, until day 14. The other points represent tissues cultured in medium B with different initial slice thicknesses. Tissue culture thickness levels off between days 4 and 14, during which time the average tissue thickness is 158 ± 3 μm for medium A with an initial slice thickness of 500 μm. Medium B produces average tissue thicknesses for days 4 – 14 in culture of 155 ± 4, 182 ± 4, and 192 ± 3 μm, with initial slice thicknesses of 300, 400, and 500 μm, respectively. The two different culture media result in statistically different tissue culture thicknesses over this time period, with $p < 0.0001$. Single-factor ANOVA of 500 μm initial slice thickness cultured over either medium shows that there is a slight dependence of thickness on the day in culture. Single-factor ANOVA shows that initial slice thickness affects medium B tissue culture thickness ($p < 3 \times 10^{-10}$).

On a given day in culture, thicknesses can vary as evidenced by the standard deviations in Table 6.1. Thicknesses of tissues cultured in medium B are less variable than thicknesses of slices cultured in medium A. For example, for a slice thickness 500 μm on day 6 in culture (n = 10), the SEM in tissue thickness for medium B, 5 % of the mean, is smaller than those cultured in medium A, 10 % of the mean. Positioning of the micromanipulator includes a 14 μm standard deviation (n = 8).

6.3.2 Viabilty

An average of 3.9 ± 1.2 % cell death is incurred in the tissue cultures as a result of thickness measurements as compared to negative and positive controls.

6.3.3 Method validation

Images of the gel slab taken before probe thickness measurements resulted in a thickness of 3.44 ± 0.03 mm. The slab thickness measured using the proposed probe technique was 3.51 ± 0.05 mm. The thickness measurement of the slab using image analysis following the probe measurements was 3.52 ± 0.02 mm.

6.4 DISCUSSION

Current methods available for measuring OHSC thickness have significant drawbacks. Most OHSC users chop the OHSC perpendicularly to the insert membrane in order to image and optically measure the thickness. When we made an attempt using this method in our laboratory, we found it to be unreliable. The tissue cultures were consistently measured thinner once chopped compared to when measured with the probe. The primary concern relates to “pinching” of the OHSC along the chopped edges. Furthermore, manipulation of the chopped OHSCs is challenging. The chopped OHSC has a tendency to dry out or not lay perfectly perpendicular to the coverslip. As stated earlier, the use of ion-selective microelectrodes is cumbersome, and therefore was not used as a method of validation. The use of a 3% gel slab allows for optical measurements without risking dehydration of the gel. In order to position the slab on its end for optical measurements, the gel thickness must be large enough to stand on its side. Gel slabs of similar thickness to OHSCs tend to fall over during optical measurements. In addition, the gel composition consists of Hanks' balanced salt solution, such that the multimeter responds when the stainless steel probe contacts the surface of the gel. Optical thickness measurements confirmed thickness measurements made with the stainless steel probe, thus validating the proposed method of thickness measurements. Some error in the measurements is due to the 14 μm standard deviation of the manipulator positioning.

Figure 6.1 shows a significant loss of thickness within the first few days. Measurements taken within a couple of hours following explantation show that the tissue thickness is 20% (medium B) to 30% (medium A) less than the chopper setting. There is no observable dependence of tissue culture thickness on time within the 30 minutes to 2 hour time-span following explantation. These results show thinning occurring on a shorter timescale compared to Stoppini's original estimation of one week..[84] The two media produce slightly different tissue thicknesses once the tissue thicknesses level off. The different thicknesses may arise from differences in glial cell proliferation.[158, 226] Visual inspection confirms a small extension of glia that line the edges of the tissue cultures[84] in medium B compared to medium A.

The standard deviations in Table 6.1 show variation in thicknesses among tissue cultures. Variations among the tissue cultures could be due to varying cell differentiation rates and glial cell proliferation,[152] since there is a dependence on the medium. Once in culture, reactive astrocytic glia blanket the surface of the sectioned tissue.[224, 226] Other factors affecting tissue thickness are related to surgery and incubation. Some of those factors are variations in time spent outside of the culture environment and degree of oxygenation.

Measuring tissue thickness is effective for screening and characterizing brain tissue cultures prior to use in experiments. Brain tissue slices or cultures that are of thicknesses other than expected are likely unhealthy tissues.[18] The technique can be useful in real time measurements of tissue swelling under various stress conditions, as opposed to final characterization methods requiring sacrifice of the tissue culture.[84, 223] Characterizing tissue cultures prior to experiments also allows for proper placement of sampling and measurement probes and capillaries.[93, 215] Furthermore, sampling analytes from the extracellular space is affected by tissue thickness.[93, 215, 216, 221] Variations in thicknesses among the tissue cultures strengthen the argument that tissue culture thickness should be measured.

The method proposed in this paper is easy, effective, expeditious, and inexpensive. It causes negligible cell death, and does not require the tissue cultures to be submerged in a bath. Furthermore, none of the components are fragile. This simple technique may be applied for characterization and screening of any tissue slice or culture that is not submerged in solution.

REFERENCES

1. Savtchenko LP, Kulahin N, Korogod SM, Rusakov DA. Electric fields of synaptic currents could influence diffusion of charged neurotransmitter molecules. *Synapse.* 2004;51(4):270-278.

2. Anastassiou CA, Montgomery SM, Barahona M, Buzsaki G, Koch C. The effect of spatially inhomogeneous extracellular electric fields on neurons. *Journal of Neuroscience.* 2010;30(5):1925-1936.

3. Jefferys JG. Nonsynaptic modulation of neuronal activity in the brain: electric currents and extracellular ions. *Physiological Reviews.* 1995;75(4):689-723.

4. Perlmutter JS, Mink JW. Deep brain stimulation. *Annual Review of Neuroscience.* 2006;29:229-257.

5. Kim EJ, Kim WR, Chi SE, et al. Repetitive transcranial magnetic stimulation protects hippocampal plasticity in an animal model of depression. *Neuroscience Letters.* 2006;405(1-2):79-83. Epub 2006 Jul 2012.

6. Kuroda Y, Motohashi N, Ito H, et al. Effects of repetitive transcranial magnetic stimulation on [11C]raclopride binding and cognitive function in patients with depression. *Journal of Affective Disorders.* 2006;95(1-3):35-42. Epub 2006 Jun 2015.

7. Lisanby SH, Belmaker RH. Animal models of the mechanisms of action of repetitive transcranial magnetic stimulation (RTMS): comparisons with electroconvulsive shock (ECS). *Depression and Anxiety.* 2000;12(3):178-187.

8. Wagner T, Gangitano M, Romero R, et al. Intracranial measurement of current densities induced by transcranial magnetic stimulation in the human brain. *Neuroscience Letters.* 2004;354(2):91-94.

9. Ozen S, Sirota A, Belluscio MA, et al. Transcranial electric stimulation entrains cortical neuronal populations in rats. *Journal of Neuroscience.* 2010;30(34):11476-11485.

10. Ardolino G, Bossi B, Barbieri S, Priori A. Non-synaptic mechanisms underlie the after-effects of cathodal transcutaneous direct current stimulation of the human brain. *Journal of Physiology.* 2005;568(Pt 2):653-663. Epub 2005 Jul 2021.

11. Fregni F, Boggio PS, Nitsche MA, Rigonatti SP, Pascual-Leone A. Cognitive effects of repeated sessions of transcranial direct current stimulation in patients with depression. *Depression and Anxiety.* 2006;23(8):482-484.

12. Juckel G, Mendlin A, Jacobs BL. Electrical stimulation of rat medial prefrontal cortex enhances forebrain serotonin output: implications for electroconvulsive therapy and transcranial magnetic stimulation in depression. *Neuropsychopharmacology.* 1999;21(3):391-398.

13. Weinstein S. The anticonvulsant effect of electrical fields. *Current Neurology and Neuroscience Reports.* 2001;1(2):155-161.

14. Garcia PA, Rossmeisl JH, Jr., Neal RE, 2nd, et al. Intracranial nonthermal irreversible electroporation: in vivo analysis. *The Journal of Membrane Biology.* 2010;236(1):127-136.

15. Akaneya Y, Jiang B, Tsumoto T. RNAi-induced gene silencing by local electroporation in targeting brain region. *Journal of Neurophysiology*. 2005;93(1):594-602.

16. McQuiston AR. Cholinergic modulation of excitatory synaptic input integration in hippocampal CA1. *The Journal of Physiology*. 2010;588(Pt 19):3727-3742.

17. McCaig CD, Sangster L, Stewart R. Neurotrophins enhance electric field-directed growth cone guidance and directed nerve branching. *Dev. Dyn.* 2000;217(3):299-308.

18. Sykova E, Nicholson C. Diffusion in brain extracellular space. *Physiological Reviews.* 2008;88(4):1277-1340.

19. Cheer JF, Aragona BJ, Heien ML, Seipel AT, Carelli RM, Wightman RM. Coordinated accumbal dopamine release and neural activity drive goal-directed behavior. *Neuron.* 2007;54(2):237-244.

20. Kiyatkin EA, Brown PL. I.v. cocaine induces rapid, transient excitation of striatal neurons via its action on peripheral neural elements: single-cell, iontophoretic study in awake and anesthetized rats. *Neuroscience.* 2007;148(4):978-995. Epub 2007 Jul 2017.

21. Lerner EN, van Zanten EH, Stewart GR. Enhanced delivery of octreotide to the brain via transnasal iontophoretic administration. *Journal of Drug Targeting.* 2004;12(5):273-280.

22. Probstein RF. *Physicochemical Hydrodynamics, An Introduction: Second Edition*; 1994.

23. Delgado AV, Gonzalez-Caballero F, Hunter RJ, Koopal LK, Lyklema J. Measurement and interpretation of electrokinetic phenomena. *Journal of Colloid and Interface Science.* 2007;309(2):194-224. Epub 2007 Mar 2021.

24. Miyake M, Kurihara K. Resting potential of the mouse neuroblastoma cells. II. Significant contribution of the surface potential to the resting potential of the cells under physiological conditions. *Biochimica et Biophysica Acta.* 1983;762(2):256-264.

25. Viskari PJ, Landers JP. Unconventional detection methods for microfluidic devices. *Electrophoresis.* 2006;27(9):1797-1810.

26. Brewer GJ. Exocytosis and directed movement of cytoplasmic vesicles toward the plasma membrane. *Journal of Theoretical Biology.* 1980;85(1):75-82.

27. Stoilova S, Kancheva M. Microelectrophoretic properties of rat brain membrane structures - synaptosomes. *Studia Biophysica.* 1986;113(1-2):27-30.

28. Chammas P, Federspiel WJ, Eisenberg SR. A Microcontinuum Model of Electrokinetic Coupling in the Extracellular Matrix: Perturbation Formulation and Solution. *Journal of Colloid and Interface Science.* 1994;168(2):526-538.

29. Bath BD, Lee RD, White HS, Scott ER. Imaging Molecular Transport in Porous Membranes. Observation and Analysis of Electroosmotic Flow in Individual Pores Using the Scanning Electrochemical Microscope. *Analytical Chemistry.* 1998;70(6):1047-1058.

30. Uitto OD, White HS. Electroosmotic pore transport in human skin. *Pharmaceutical Research.* 2003;20(4):646-652.

31. Ranck JB, Jr. Synaptic "Learning" Due to Electroosmosis: a Theory. *Science.* 1964;144:187-189.

32. Anderova M, Kubinova S, Mazel T, et al. Effect of elevated K(+), hypotonic stress, and cortical spreading depression on astrocyte swelling in GFAP-deficient mice. *Glia.* 2001;35(3):189-203.

33. Cragg SJ, Nicholson C, Kume-Kick J, Tao L, Rice ME. Dopamine-mediated volume transmission in midbrain is regulated by distinct extracellular geometry and uptake. *Journal of Neurophysiology.* 2001;85(4):1761-1771.

34. Cserr HF, DePasquale M, Nicholson C, Patlak CS, Pettigrew KD, Rice ME. Extracellular volume decreases while cell volume is maintained by ion uptake in rat brain during acute hypernatremia. *Journal of Physiology.* 1991;442:277-295.

35. Homola A, Zoremba N, Slais K, Kuhlen R, Sykova E. Changes in diffusion parameters, energy-related metabolites and glutamate in the rat cortex after transient hypoxia/ischemia. *Neuroscience Letters.* 2006;404(1-2):137-142. Epub 2006 Jun 2006.

36. Hrabetova S. Extracellular diffusion is fast and isotropic in the stratum radiatum of hippocampal CA1 region in rat brain slices. *Hippocampus.* 2005;15(4):441-450.

37. Hrabetova S, Nicholson C. Dextran decreases extracellular tortuosity in thick-slice ischemia model. *Journal of Cerebral Blood Flow Metabolism.* 2000;20(9):1306-1310.

38. Krizaj D, Rice ME, Wardle RA, Nicholson C. Water compartmentalization and extracellular tortuosity after osmotic changes in cerebellum of Trachemys scripta. *Journal of Physiology.* 1996;492(Pt 3):887-896.

39. Kume-Kick J, Mazel T, Vorisek I, Hrabetova S, Tao L, Nicholson C. Independence of extracellular tortuosity and volume fraction during osmotic challenge in rat neocortex. *Journal of Physiology.* 2002;542(Pt 2):515-527.

40. Lehmenkuhler A, Sykova E, Svoboda J, Zilles K, Nicholson C. Extracellular space parameters in the rat neocortex and subcortical white matter during postnatal development determined by diffusion analysis. *Neuroscience.* 1993;55(2):339-351.

41. Mazel T, Richter F, Vargova L, Sykova E. Changes in extracellular space volume and geometry induced by cortical spreading depression in immature and adult rats. *Physiological Research.* 2002;51(Suppl 1):S85-93.

42. Mazel T, Simonova Z, Sykova E. Diffusion heterogeneity and anisotropy in rat hippocampus. *Neuroreport.* 1998;9(7):1299-1304.

43. McBain CJ, Traynelis SF, Dingledine R. Regional variation of extracellular space in the hippocampus. *Science.* 1990;249(4969):674-677.

44. Nicholson C, Phillips JM. Ion diffusion modified by tortuosity and volume fraction in the extracellular microenvironment of the rat cerebellum. *Journal of Physiology.* 1981;321:225-257.

45. Perez-Pinzon MA, Tao L, Nicholson C. Extracellular potassium, volume fraction, and tortuosity in rat hippocampal CA1, CA3, and cortical slices during ischemia. *Journal of Neurophysiology.* 1995;74(2):565-573.

46. Piet R, Vargova L, Sykova E, Poulain DA, Oliet SH. Physiological contribution of the astrocytic environment of neurons to intersynaptic crosstalk. *Proceedings of the National Academy of Sciences of the United States of America.* 2004;101(7):2151-2155. Epub 2004 Feb 2156.

47. Rice ME, Okada YC, Nicholson C. Anisotropic and heterogeneous diffusion in the turtle cerebellum: implications for volume transmission. *Journal of Neurophysiology.* 1993;70(5):2035-2044.

48. Slais K, Vorisek I, Zoremba N, Homola A, Dmytrenko L, Sykova E. Brain metabolism and diffusion in the rat cerebral cortex during pilocarpine-induced status epilepticus. *Experimental Neurology.* 2008;209(1):145-154. Epub 2007 Sep 2020.

49. Sykova E, Fiala J, Antonova T, Vorisek I. Extracellular space volume changes and diffusion barriers in rats with kaolin-induced and inherited hydrocephalus. *European Journal of Pediatric Surgery.* 2001;11(Suppl 1):S34-37.

50. Sykova E, Mazel T, Hasenohrl RU, et al. Learning deficits in aged rats related to decrease in extracellular volume and loss of diffusion anisotropy in hippocampus. *Hippocampus.* 2002;12(2):269-279.

51. Sykova E, Mazel T, Simonova Z. Diffusion constraints and neuron-glia interaction during aging. *Experimental Gerontology.* 1998;33(7-8):837-851.

52. Sykova E, Vorisek I, Antonova T, et al. Changes in extracellular space size and geometry in APP23 transgenic mice: a model of Alzheimer's disease. *Proceedings of the National Academy of Sciences of the United States of America.* 2005;102(2):479-484. Epub 2005 Jan 2003.

53. Sykova E, Vorisek I, Mazel T, Antonova T, Schachner M. Reduced extracellular space in the brain of tenascin-R- and HNK-1-sulphotransferase deficient mice. *European Journal of Neuroscience.* 2005;22(8):1873-1880.

54. van der Toorn A, Sykova E, Dijkhuizen RM, et al. Dynamic changes in water ADC, energy metabolism, extracellular space volume, and tortuosity in neonatal rat brain during global ischemia. *Magnetic Resonance in Medicine.* 1996;36(1):52-60.

55. Vargova L, Homola A, Zamecnik J, Tichy M, Benes V, Sykova E. Diffusion parameters of the extracellular space in human gliomas. *Glia.* 2003;42(1):77-88.

56. Vorisek I, Sykova E. Ischemia-induced changes in the extracellular space diffusion parameters, K+, and pH in the developing rat cortex and corpus callosum. *Journal of Cerebral Blood Flow Metabolism.* 1997;17(2):191-203.

57. Vorisek I, Sykova E. Evolution of anisotropic diffusion in the developing rat corpus callosum. *Journal of Neurophysiology.* 1997;78(2):912-919.

58. Zoremba N, Homola A, Rossaint R, Sykova E. Brain metabolism and extracellular space diffusion parameters during and after transient global hypoxia in the rat cortex. *Experimental Neurology*. 2007;203(1):34-41. Epub 2006 Sep 2007.

59. Nicholson C, Tao L. Hindered diffusion of high molecular weight compounds in brain extracellular microenvironment measured with integrative optical imaging. *Biophysical Journal.* 1993;65(6):2277-2290.

60. Tao L, Nicholson C. Diffusion of albumins in rat cortical slices and relevance to volume transmission. *Neuroscience.* 1996;75(3):839-847.

61. Thorne RG, Nicholson C. In vivo diffusion analysis with quantum dots and dextrans predicts the width of brain extracellular space. *Proceedings of the National Academy of Sciences of the United States of America.* 2006;103(14):5567-5572. Epub 2006 Mar 5527.

62. Xiao F, Nicholson C, Hrabe J, Hrabetova S. Diffusion of flexible random-coil dextran polymers measured in anisotropic brain extracellular space by integrative optical imaging. *Biophysical Journal.* 2008;95(3):1382-1392. Epub 2008 May 1382.

63. Prokopova-Kubinova S, Vargova L, Tao L, et al. Poly[N-(2-hydroxypropyl) methacrylamide] polymers diffuse in brain extracellular space with same tortuosity as small molecules. *Biophysical Journal.* 2001;80(1):542-548.

64. Stroh M, Zipfel WR, Williams RM, Ma SC, Webb WW, Saltzman WM. Multiphoton microscopy guides neurotrophin modification with poly(ethylene glycol) to enhance interstitial diffusion. *Nature Materials.* 2004;3(7):489-494.

65. Thorne RG, Hrabetova S, Nicholson C. Diffusion measurements for drug design. *Nature Materials.* 2005;4(10):713-713.

66. Fenstermacher J, Kaye T. Drug "Diffusion" within the Brain. *Annals of the New York Academy of Sciences.* 1988;531(1):29-39.

67. Fenstermacher JD, Patlak CS, Blasberg RG. Transport of material between brain extracellular fluid, brain cells and blood. *Federation Proceedings.* 1974;33(9):2070-2074.

68. Patlak CS, Fenstermacher JD. Measurements of dog blood-brain transfer constants by ventriculocisternal perfusion. *American Journal of Physiology.* 1975;229(4):877-884.

69. Rosenberg GA, Kyner WT, Estrada E. Bulk flow of brain interstitial fluid under normal and hyperosmolar conditions. *The American Journal of Physiology.* 1980;238(1):F42-49.

70. Kohling R, Lehmenkukhler A, Nicholson C, Speckmann EJ. Superfusion of verapamil on the cerebral cortex does not suppress epileptic discharges due to restricted diffusion (rats, in vivo). *Brain Research.* 1993;626(1-2):149-155.

71. Lehmenkuhler A, Kersting U, Nicholson C. Diffusion of penicillin in agar and cerebral cortex of the rat. *Brain Research.* 1988;444(1):181-183.

72. Lucke A, Lehmenkuhler A, Altrup U, et al. Diffusion analysis of valproate and trans-2-en-valproate in agar and in cerebral cortex of the rat. *Brain Research.* 1993;631(2):187-190.

73. Nicholson C, Rice ME. Calcium diffusion in the brain cell microenvironment. *Canadian Journal of Physiology and Pharmacology.* 1987;65(5):1086-1091.

74. Schwindt W, Nicholson C, Lehmenkuhler A. Critical volume of rat cortex and extracellular threshold concentration for a pentylenetetrazol-induced epileptic focus. *Brain Research.* 1997;753(1):86-97.

75. Thorne RG, Lakkaraju A, Rodriguez-Boulan E, Nicholson C. In vivo diffusion of lactoferrin in brain extracellular space is regulated by interactions with heparan sulfate.

Proceedings of the National Academy of Sciences of the United States of America. 2008;105(24):8416-8421. Epub 2008 Jun 8419.

76. Barrande M, Bouchet R, Denoyel R. Tortuosity of Porous Particles. *Analytical Chemistry.* 2007;79(23):9115-9121.

77. Guy Y, Muha RJ, Sandberg M, Weber SG. Determination of Zeta-Potential and Tortuosity in Rat Organotypic Hippocampal Cultures from Electroosmotic Velocity Measurements under Feedback Control. *Analytical Chemistry.* 2009;81(8):3001-3007.

78. Guy Y, Sandberg M, Weber SG. Determination of ζ-potential in rat organotypic hippocampal cultures. *Biophysical Journal.* 2008;94(11):4561-4569.

79. Barrande M, Bouchet R, Denoyel R. Tortuosity of Porous Particles. *Analytical Chemistry (Washington, DC, United States).* 2007;79(23):9115-9121.

80. Glover PWJ, Gomez JB, Meredith PG. Fracturing in saturated rocks undergoing triaxial deformation using complex electrical conductivity measurements: experimental study. *Earth and Planetary Science Letters.* 2000;183(1-2):201-213.

81. Shiga T. Deformation and Viscoelastic Behavior of Polymer Gels in Electric Fields. *Neutron Spin Echo Spectroscopy Viscoelasticity Rheology.* Vol 134: Springer Berlin / Heidelberg; 1997:131-163.

82. Jabbari E, Tavakoli J, Sarvestani AS. Swelling characteristics of acrylic acid polyelectrolyte hydrogel in a dc electric field. *Smart Materials and Structures.* 2007;16(5):1614.

83. Gahwiler BH, Capogna M, Debanne D, McKinney RA, Thompson SM. Organotypic slice cultures: a technique has come of age. *Trends in Neurosciences.* 1997;20(10):471-477.

84. Stoppini L, Buchs PA, Muller D. A simple method for organotypic cultures of nervous tissue. *Journal of neuroscience methods.* 1991;37(2):173-182.

85. Jaquins-Gerstl A, Michael AC. Comparison of the brain penetration injury associated with microdialysis and voltammetry. *Journal of Neuroscience Methods.* 2009;183(2):127-135.

86. Mitala CM, Wang Y, Borland LM, et al. Impact of microdialysis probes on vasculature and dopamine in the rat striatum: a combined fluorescence and voltammetric study. *Journal of Neuroscience Methods.* 2008;174(2):177-185. Epub 2008 Jul 2015.

87. Budygin EA, Kilpatrick MR, Gainetdinov RR, Wightman RM. Correlation between behavior and extracellular dopamine levels in rat striatum: comparison of microdialysis and fast-scan cyclic voltammetry. *Neuroscience Letters.* 2000;281(1):9-12.

88. Kawagoe KT, Zimmerman JB, Wightman RM. Principles of voltammetry and microelectrode surface states. *Journal of Neuroscience Methods.* 1993;48(3):225-240.

89. Robinson DL, Venton BJ, Heien ML, Wightman RM. Detecting subsecond dopamine release with fast-scan cyclic voltammetry in vivo. *Clinical Chemistry.* 2003;49(10):1763-1773.

90. Asai S, Kohno T, Ishii Y, Ishikawa K. A newly developed procedure for monitoring of extracellular proteins using a push-pull microdialysis. *Analytical Biochemistry.* 1996;237(2):182-187.

91. Cellar NA, Burns ST, Meiners J-C, Chen H, Kennedy RT. Microfluidic Chip for Low-Flow Push-Pull Perfusion Sampling in Vivo with On-Line Analysis of Amino Acids. *Analytical Chemistry.* 2005;77(21):7067-7073.

92. Myers RD, Rezvani AH, Gurley-Orkin LA. New double-lumen polyethylene cannula for push-pull perfusion of brain tissue in vivo. *Journal of neuroscience methods.* 1985;12(3):205-218.

93. Xu H, Guy Y, Hamsher A, Shi G, Sandberg M, Weber SG. Electroosmotic Sampling. Application to Determination of Ectopeptidase Activity in Organotypic Hippocampal Slice Cultures. *Analytical Chemistry.* 2010;82(15):6377-6383.

94. Tsien RY. A non-disruptive technique for loading calcium buffers and indicators into cells. *Nature.* 1981;290(5806):527-528.

95. Cobbold PH, Rink TJ. Fluorescence and bioluminescence measurement of cytoplasmic free calcium. *Biochemistry Journal.* 1987;248(2):313-328.

96. Jobsis PD, Rothstein EC, Balaban RS. Limited utility of acetoxymethyl (AM)-based intracellular delivery systems, in vivo: interference by extracellular esterases. *Journal of Microscopy.* 2007;226(Pt 1):74-81.

97. Hamsher AE, Xu H, Guy Y, Sandberg M, Weber SG. Minimizing Tissue Damage in Electroosmotic Sampling. *Analytical Chemistry.* 2010;82(15):6370-6376.

98. Nicholson C, Chen KC, Hrabetova S, Tao L. Diffusion of molecules in brain extracellular space: theory and experiment. *Progress in Brain Research.* 2000;125(Volume Transmission Revisited):129-154.

99. Nicholson C, Sykova E. Extracellular space structure revealed by diffusion analysis. *Trends in Neurosciences.* 1998;21(5):207-215.

100. Sykova E, Mazel T, Vargova L, Vorisek I, Prokopova-Kubinova S. Extracellular space diffusion and pathological states. *Progress in Brain Research.* 2000;125:155-178.

101. Binder DK, Papadopoulos MC, Haggie PM, Verkman AS. In vivo measurement of brain extracellular space diffusion by cortical surface photobleaching. *Journal of Neuroscience.* 2004;24(37):8049-8056.

102. Ashwal S, Holshouser BA, Tong KA. Use of Advanced Neuroimaging Techniques in the Evaluation of Pediatric Traumatic Brain Injury. *Developmental Neuroscience (Basel, Switzerland).* 2006;28(4-5):309-326.

103. Kaiser LG, Meersmann T, Logan JW, Pines A. Visualization of gas flow and diffusion in porous media. *Proceedings of the National Academy of Sciences of the United States of America.* 2000;97(6):2414-2418.

104. Kroenke CD, Neil JJ. Use of magnetic resonance to measure molecular diffusion within the brain extracellular space. *Neurochemistry International.* 2004;45(4):561-568.

105. Pierpaoli C, Jezzard P, Basser PJ, Barnett A, Di Chiro G. Diffusion tensor MR imaging of the human brain. *Radiology.* 1996;201(3):637-648.

106. Thorne RG, Hrabetova S, Nicholson C. Diffusion of epidermal growth factor in rat brain extracellular space measured by integrative optical imaging. *Journal of Neurophysiology.* 2004;92(6):3471-3481.

107. Chen KC, Hoistad M, Kehr J, Fuxe K, Nicholson C. Theory relating in vitro and in vivo microdialysis with one or two probes. *J. Neurochem.* 2002;81(1):108-121.

108. Kehr J, Hoistad M, Fuxe K. Diffusion of radiolabeled dopamine, its metabolites and mannitol in the rat striatum studied by dual-probe microdialysis. *Progress in Brain Research.* 2000;125(Volume Transmission Revisited):179-190.

109. Thorne RG, Nicholson C. In vivo diffusion analysis with quantum dots and dextrans predicts the width of brain extracellular space. *Proceedings of the National Academy of Sciences of the United States of America.* 2006;103(14):5567-5572.

110. Perez-Pinzon MA, Tao L, Nicholson C. Extracellular potassium, volume fraction, and tortuosity in rat hippocampal CA1, CA3, and cortical slices during ischemia. *Journal of Neurophysiology.* 1995;74(2):565-573.

111. Sykova E. Extrasynaptic volume transmission and diffusion parameters of the extracellular space. *Neuroscience (Oxford).* 2004;129(4):861-876.

112. Mazel T, Simonova Z, Sykova E. Diffusion heterogeneity and anisotropy in rat hippocampus. *Neuroreport.* 1998;9(7):1299-1304.

113. Rice ME. Distinct regional differences in dopamine-mediated volume transmission. *Progress in Brain Research.* 2000;125(Volume Transmission Revisited):277-290.

114. Wightman RM, Amatore C, Engstrom RC, et al. Real-time characterization of dopamine overflow and uptake in the rat striatum. *Neuroscience (Oxford).* 1988;25(2):513-523.

115. Strigini M. Mechanisms of morphogen movement. *Journal of Neurobiology.* 2005;64(4):324-333.

116. Borland LM, Shi G, Yang H, Michael AC. Voltammetric study of extracellular dopamine near microdialysis probes acutely implanted in the striatum of the anesthetized rat. *Journal of Neuroscience Methods.* 2005;146(2):149-158.

117. Savtchenko LP, Kulahin N, Korogod SM, Rusakov DA. Electric fields of synaptic currents could influence diffusion of charged neurotransmitter molecules. *Synapse (New York).* 2004;51(4):270-278.

118. Ardolino G, Bossi B, Barbieri S, Priori A. Non-synaptic mechanisms underlie the after-effects of cathodal transcutaneous direct current stimulation of the human brain. *Journal of Physiology (London).* 2005;568(2):653-663.

119. Talelli P, Rothwell J. Does brain stimulation after stroke have a future? *Current opinion in neurology.* 2006;19(6):543-550.

120. Fregni F, Boggio Paulo S, Nitsche Michael A, Rigonatti Sergio P, Pascual-Leone A. Cognitive effects of repeated sessions of transcranial direct current stimulation in patients with depression. *Depression and Anxiety.* 2006;23(8):482-484.

121. Juckel G, Mendlin A, Jacobs BL. Electrical stimulation of rat medial prefrontal cortex enhances forebrain serotonin output: implications for electroconvulsive therapy and transcranial magnetic stimulation in depression. *Neuropsychopharmacology.* 1999;21(3):391-398.

122. Lisanby SH, Belmaker RH. Animal models of the mechanisms of action of repetitive transcranial magnetic stimulation (RTMS): comparisons with electroconvulsive shock (ECS). *Depression and anxiety.* 2000;12(3):178-187.

123. Kuroda Y, Motohashi N, Ito H, et al. Effects of repetitive transcranial magnetic stimulation on [11C]raclopride binding and cognitive function in patients with depression. *Journal of Affective Disorders.* 2006;95(1-3):35-42.

124. Kim EJ, Kim WR, Chi SE, et al. Repetitive transcranial magnetic stimulation protects hippocampal plasticity in an animal model of depression. *Neuroscience Letters.* 2006;405(1-2):79-83.

125. Wagner T, Gangitano M, Romero R, et al. Intracranial measurement of current densities induced by transcranial magnetic stimulation in the human brain. *Neuroscience Letters.* 2004;354(2):91-94.

126. Miranda P, C., Hallett M, Basser Peter J. The electric field induced in the brain by magnetic stimulation: a 3-D finite-element analysis of the effect of tissue heterogeneity and anisotropy. *IEEE transactions on biomedical engineering.* 2003;50(9):1074-1085.

127. Gluckman BJ, Nguyen H, Weinstein SL, Schiff SJ. Adaptive electric field control of epileptic seizures. *J. Neurosci.* 2001;21(2):590-600.

128. LeBeau FEN, Malmierca MS, Rees A. Iontophoresis in vivo demonstrates a key role for GABAA and glycinergic inhibition in shaping frequency response areas in the inferior colliculus of guinea pig. *Journal of Neuroscience.* 2001;21(18):7303-7312.

129. Calegari F, Marzesco A-M, Kittler R, Buchholz F, Huttner WB. Tissue-specific RNA interference in post-implantation mouse embryos using directional electroporation and whole embryo culture. *Differentiation (Malden, MA, United States).* 2004;72(2-3):92-102.

130. Cerda GA, Thomas JE, Allende ML, Karlstrom RO, Palma V. Electroporation of DNA, RNA, and morpholinos into zebrafish embryos. *Methods (San Diego, CA, United States).* 2006;39(3):207-211.

131. Abla N, Naik A, Guy RH, Kalia YN. Contributions of electromigration and electroosmosis to peptide iontophoresis across intact and impaired skin. *Journal of Controlled Release.* 2005;108(2-3):319-330.

132. Imanidis G, Luetolf P. An extended model based on the modified Nernst-Planck equation for describing transdermal iontophoresis of weak electrolytes. *Journal of Pharmaceutical Sciences.* 2006;95(7):1434-1447.

133. Nair V, Panchagnula R. Physicochemical considerations in the iontophoretic delivery of a small peptide: in vitro studies using arginine vasopressin as a model peptide. *Pharmacological Research.* 2003;48(2):175-182.

134. Nugroho AK, Li GL, Danhof M, Bouwstra JA. Transdermal Iontophoresis of Rotigotine Across Human Stratum Corneum in Vitro: Influence of pH and NaCl Concentration. *Pharmaceutical Research.* 2004;21(5):844-850.

135. Pikal MJ. The role of electroosmotic flow in transdermal iontophoresis. *Advanced Drug Delivery Reviews.* 2001;46(1-3):281-305.

136. Sieg A, Guy RH, Delgado-Charro MB. Electroosmosis in transdermal iontophoresis: Implications for noninvasive and calibration-free glucose monitoring. *Biophysical Journal.* 2004;87(5):3344-3350.

137. Vijh AK. Electrochemical treatment (ECT) of cancerous tumors: necrosis involving hydrogen cavitation, chlorine bleaching, pH changes, electroosmosis. *International Journal of Hydrogen Energy.* 2003;29(6):663-665.

138. Sekkat N, Naik A, Kalia YN, Glikfeld P, Guy RH. Reverse iontophoretic monitoring in premature neonates: feasibility and potential. *Journal of Controlled Release.* 2002;81(1-2):83-89.

139. Omasu F, Nakano Y, Ichiki T. Measurement of the electrophoretic mobility of sheep erythrocytes using microcapillary chips. *Electrophoresis.* 2005;26(6):1163-1167.

140. Miyake M, Kurihara K. Resting potential of the mouse neuroblastoma cells. II. Significant contribution of the surface potential to the resting potential of the cells under physiological conditions. *Biochim. Biophys. Acta.* 1983;762(2):256-264.

141. Dunlap CA, Biresaw G, Jackson MA. Hydrophobic and electrostatic cell surface properties of blastospores of the entomopathogenic fungus Paecilomyces fumosoroseus. *Colloids and Surfaces, B: Biointerfaces.* 2005;46(4):261-266.

142. Guzelsu N, Regimbal RL. The origin of electrokinetic potentials in bone tissue: the organic phase. *Journal of biomechanics.* 1990;23(7):661-672.

143. Badr GG, Waldman AA. Electrophoretic studies of intact nuclei isolated from mammalian brain. II. Electrokinetic characteristics following treatment and comparison of glial and neuronal nuclei. *International Journal of Neuroscience.* 1973;6(3):131-139.

144. Brewer GJ. Exocytosis and directed movement of cytoplasmic vesicles toward the plasma membrane. *Journal of Theoretical Biology.* 1980;85(1):75-82.

145. Stoilova S, Kancheva M. Microelectrophoretic properties of rat brain membrane structures - synaptosomes. *Stud. Biophys.* 1986;113(1-2):27-30.

146. Polevoi VV, Bilova TE, Shevtsov YI. Electroosmotic phenomena in plant tissues. *Biology Bulletin (Moscow, Russian Federation).* 2003;30(2):133-139.

147. Miyamoto M, Nakahari T, Yoshida H, Imai Y. Electroosmotic flow measurements. *Journal of Membrane Science.* 1989;41:377-391.

148. Nordenstrom BE. Fleischner lecture. Biokinetic impacts on structure and imaging of the lung: the concept of biologically closed electric circuits. *AJR. American journal of roentgenology.* 1985;145(3):447-467.

149. Rubashkin A, Iserovich P, Hernandez JA, Fischbarg J. Epithelial Fluid Transport: Protruding Macromolecules and Space Charges Can Bring about Electro-Osmotic Coupling at the Tight Junctions. *Journal of Membrane Biology.* 2006;208(3):251-263.

150. Boyack JR, Giddings JC. Theory of electrophoretic mobility in stabilized media. *Archives of Biochemistry and Biophysics.* 1963;100(1):16-25.

151. Rathore AS, Wen E, Horvath C. Electroosmotic Mobility and Conductivity in Columns for Capillary Electrochromatography. *Analytical Chemistry.* 1999;71(14):2633-2641.

152. Gahwiler BH, Capogna M, Debanne D, McKinney RA, Thompson SM. Organotypic slice cultures: a technique has come of age. *Trends in Neurosciences.* 1997;20(10):471-477.

153. Bahr BA. Long-term hippocampal slices: a model system for investigating synaptic mechanisms and pathologic processes. *Journal of Neurosci Research.* 1995;42(3):294-305.

154. Beeskow T, Kroner KH, Anspach FB. Nylon-based affinity membranes: impacts of surface modification on protein adsorption. *Journal of Colloid and Interface Science.* 1997;196(2):278-291.

155. Masson J-F, Battaglia TM, Davidson MJ, et al. Biocompatible polymers for antibody support on gold surfaces. *Talanta.* 2005;67(5):918-925.

156. Buchs PA, Stoppini L, Muller D. Structural modifications associated with synaptic development in area CA1 of rat hippocampal organotypic cultures. *Brain research.* 1993;71(1):81-91.

157. Gahwiler BH. Organotypic cultures of neural tissue. *Trends in Neuroscience.* 1988;11(11):484-489.

158. Holopainen IE. Organotypic Hippocampal Slice Cultures: A Model System to Study Basic Cellular and Molecular Mechanisms of Neuronal Cell Death, Neuroprotection, and Synaptic Plasticity. *Neurochemical Research.* 2005;30(12):1521-1528.

159. Olofsson J, Levin M, Stroemberg A, Weber SG, Ryttsen F, Orwar O. Scanning electroporation of selected areas of adherent cell cultures. *Analytical Chemistry (Washington, DC, United States).* 2007;79(12):4410-4418.

160. Todd P, Plank LD, Kunze ME, et al. Electrophoretic separation and analysis of living cells from solid tissues by several methods. Human embryonic kidney cell cultures as a model. *Journal of Chromatography.* 1986;364:11-24.

161. Vornov JJ, Tasker RC, Coyle JT. Direct observation of the agonist-specific regional vulnerability to glutamate, NMDA, and kainate neurotoxicity in organotypic hippocampal cultures. *Experimental. Neurology.* 1991;114(1):11-22.

162. Prokopova-Kubinova S, Vargova L, Tao L, et al. Poly[N-(2-hydroxypropyl) methacrylamide] polymers diffuse in brain extracellular space with same tortuosity as small molecules. *Biophysical Journal.* 2001;80(1):542-548.

163. Nicholson C, Tao L. Hindered diffusion of high molecular weight compounds in brain extracellular microenvironment measured with integrative optical imaging. *Biophysical Journal.* 1993;65(6):2277-2290.

164. McBain CJ, Traynelis SF, Dingledine R. Regional variation of extracellular space in the hippocampus. *Science.* 1990;249(4969):674-677.

165. Burdalo J, Medrano R, Saiz E, Tarazona MP. A simple method to determine unperturbed dimensions of polymers using size exclusion chromatography and multiangle light scattering. *Polymer.* 1999;41(4):1615-1620.

166. Sulzer D. The complex regulation of dopamine output: A review of current themes. *Clinical Neuroscience Research.* 2005;5(2-4):117-121.

167. Watts RJ, Harrigan RW, Crosby GA. Temperature and magnetic-field effects on the luminescence lifetimes of complexes of ruthenium(II) and iridium(III). *Chemical Physics Letters.* 1971;8(1):49-50.

168. Demas JN, Harris EW, McBride RP. Energy transfer from luminescent transition metal complexes to oxygen. *Journal of the American Chemical Society.* 1977;99(11):3547-3551.

169. Zhou F, Zhu X, Castellani RJ, et al. Hibernation, a model of neuroprotection. *The American journal of pathology.* 2001;158(6):2145-2151.

170. Stone TW. *Microiontophoresis and pressure ejection.* Vol 8. Chichester: Wiley; 1985.

171. Nicholson C, Tao L. Hindered diffusion of high molecular weight compounds in brain extracellular microenvironment measured with integrative optical imaging. *Biophysical Journal.* 1993;65(6):2277-2290.

172. Prokopova-Kubinova S, Vargova L, Tao L, et al. Poly[N-(2-hydroxypropyl) methacrylamide] polymers diffuse in brain extracellular space with same tortuosity as small molecules. *Biophysical Journal.* 2001;80(1):542-548.

173. Samec Z, Marecek V, Koryta J, Khalil MW. Investigation of ion transfer across the interface between two immiscible electrolyte solutions by cyclic voltammetry. *Journal of Electroanalytical Chemistry and Interfacial Electrochemistry.* 1977;83(2):393-397.

174. Nischang I, Tallarek U. Fluid dynamics in capillary and chip electrochromatography. *Electrophoresis.* 2007;28(4):611-626.

175. Maiti S, Shear JB, Williams RM, Zipfel WR, Webb WW. Measuring serotonin distribution in live cells with three-photon excitation. *Science.* 1997;275(5299):530-532.

176. Pellegatti L, Zhang J, Drahos B, et al. Pyridine-based lanthanide complexes: towards bimodal agents operating as near infrared luminescent and MRI reporters. *Chemical Communications.* 2008(48):6591-6593.

177. Kassam Amin B, Engh Johnathan A, Mintz Arlan H, Prevedello Daniel M. Completely endoscopic resection of intraparenchymal brain tumors. *Journal of neurosurgery.* 2009;110(1):116-123.

178. Hao J, Li SK, Liu C-Y, Kao WWY. Electrically assisted delivery of macromolecules into the corneal epithelium. *Experimental Eye Research.* 2009;89(6):934-941.

179. Hughes M. Ocular drug delivery: expanding the field of vision. *Drug Delivery Technology.* 2009;9(4):34-35.

180. Colombo R, Brausi M, Da Pozzo L, et al. Thermo-chemotherapy and electromotive drug administration of mitomycin C in superficial bladder cancer eradication. a pilot study on marker lesion. *European urology.* 2001;39(1):95-100.

181. Clarke G, Hill RG, Simmonds MA. Microiontophoretic release of drugs from micropipettes: use of 24Na as a model. *British Journal of Pharmacology.* 1973;48(1):156-161.

182. Hoffer BJ, Neff NH, Siggins GR. Microiontophoretic release of norepinephrine from micropipettes. *Neuropharmacology.* 1971;10(21):175-180.

183. Bloom FE. To spritz or not to spritz: the doubtful value of aimless iontophoresis. *Life sciences.* 1974;14(10):1819-1834.

184. Shoemaker WJ, Balentine LT, Siggins GR, Hoffer BJ, Henriksen SJ, Bloom FE. Characteristics of the release of adenosine 3':5'-monophosphate from micropipets by microiontophoresis. *Journal of cyclic nucleotide research.* 1975;1(2):97-106.

185. Purves R. Ionophoresis - progress and pitfalls. *Trends in Neurosciences.* 1980;3(10):245-247.

186. Chen KC, Nicholson C. Measurement of diffusion parameters using a sinusoidal iontophoretic source in rat cortex. *Journal of Neuroscience Methods.* 2002;122(1):97-108.

187. Hrabetova S, Masri D, Tao L, Xiao F, Nicholson C. Calcium diffusion enhanced after cleavage of negatively charged components of brain extracellular matrix by chondroitinase ABC. *Journal of Physiology*. 2009;587(16):4029-4049.

188. Dionne VE. Characterization of drug iontophoresis with a fast microassay technique. *Biophysical Journal.* 1976;16(7):705-717.

189. Armstrong-James M, Fox K, Kruk ZL, Millar J. Quantitative ionophoresis of catecholamines using multibarrel carbon fibre microelectrodes. *Journal of Neuroscience Methods.* 1981;4(4):385-406.

190. Armstrong-James M, Millar J, Kruk ZL. Quantification of noradrenaline iontophoresis. *Nature.* 1980;288(5787):181-183.

191. Herr NR, Daniel KB, Belle AM, Carelli RM, Wightman RM. Probing presynaptic regulation of extracellular dopamine with iontophoresis. *ACS Chemical Neuroscience.* 2010;1(9):627-638.

192. Purves RD. The physics of iontophoretic pipettes. *Journal of neuroscience methods.* 1979;1(2):165-178.

193. Curtis DR, Perrin DD, Watkins JC. Excitation of spinal neurons by the ionophoretic application of agents which chelate calcium. *Journal of Neurochemistry.* 1960;6:1-20.

194. Trubatch J, Van Harreveld A. Spread of iontophoretically injected ions in a tissue. *Journal of Theoretical Biology.* 1972;36(2):355-366.

195. Lux HD, Neher E. The equilibration time course of (K +) 0 in cat cortex. *Experimental brain research.* 1973;17(2):190-205.

196. Nicholson C, Phillips JM, Gardner-Medwin AR. Diffusion from an iontophoretic point source in the brain: role of tortuosity and volume fraction. *Brain research.* 1979;169(3):580-584.

197. Norman RS. Diffusional spread of iontophoretically injected ions. *Journal of theoretical biology.* 1975;52(1):159-162.

198. Herr NR, Kile BM, Carelli RM, Wightman RM. Electroosmotic flow and its contribution to iontophoretic delivery. *Analytical Chemistry.* 2008;80(22):8635-8641.

199. Scott ER, Laplaza AI, White HS, Phipps JB. Transport of ionic species in skin: contribution of pores to the overall skin conductance. *Pharmaceutical research.* 1993;10(12):1699-1709.

200. Drouin H. On microelectrode ionophoresis. *Biophysical Journal.* 1984;46(5):597-604.

201. Noraberg J, Kristensen BW, Zimmer J. Markers for neuronal degeneration in organotypic slice cultures. *Brain research protocols.* 1999;3(3):278-290.

202. Beisler AT, Schaefer KE, Weber SG. Simple method for the quantitative examination of extra column band broadening in microchromatographic systems. *Journal of Chromatography A.* 2003;986(2):247-251.

203. Barz DPJ, Vogel MJ, Steen PH. Determination of the Zeta Potential of Porous Substrates by Droplet Deflection. I. The Influence of Ionic Strength and pH Value of an Aqueous Electrolyte in Contact with a Borosilicate Surface. *Langmuir.* 2009;25(3):1842-1850.

204. McGuffin VL, Tavares MFM. Computer-Assisted Optimization of Separations in Capillary Zone Electrophoresis. *Analytical Chemistry.* 1997;69(2):152-164.

205. Thormann W, Zhang C-X, Caslavska J, Gebauer P, Mosher RA. Modeling of the impact of ionic strength on the electroosmotic flow in capillary electrophoresis with uniform and discontinuous buffer systems. *Analytical Chemistry.* 1998;70(3):549-562.

206. Scales N, Tait RN. Modeling electroosmotic and pressure-driven flows in porous microfluidic devices: Zeta potential and porosity changes near the channel walls. *Journal of Chemical Physics.* 2006;125(9):094714/094711-094714/094712.

207. Zoski CG, Bond AM, Allinson ET, Oldham KB. How long does it take a microelectrode to reach a voltammetric steady state? *Analytical Chemistry.* 1990;62(1):37-45.

208. Krnjević K. When and why amino acids? *The Journal of Physiology.* 2010;588(1):33-44.

209. Kirby BJ, Hasselbrink EF. Zeta potential of microfluidic substrates: 1. Theory, experimental techniques, and effects on separations. *Electrophoresis.* 2004;25(2):187-202.

210. Scales N, Tait RN. Modeling wall effects in capillary electrochromatography. *Journal of Chromatography, A.* 2008;1205(1-2):150-157.

211. Rathore AS, Horvath C. Axial Nonuniformities and Flow in Columns for Capillary Electrochromatography. *Analytical Chemistry.* 1998;70(14):3069-3077.

212. Westerhuis WH, Sturgis JN, Niederman RA. Reevaluation of the electrophoretic migration behavior of soluble globular proteins in the native and detergent-denatured states in polyacrylamide gels. *Analytical Biochemistry.* 2000;284(1):143-152.

213. Stylianopoulos T, Diop-Frimpong B, Munn LL, Jain RK. Diffusion Anisotropy in Collagen Gels and Tumors: The Effect of Fiber Network Orientation. *Biophysical Journal.* 2010;99(10):3119-3128.

214. Baraban SC, Bausch SB. Organotypic Hippocampal Slice Cultures as a Model of Limbic Epileptogenesis. *Animal Models of Epilepsy.* Vol 40: Humana Press; 2009:183-201.

215. Hamsher A, Xu H, Guy Y, Sandberg M, Weber SG. Minimizing tissue damage in electroosmotic sampling. *Analytical Chemistry.* 2010;82(15):6370-6376.

216. Duport S, Robert F, Muller D, Grau G, Parisi L, Stoppini L. An in vitro blood-brain barrier model: cocultures between endothelial cells and organotypic brain slice cultures. *Proceedings of the National Academy of Sciences of the United States of America.* 1998;95(4):1840-1845.

217. Oldenziel WH, Dijkstra G, Cremers TIFH, Westerink BHC. Evaluation of Hydrogel-Coated Glutamate Microsensors. *Analytical Chemistry.* 2006;78(10):3366-3378.

218. Kim J, Tsien RW. Synapse-specific adaptations to inactivity in hippocampal circuits achieve homeostatic gain control while dampening network reverberation. *Neuron.* 2008;58(6):925-937.

219. Lipinski HG. Brain tissue slice thickness monitored by ion-profile measurement. *Journal of neuroscience methods.* 1992;42(1-2):37-43.

220. Oldenziel WH, van der Zeyden M, Dijkstra G, et al. Monitoring extracellular glutamate in hippocampal slices with a microsensor. *Journal of Neuroscience Methods.* 2007;160(1):37-44.

221. Robert F, Parisi L, Bert L, Renaud B, Stoppini L. Microdialysis monitoring of extracellular glutamate combined with the simultaneous recording of evoked field potentials in hippocampal organotypic slice cultures. *Journal of Neuroscience Methods.* 1997;74(1):65-76.

222. Schrenk-Siemens K, Perez-Alcala S, Richter J, et al. Embryonic stem cell-derived neurons as a cellular system to study gene function: Lack of amyloid precursor proteins APP and APLP2 leads to defective synaptic transmission. *Stem Cells.* 2008;26(8):2153-2163.

223. Takahashi M, Liou SY, Kunihara M. Ca(2+)- and Cl(-)-dependent, NMDA receptor-mediated neuronal death induced by depolarization in rat hippocampal organotypic cultures. *Brain Research.* 1995;675(1-2):249-256.

224. Cho S, Wood A, Bowlby MR. Brain slices as models for neurodegenerative disease and screening platforms to identify novel therapeutics. *Current Neuropharmacology.* 2007;5(1):19-33.

225. Noraberg J. Organotypic brain slice cultures: An efficient and reliable method for neurotoxicological screening and mechanistic studies. *ATLA, Alternatives to Laboratory Animals.* 2004;32(4):329-337.

226. Muller D, Toni N, Buchs P-A, Parisi L, Stoppini L. Interface Organotypic Hippocampal Slice Cultures. *Protocols for Neural Cell Culture*: Springer Protocols; 2001:13-27.